ULTRAFAST NONLINEAR OPTICAL PROPERTIES OF PASSIVE AND ACTIVE SEMICONDUCTOR DEVICES

BY

ALI REZA MOTAMEDI

B.A.SC. ELECTRICAL ENGINEERING, 1990
SIMON FRASER UNIVERSITY
BURNABY, BC, CANADA

M.A.SC. ELECTRICAL ENGINEERING AND COMPUTER SCIENCE, 1997
UNIVERSITY OF VICTORIA,
VICTORIA, BC, CANADA

SUBMITTED TO THE DEPARTMENT OF ELECTRICAL ENGINEERING AND COMPUTER SCIENCE IN PARTIAL FULFILLMENT OF THE REQUIREMENTS FOR THE DEGREE OF

DOCTORATE OF PHILOSOPHY
AT THE
MASSACHUSETTS INSTITUTE OF TECHNOLOGY

JUNE 2011

SIGNATURE OF AUTHOR:_____
Department of Electrical Engineering and Computer Science
February 8, 2011

CERTIFIED BY:_____
Erich P. Ippen
Elihu Thomson Professor of Electrical Engineering and Computer Science
Professor of Physics
Thesis Supervisor

ACCEPTED BY:_____
Terry P. Orlando
Professor of Electrical Engineering and Computer Science
Chairman, Department Committee on Graduate Students

ULTRAFAST NONLINEAR OPTICAL PROPERTIES OF PASSIVE AND ACTIVE SEMICONDUCTOR DEVICES

BY

ALI REZA MOTAMEDI

SUBMITTED TO THE DEPARTMENT OF ELECTRICAL ENGINEERING AND COMPUTER SCIENCE ON FEBRUARY 8, 2011 IN PARTIAL FULFILLMENT OF THE REQUIREMENTS FOR THE DEGREE OF DOCTOR OF PHILOSOPHY IN ELECTRICAL ENGINEERING AND COMPUTER SCIENCE

Abstract

Nonlinear optical properties and ultrafast carrier dynamics of slab-coupled optical waveguide amplifiers, silicon nanowaveguides, and III-V semiconductor saturable Bragg reflectors are studied. The limits imposed by two photon absorption and free-carrier absorption on the gain and output powers of an InGaAsP/InP slab-coupled optical waveguide amplifier with a confinement factor of $\Gamma = 0.5\%$ are determined. The two-photon absorption coefficient and the induced free-carrier absorption cross-section were measured to be 65cm/GW and $7\text{x}10^{-17}$ cm^2, respectively. The effects of two-photon absorption begin to limit the gain significantly for pulses shorter than 40ps. The carrier recovery times were observed to vary between 390 to 160ps for 1A to 4A bias currents, and the short-pulse saturation fluence of the gain was determined to be 1.4mJ/cm^2. Furthermore, nonlinear optical processes in high-index-contrast waveguide circuits consisting of 106nm x 497nm silicon waveguides with SiO_2 and HSQ cladding layers were studied using a heterodyne pump probe experimental setup. The linear loss of the waveguides was determined to be 6.5dB/cm. The two-photon absorption coefficient and free-carrier absorption effective cross-section were determined to be 0.68cm/GW, and $1.9\text{x}10^{-17}$ cm^2, respectively. Coefficients for the index changes due to optical Kerr effect, and free-carrier density were determined to be $3.2\text{x}10^{-14}$ cm^2/W, and $-5.5\text{x}10^{-21}$ cm^3. Effects of the proton bombardment on linear loss and carrier lifetimes in the devices were also studied. Carrier lifetime reduction to 33ps with a linear loss of only 14.8dB/cm was achieved using a proton bombardment level of $10^{15}/\text{cm}^2$. Ultrafast dynamics of semiconductor saturable absorber mirrors were also investigated. The addition of resonant layers to the absorbers resulted in lower saturation fluence and increased non-saturable loss. Proton bombardment was utilized on these devices as well, to decrease the carrier recovery times. With proton bombardment of single-absorber layer devices with 40KeV proton energies at a dose of $10^{15}/\text{cm}^2$, a 1.5ps carrier recovery time was achieved in single-absorber structures.

Thesis Supervisor: Erich P. Ippen
Title: Elihu Thompson Professor of Electrical Engineering and Computer Science
Professor of Physics

I DEDICATE THIS THESIS WITH

LOVE

TO MY MOTHER

MINOO MOTAMEDI

THANK YOU MOM FOR YOUR INFINITE

LOVE, PERSEVERANCE, AND SACRIFICES

Acknowledgements

As I think about the people that I would like to thank, I can't help but to reflect on the past several years at MIT, from the first day that I arrived having driven from the bay area to Boston until the moment that I presented my conclusions at my defense. A dream that has finally become a reality and a reality that without the following people's help wouldn't have been possible.

First and foremost, I would like to thank my advisor and my mentor, Professor Erich Ippen. I still remember the excitement that I felt on the day that he agreed to take me on as one of his graduate students. I couldn't wait to begin my research. Throughout the years his support, infinite kindness, and patience made my experience at MIT most enjoyable and memorable. Professor Ippen was always available for technical and career related discussions which made it extremely easy to discuss the future directions of any experiment or project. His intuitions, high standards, strive for excellence, and enthusiasm created an environment conducive to learning and excellence. He once told me, "the most important part of doing research is to know what questions to ask."

I would like to thank Professor Rajeev Ram and Professor Franz Kärtner for agreeing to be on my PhD committee. With Professor Ram, I enjoyed many technical and technology related discussions, including but not limited to topics ranging from semiconductor physics, biology

related topics, to startups, and business related issues. I will always remember him telling me, "any research topic that you decide to pursue, make sure that you end up being the best in the world at it so that everyone else will come to you when they have a problem in that field." Professor Kärtner was always available to look at my results and always ask that one question that I had never thought of, no matter how prepared I was stepping into his office. He was always available for the next technical discussion. I admired his enthusiasm for the variety of different topics of research that he undertook in his group. I would also like to thank Professor Kolodziejski and Dr. Gale Petrich for collaboration on the SBR project.

I would like to thank several colleagues at Lincoln Lab, first and foremost, I thank Paul Juodawlkis from Lincoln Lab for making the SCOWA project possible by generously donating several devices for characterization. I admired his vision for the future of the IPI program and the SCOW devices. Jason Plant and I collaborated on the SCOW devices and he generously donated much of his time discussing the intricacies of mounting and aligning the devices. Scott Hamilton, Bryan Robinson, and Jade Wang for collaboration on the SOA based optical switching project. I also had the great privilege of working with Kazi Abedin on quantum-dot SOAs. We worked hard and rewarded ourselves with drinking strong coffee while listening to Jazz.

Of the past and current friends and colleagues at MIT, I would like to start by thanking Juliet Gopinath for getting me started on the pump-probe setup. Her support and help continued well after she left MIT and while she was working at Lincoln Lab. She was always available for sharing her extensive knowledge and past experience on fixing the OPAL laser when it stopped working. Aside from work, it was delightful to talk to her about MIT and life in general. My collaboration with Anatol Khilo on the silicon project was most fruitful. His calculations of the effective area made the chapter on silicon nanowaveguides possible. Our work extended well

beyond "normal" working hours with help of very strong coffee late in the evenings to get us through the analysis. I would like to thank Amir Nejadmalayeri for his assistance in setting up the heterodyne pump-probe experiment. There was never a dull moment in the lab, and we managed to combine many hours of hard work with many jokes and fun moments. It was a great pleasure to work with Amir. SBR project was made possible by collaboration with Michelle Sander, Hyunil Byun, and Hanfei Shen. Michelle's work on the proton bombardment and multi-quantum-well SBRs resulted in very interesting results. I wish her much success in her future endeavors with proton bombardment of the SBRs and the new designs. Hyunil demonstrated the operation of some of the SBRs in his setup and we worked on Si/Ge project together as well. We were working together when he first met Soonmin who later became his life partner. Hanfei and I collaborated on SBR project, shared many hockey stories, and cheered for the opposite teams more often than we probably like to admit!!! All of this work wouldn't have been possible without the incessant support of Donna Gale and Dorothy Fleischer. I will never forget Donna's extreme kindness and support throughout my PhD career. I always looked forward to our early morning conversations which took place after I made my cup of coffee and before anyone else arrived in the office. Special thanks go to Dave Foss, Bill Adams and Sukru Cinar in the RLE headquarters for their support throughout my years at MIT.

Jason Sickler and I shared a very interesting and amusing sense of humor and we always knew what the other one was about to say or was thinking at the time. Jonathan Morse never ceased to amaze me with how many different gadgets one can carry around. His level of organization is against the laws of entropy. I am extremely grateful for him being so organized so that instead of my own lab, I could always count on finding what I need in his!!! Marcus Dahlem and I started the same year at MIT and shared several fun-filled road trips together and

spent much time supporting each other while we served on the GradRat committee at MIT. He was always willing and available to help with any experimental setup and it was a pleasure to work with him. Milos Popovic and I shared many lunches discussing quantum mechanics, and imaginary and made up particles including gravitinos (combination of gravitons and neutrinos). Peter Rakich's intuition for different measurement techniques was certainly to be admired. Politics and world economic were topics of many discussions with Jonathan Birge. Andrew Benedick's willingness to generously share his test equipment saved many hours of search around different labs. Vikas Sharma and I started grad school at the same time and later became roommates and now very close friends. His ability to pick out a half dozen misaligned pixels on a 36 inch TV which required several trips back and forth to the store is unmatched by anyone I have ever known!!! Hung-Wen Shen and Katia Shtyrkova are my latest officemates and despite the very short period of time knowing them, I am certain that our friendships will last well beyond my time at MIT.

Vincent Berube and I became friends through hockey. I'll never forget the amazing times we spent together in Vancouver during the winter Olympics of 2010, and I am certain that we both remember the moment that Canada won the gold medal in hockey. Jess Vey and I made great friends enjoyed many political discussions with her, especially around the election times. I would also like to thank my very good friend Baharak Moshiree for her support through very difficult and emotional times in my life. Her presence at my thesis defense was a pleasant surprise and I am most appreciative.

While at MIT, I had the privilege of developing long lasting friendships with very special people. The first person that I met when I arrived at MIT was Obrad Scepanovic. We started as labmates and our friendship has developed to the point that I feel as though we are parts of the

same family. I have had the great privilege of making friends with Dave Berns whom I met through playing ice hockey at MIT. I thank Dave for his support and infinite kindness throughout the years of knowing him. Dave is just like another brother to me and I know that our friendship will last a lifetime.

I would like to thank Dean Blanche Staton and Professor Terry Orlando for their support and help in what turned out to be very challenging period of my life. I feel extremely blessed to have had the opportunity to meet such wonderful people.

In my life, there are three very special people who made everything I am today possible. First and foremost, I would like to thank my brother Mo Motamedi. He has been a brother, a father, a critique, a friend, and the pillar of support to me. He guided me through my life and without his many sacrifices, generosity, and love, I could have never completed this thesis. Second, I would like to thank my sister-in-law Jeannette van der Velde for her kindness, love, and support throughout the years. I certainly enjoyed our conversations about family, life, relationships, and career at a coffee shop on Newbury street. I thank her for being there for me when I needed a somewhat "unbiased" opinion!!!

Finally, the most important person in my life, and the one who made everything I am today possible with her vision, determination, and no-defeat attitude. I would like to thank the most important person in my life, my confidant, my teacher, role model, inspiration, and my best friend, and that would be my mother, Minoo Motamedi. She has been a father, a mother, a sister, and most importantly the best friend to me. I am blessed that I was born to Minoo Motamedi. Her infinite unconditional love, lifetime of sacrifices, hard work, purpose, care, determination, and resilience, gave me the opportunity to pursue my dreams, and her continued encouragements made me overcome many obstacles in my life. I thank you mom, and I am proud to be your son.

Table of Contents

List of Figures

List of Tables

Chapter 1

Introduction

1.1. Motivation

The explosive growth in the internet traffic experienced in the late 90s has only become more explosive in the past 5 years with the increasing demand for personal mobile devices, digital TV and radio, gaming industry, and online videos. In 2009, the data consumption by Americans was estimated at 3.6 zettabytes equivalent to 36 million million gigabytes, and enough to fill 7 DVDs per day. The breakdowns of this data consumption are 55% games, 35% digital TV and 10% movies and computer data only took up less than 1% of the total data [1, 2]. The demand is not stopping at these numbers but growing at 5.4% per year, and for most part many users still feel that their connection to the internet is not fast enough. To move such a large volume of data, new ways to pack more data into the fiber is being explored. For this purpose, new methods for faster data transfer using dense wavelength division multiplexing (DWDM) [3-8] and optical time-division multiplexing (OTDM) [9-12] have been studied. In a DWDM system, several wavelengths closely separated by wavelength are each modulated with data and transmitted over

the optical fiber networks to the destination. While in transit from the source to the destination and at the receiver, each wavelength is separated and the data is extracted. In OTDM networks, in addition to having the option of using different wavelengths, the data is multiplexed in the time domain by the sender and demultiplexed at the receiver and the routers. In the conventional DWDM and OTDM systems, each wavelength is generated by a different optical source. However, with the broad spectral bandwidth of mode-locked lasers, the output of these devices can be sliced in the frequency domain to generate different wavelengths. The high repetition rate of mode-locked lasers can also be utilized in the OTDM systems for generation high frequency pulse trains. One of the topics covered in this thesis is the study of the ultrafast carrier dynamics and nonlinear optical properties of saturable absorbers which are amongst the main constituent elements of mode-locked lasers.

Free-space optical communication (FSO) systems also offer large data rates and have received a great deal of attention in the past years [13-16]. Optical signals transmitted over long distances must be amplified at several intervals to overcome the scattering and atmospheric losses. Eye-safe, high power optical lasers and amplifiers operating around 1.5μm can extend the transmission range and reduce the number of repeater stations. High power SOAs have also found application in laser imaging and detection systems[17, 18]. Conventional SOAs offer several advantages including high gain, large bandwidth, low-noise operation, and compact size. However, obtaining high saturation powers from these devices remains a challenge. A class of SOAs that overcomes this is the slab-coupled optical waveguide amplifiers (SCOWAs) [19-21]. SCOWA design is based on Marcatili's coupled-mode analysis which demonstrated that a large multimode waveguide structure can be designed to operate in the single fundamental mode by coupling the higher order modes to the adjacent slab waveguide[22]. SCOWAs offer large

saturation powers and large mode-size, the latter being compatible with that of a single-mode fiber for efficient coupling. The SCOW topology has also been applied to lasers (SCOWL) in both CW[23, 24] and mode-locked configurations[25-27]. However, because of the high intensity of the optical signals inside the slab, optical nonlinearities limit the maximum achievable saturation energy[28, 29]. In this thesis, the limitations imposed by optical nonlinearities on the saturation energy of a SCOWA for transmission of pulses and their carrier dynamics as a function of the bias current are studied.

The large bandwidth and high data rates offered by these photonic technologies is also being extended to solving the current bottle-neck that exists in communication between different chips on the same CPU board. Therefore, development of different silicon-based optical devices using silicon technology has received a great deal of attention [30-37]. Silicon-photonics is an attractive technology because of its compatibility with the mature CMOS technology which enables low-cost large-volume production of devices. Because of advancements in silicon technology, driven mainly by the semiconductor industry, silicon-waveguides with transverse dimensions less than 20nm can be efficiently fabricated[38]. With such small feature sizes, many compact silicon-based devices can be integrated on the same chip to produce a complete on-chip transceiver[39-41]. However, with the increasing data rates, the pulsewidths of optical signals become shorter resulting in higher optical signal peak power. The small transverse dimension of waveguides carrying data results in peak intensities in the order of several MW/cm^2. At such high intensities, the nonlinear optical properties of silicon limit the maximum power that can be transmitted through these waveguides. This, combined with the carrier lifetime in silicon devices which, depending on the quality of the material, can vary from a few hundreds of picoseconds to several nanoseconds, limit the maximum achievable data rates. Nonlinear silicon photonics have

been extensively studied and has received much attention in recent years[32, 33, 42-57]. In this thesis, we present the results of self-consistent femtosecond studies of these properties at 1.5μm in silicon nanowaveguides using a heterodyne pump-probe technique. This measurement technique is sensitive to both instantaneous and longer-lived optically induced loss and index of refraction changes. Therefore, both loss and refractive index changes are measured simultaneously using the same technique. In the following sections, some of the applications of mode-locked lasers and silicon-photonics are described.

1.2. Mode-locked lasers

Mode-locked lasers offer several advantages including high peak intensities, highly stable repetition rate, and broad spectral range that have found many applications. The high peak intensities produced by femtosecond and picosecond mode-locked lasers can be utilized to apply a very high intensity burst of energy in a very short period of time, breaking bonds between molecules or resulting in ablation of tissue. Therefore, mode-locked lasers have found applications in nanosurgery[58, 59] and precision micro-machining[60, 61]. Their broad output spectrum combined with their highly stable repetition rate has been utilized in many applications such as frequency metrology[62-64], astrophysics[65], optical coherence tomography[66-68], and optical arbitrary waveform generation (OAWG) [69-72]. Recently, a multi-disciplinary collaborative project between MIT, UC Davis, and several companies was funded by DARPA to develop such an OAWG system. An arbitrary optical waveform can be manipulated in the time domain by controlling its Fourier components in frequency domain. The broad optical spectrum generated by a high repetition-rate mode-locked laser is ideally suited to being divided spatially in a way that permits each frequency component to be modulated rapidly for ultra-broadband

arbitrary optical waveform generation in the time domain. Figure 1-1 shows a conceptual picture of this process. Mode-locked lasers play an important part in making OAWG systems possible.

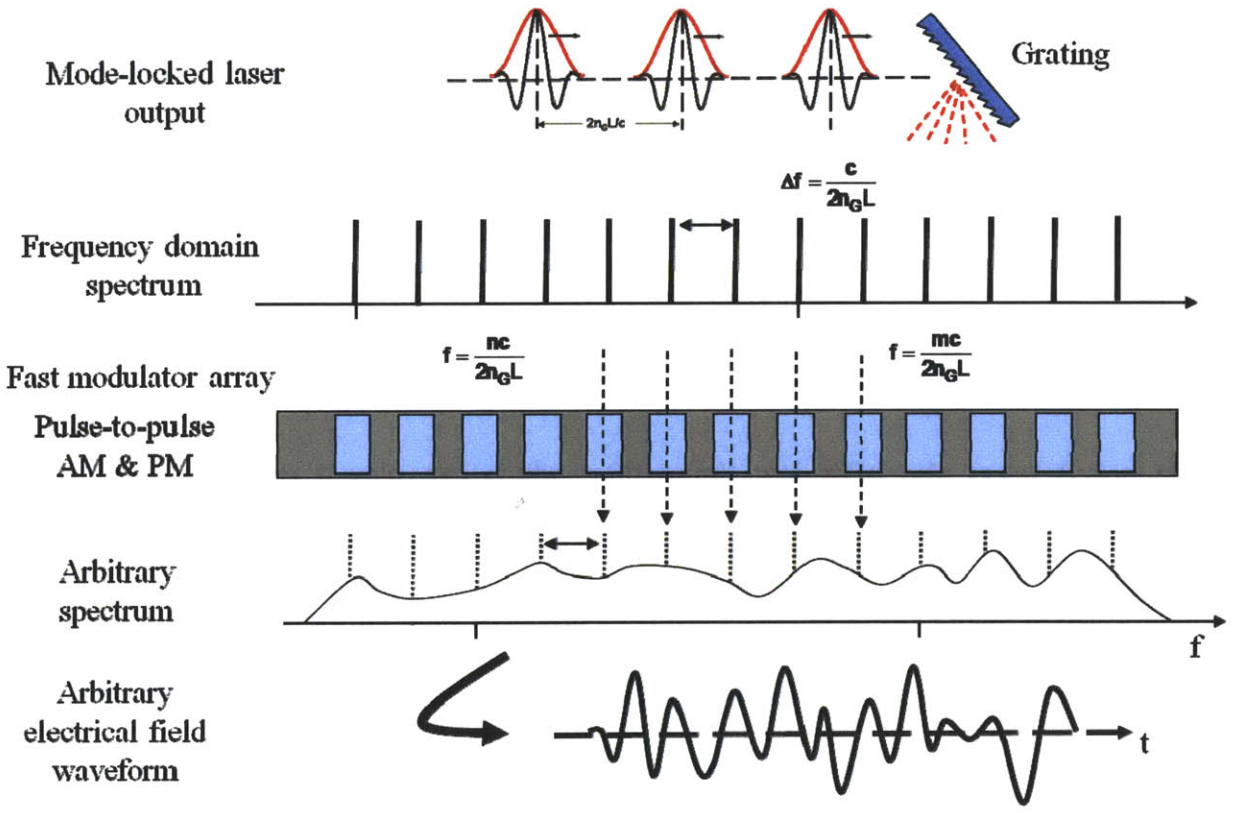

Figure 1-1 – Optical arbitrary waveform generation using a mode-locked laser. The output spectrum of the laser is sliced into different wavelengths and each is amplitude and phase modulated in frequency domain to generate an arbitrary E-field in time domain [69].

Stable operation of mode-locked lasers with femtosecond or picosecond pulsewidths has become possible by addition of a semiconductor saturable absorber in the laser cavity. A saturable absorber (SA) consists of a normally absorptive layer, the loss of which decreases with increasing intensity of the incident light. As the formation of a pulse in a laser cavity results in high peak intensities, this intensity-dependent transparency of SAs results in preferential operation of the laser in a short-pulse mode. With the advancement in fabrication processes and advent of bandgap engineering, broadband SAs with different absorption spectra nonlinearity and bandwidth have become possible[73-79]. In addition to the saturation dynamics of an SA,

the recovery times of a device can determine for a given output power, both the duration of the pulses generated and the maximum repetition rate that can be achieved in the laser. Studies of both saturation and ultrafast carrier dynamics of saturable absorbers are extremely important for predicting the stability and limitations of a mode-locked laser. Saturation dynamics and effects of proton bombardment on the carrier lifetime of different semiconductor saturable absorber mirror (SESAM) structures are studied in this thesis.

1.3. Analog-to-digital conversion

Mode-locked lasers also offer low timing-jitter which can play a role in improving high frequency electronic analog-to-digital conversion[80-82]. An example of such a system is demonstrated in Figure 1-2. A mode-locked laser produces short pulses that are passed through a length of fiber. The chirped output of the fiber is passed through an electro-optic modulator (EOM), the input to which is the RF signal to be sampled. The output of the EOM is passed through N-number of ring-resonator filter banks that spectrally separate the chirped pulses into N wavelength-separated sub-pulses. These pulses are then converted to electrical domain using N-photodetectors and sampled using commercially available ADCs. This provides an effective sampling rate of N-times the sampling rate of that of the pulse repetition rate and electronic quantization rate. One of the advantages offered by this system is that all the devices with the exception of the mode-locked lasers can be fabricated in silicon, hence allowing for integration of most of the components on a single chip. This project has been a collaborative effort between MIT and Lincoln Lab funded by DARPA. In this thesis, the nonlinear optical properties of these silicon nanowaveguides and the effects of proton bombardment on their recovery times are

studied. The results of these studies can lead to the design optimization at both component and system levels.

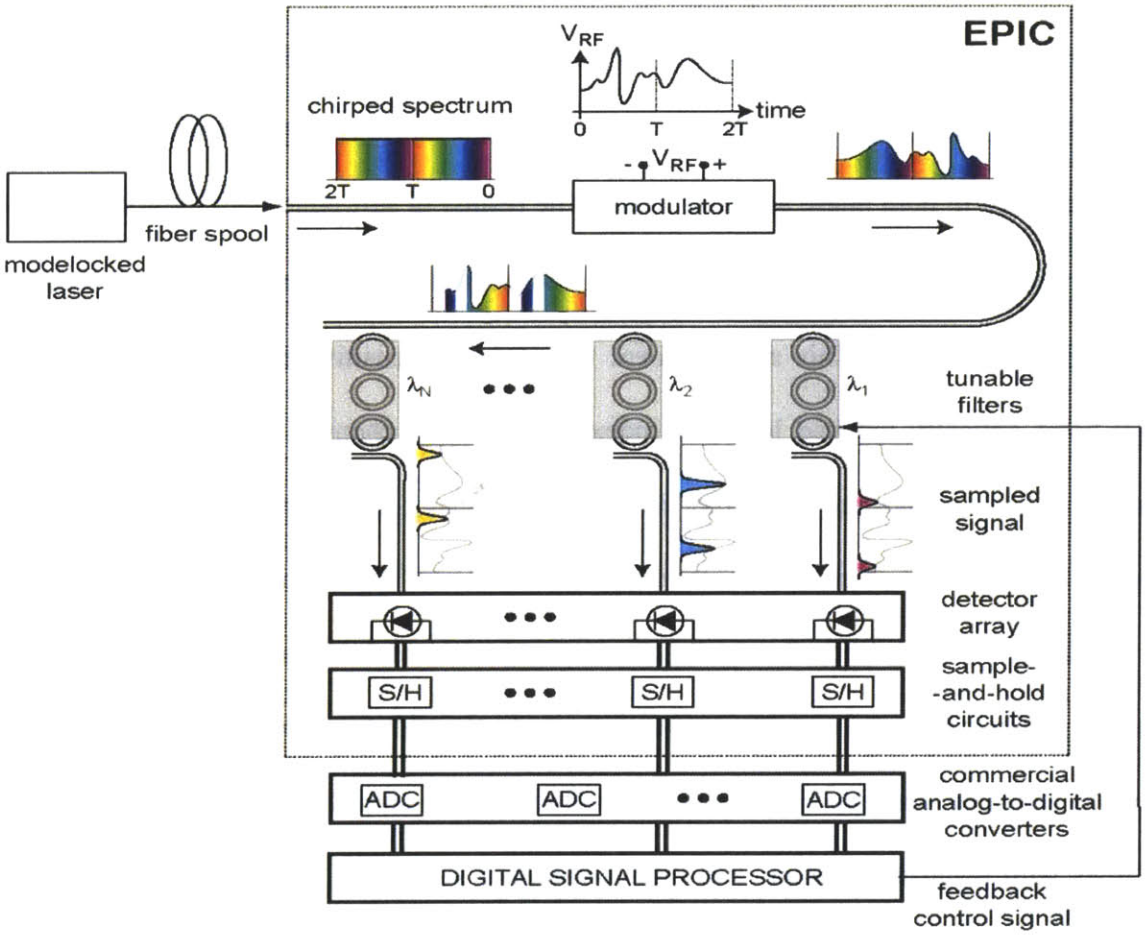

Figure 1-2 – An example of a photonic analog-to-digital converter. The optical path consists of a mode-locked laser, 2km spool of fiber, an optical modulator, and several ring-resonator filter banks and photodetectors. The electronics consist of several sample-and-hold and commercially available ADC circuits, and a DSP chip.

1.4. Thesis outline

In chapter 2 of this thesis, I will give a brief overview of the nonlinear optical processes that play a role in the experimental investigations described in the following sections. In Chapter 3, limitations imposed by nonlinear optical processes on the saturation energy of a SCOWA are

presented. A degenerate double-chopped pump-probe experiment using pulsewidths varying between 1.4 to 40ps is utilized to extract the two-photon absorption coefficient. The gain dynamic of the SCOWA as a function of the input power and pulsewidth is studied and the free-carrier absorption effective cross-section and saturation energy of the device are extracted.

Chapter 4 contains a detailed study of ultrafast nonlinear optical processes in silicon nanowaveguides in both phase and magnitude. The results of self-consistent femtosecond studies of these properties at 1.5μm in silicon nanowaveguides using a heterodyne pump-probe technique are presented. This measurement technique is sensitive to both instantaneous and longer-lived optically induced loss and index of refraction changes. Therefore, both loss and refractive index changes are measured simultaneously using the same technique. The results of the study of the effects of proton bombardment on the carrier lifetime are also presented.

Chapter 5 deals with the study of semiconductor saturable absorber mirrors. A cross-polarized pump-probe experiment was setup to study the ultrafast carrier dynamics of different saturable absorber designs. These designs include single-absorber structures, single-absorber SESAMs with resonant coatings, and double-absorber structures. The saturation dynamics and the carrier lifetime in these devices as a function of proton-bombardment were determined.

1.5. References

[1] R. R. Bohn and J. E. Short, "How Much Information? 2009 Report on American Consumers," December 2009.

[2] P. Boutin. (2009). *Americans consume 3,600,000,000,000,000,000,000 bytes of information per year, not counting work.* Available: http://venturebeat.com/2009/12/10/americans-consume-360000000000000000000-bytes-of-information-per-year-not-counting-work/

[3] D. J. Richardson, "Filling the Light Pipe," *Science,* vol. 330, pp. 327-328, October 15, 2010 2010.

[4] S. Chandrasekhar, *et al.*, "Terabit transmission at 42.7-gb/s on 50-GHz grid. using hybrid RZ-DQPSK and NRZ-DBPSK formats over 16 x 80 km SSMF spans and 4 bandwidth-managed ROADMs," *Journal of Lightwave Technology,* vol. 26, pp. 85-90, Jan-Feb 2008.

[5] K. Schuh, *et al.*, "8 Tb/s (80 x 107 Gb/s) DWDM NRZ-VSB Transmission Over 510 km NZDSF with 1 bit/s/Hz Spectral Efficiency," *Bell Labs Technical Journal,* vol. 14, pp. 89-104, Spr 2009.

[6] H. Suzuki, *et al.*, "Application of super-DWDM technologies to terrestrial terabit transmission systems," *Journal of Lightwave Technology,* vol. 24, pp. 1998-2005, May 2006.

[7] L. S. Tamil and A. Fumagalli, "Multi-Terabit hybrid photonic switching and routing - art. no. 60221N," in *Network Architectures, Management, and Applications III, Pts 1 and 2.* vol. 6022, K. W. Cheung, *et al.*, Eds., ed, 2005, pp. N221-N221.

[8] A. R. Chraplyvy and R. W. Tkach, "Terabit/second transmission experiments," *IEEE Journal of Quantum Electronics,* vol. 34, pp. 2103-2108, Nov 1998.

[9] R. A. Barry, *et al.*, "All-optical network consortium - Ultrafast TDM networks," *IEEE Journal on Selected Areas in Communications,* vol. 14, pp. 999-1013, Jun 1996.

[10] S. Seung-Woo, *et al.*, "Transparent optical networks with time-division multiplexing," *Selected Areas in Communications, IEEE Journal on,* vol. 14, pp. 1039-1051, 1996.

[11] M. A. F. Roelens, *et al.*, "Flexible and Reconfigurable Time-Domain Demultiplexing of Optical Signals at 160 Gb/s," *Photonics Technology Letters, IEEE,* vol. 21, pp. 618-620, 2009.

[12] C. Schmidt-Langhorst, *et al.*, "Terabit/s single-carrier transmission systems based on coherent time-division demultiplexing," in *Optical Fiber Communication (OFC),*

collocated National Fiber Optic Engineers Conference, 2010 Conference on (OFC/NFOEC), 2010, pp. 1-3.

[13] S. Bloom, *et al.*, "Understanding the performance of free-space optics [Invited]," *J. Opt. Netw.*, vol. 2, pp. 178-200, 2003.

[14] V. W. S. Chan, "Free-space optical communications," *Journal of Lightwave Technology*, vol. 24, pp. 4750-4762, Dec 2006.

[15] K. Kazaura, *et al.*, "Performance evaluation of next generation free-space optical communication," *IEICE Transactions on Electronics*, vol. E90C, pp. 381-388, Feb 2007.

[16] P. T. Dat, *et al.*, "Studies on characterizing the transmission of RF signals over a turbulent FSO link," *Optics Express*, vol. 17, pp. 7731-7743, May 2009.

[17] C. J. Karlsson, *et al.*, "All-Fiber Multifunction Continuous-Wave Coherent Laser Radar at 1.55 ?m for Range, Speed, Vibration, and Wind Measurements," *Appl. Opt.*, vol. 39, pp. 3716-3726, 2000.

[18] V. Philippov, *et al.*, "High-energy in-fiber pulse amplification for coherent LIDAR applications," *Opt. Lett.*, vol. 29, pp. 2590-2592, 2004.

[19] P. W. Juodawlkis, *et al.*, "Advances in 1.5-mu m InGaAsP/InP slab-coupled optical waveguide amplifiers (SCOWAs)," in *2007 IEEE Leos Annual Meeting Conference Proceedings, Vols 1 and 2*, ed, 2007, pp. 309-310.

[20] J. J. Plant, *et al.*, *Improving the Efficiency of High-Power Semiconductor Optical Amplifiers*, 2008.

[21] P. W. Juodawlkis, *et al.*, "Packaged 1.5-mu m Quantum-Well SOA With 0.8-W Output Power and 5.5-dB Noise Figure," *IEEE Photonics Technology Letters*, vol. 21, pp. 1208-1210, Sep 2009.

[22] Marcatil.Ea, "Slab-coupled waveguides," *Bell System Technical Journal*, vol. 53, pp. 645-674, 1974.

[23] P. W. Juodawlkis, *et al.*, *Narrow-linewidth, high-power 1556-nm slab-coupled optical waveguide external-cavity laser*, 2005.

[24] J. Klamkin, *et al.*, "Directly modulated narrowband slab-coupled optical waveguide laser," *Electronics Letters*, vol. 46, pp. 522-C55, Apr 2010.

[25] S. Gee, *et al.*, "Intracavity dispersion effect on timing jitter of ultralow noise mode-locked semiconductor based external-cavity laser," *Optics Letters*, vol. 34, pp. 238-240, Feb 2009.

[26] S. Ozharar, *et al.*, *Ultra Stable Coupled Optoelectronic Oscillator based on Slab-Coupled Optical Waveguide Amplifier*, 2008.

[27] J. J. Plant, *et al.*, "High power 1.5-mu m InGaAsP/InP colliding-pulse mode-locked slab-coupled optical waveguide laser," in *2006 IEEE LEOS Annual Meeting Conference Proceedings, Vols 1 and 2*, ed, 2006, pp. 794-795.

[28] F. R. Ahmad, *et al.*, "Energy limits imposed by two-photon absorption for pulse amplification in high-power semiconductor optical amplifiers," *Optics Letters,* vol. 33, pp. 1041-1043, May 2008.

[29] P. W. Juodawlkis, *et al.*, "Continuous-wave two-photon absorption in a Watt-class semiconductor optical amplifier," *Optics Express,* vol. 16, pp. 12387-12396, Aug 2008.

[30] R. M. De La Rue and Ieee, "Sensitive Silicon and Silica Based Photonics," in *2009 IEEE Leos Annual Meeting Conference Proceedings, Vols 1and 2*, ed, 2009, pp. 63-64.

[31] M. Hochberg and T. Baehr-Jones, "Towards fabless silicon photonics," *Nature Photonics,* vol. 4, pp. 492-494, Aug 2010.

[32] B. Jalali, "Silicon photonics Nonlinear optics in the mid-infrared," *Nature Photonics,* vol. 4, pp. 506-508, Aug 2010.

[33] J. Leuthold, *et al.*, "Nonlinear silicon photonics," *Nature Photonics,* vol. 4, pp. 535-544, Aug 2010.

[34] G. Overton, "Silicon photonics Cascaded microrings convert laser pulses for wireless communication," *Laser Focus World,* vol. 46, pp. 19-+, May 2010.

[35] G. T. Reed, *et al.*, "Silicon Photonics: Optical modulators," in *Quantum Sensing and Nanophotonic Devices Vii*. vol. 7608, M. Razeghi, *et al.*, Eds., ed, 2010.

[36] R. Won and M. Paniccia, "Integrating silicon photonics," *Nature Photonics,* vol. 4, pp. 498-499, Aug 2010.

[37] W. A. Zortman, *et al.*, "Silicon photonics manufacturing," *Optics Express,* vol. 18, pp. 23598-23607, Nov 2010.

[38] G. Tallents, *et al.*, "Optical lithography: Lithography at EUV wavelengths," *Nat Photon,* vol. 4, pp. 809-811, 2010.

[39] A. V. Krishnamoorthy, *et al.*, "Optical Proximity Communication With Passively Aligned Silicon Photonic Chips," *IEEE Journal of Quantum Electronics,* vol. 45, pp. 409-414, Apr 2009.

[40] A. V. Krishnamoorthy, *et al.*, "Computer Systems Based on Silicon Photonic Interconnects," *Proceedings of the IEEE,* vol. 97, pp. 1337-1361, Jul 2009.

[41] A. S. Liu, *et al.*, "Wavelength Division Multiplexing Based Photonic Integrated Circuits on Silicon-on-Insulator Platform," *IEEE Journal of Selected Topics in Quantum Electronics,* vol. 16, pp. 23-32, Jan-Feb 2010.

[42] R. A. Soref and B. R. Bennett, "Electrooptical effects in silicon," *IEEE Journal of Quantum Electronics,* vol. 23, pp. 123-129, Jan 1987.

[43] R. A. Soref, "Silicon-based optoelectronics," *Proceedings of the IEEE,* vol. 81, pp. 1687-1706, Dec 1993.

[44] H. Yamada, *et al.*, "Nonlinear-optic silicon-nanowire waveguides," *Japanese Journal of Applied Physics Part 1-Regular Papers Brief Communications & Review Papers,* vol. 44, pp. 6541-6545, Sep 2005.

[45] B. Jalali and S. Fathpour, "Silicon photonics," *Journal of Lightwave Technology,* vol. 24, pp. 4600-4615, Dec 2006.

[46] B. Jalali, *et al.*, "Silicon photonics," *IEEE Microwave Magazine,* vol. 7, pp. 58-68, Jun 2006.

[47] R. Soref, "The past, present, and future of silicon photonics," *IEEE Journal of Selected Topics in Quantum Electronics,* vol. 12, pp. 1678-1687, Nov-Dec 2006.

[48] C. Koos, *et al.*, "Nonlinear silicon-on-insulator waveguides for all-optical signal processing," *Optics Express,* vol. 15, pp. 5976-5990, May 2007.

[49] Q. Lin, *et al.*, "Nonlinear optical phenomena in silicon waveguides: modeling and applications," *Opt. Express,* vol. 15, pp. 16604-16644, 2007.

[50] T. Okubo, *et al.*, *Nonlinear-optical waveguide on a silicon platform*, 2007.

[51] P. Sanchis, *et al.*, "Design of silicon-based slot waveguide configurations for optimum nonlinear performance," *Journal of Lightwave Technology,* vol. 25, pp. 1298-1305, May 2007.

[52] K. Christian, *et al.*, "Highly-Nonlinear Silicon Photonic Slot Waveguide," 2008, p. PDP25.

[53] H. K. Tsang and Y. Liu, "Nonlinear optical properties of silicon waveguides," *Semiconductor Science and Technology,* vol. 23, Jun 2008.

[54] T. Vallaitis, *et al.*, "Optical properties of highly nonlinear silicon-organic hybrid (SOH) waveguide geometries," *Optics Express,* vol. 17, pp. 17357-17368, Sep 2009.

[55] B. Corcoran, *et al.*, "Nonlinear loss dynamics in a silicon slow-light photonic crystal waveguide," *Optics Letters,* vol. 35, pp. 1073-1075, Apr 2010.

[56] I. D. Rukhlenko, *et al.*, "Nonlinear Silicon Photonics: Analytical Tools," *IEEE Journal of Selected Topics in Quantum Electronics,* vol. 16, pp. 200-215, Jan-Feb 2010.

[57] R. Soref, "Mid-infrared photonics in silicon and germanium," *Nature Photonics,* vol. 4, pp. 495-497, Aug 2010.

[58] A. Ben-Yakar and F. Bourgeois, "Ultrafast laser nanosurgery in microfluidics for genome-wide screenings," *Current Opinion in Biotechnology,* vol. 20, pp. 100-105, Feb 2009.

[59] M. Gu, *et al.*, "Ultrafast biophotonics," *Journal of Optics,* vol. 12, Aug 2010.

[60] D. Bruneel, *et al.*, "Micromachining of metals with ultra-short Ti-Sapphire lasers: Prediction and optimization of the processing time," *Optics and Lasers in Engineering,* vol. 48, pp. 268-271, Mar 2010.

[61] M. Mielke, *et al.*, "Ultrafast Fiber Laser Platform for Advanced Materials Processing," *Journal of Laser Micro Nanoengineering,* vol. 5, pp. 53-58, Feb 2010.

[62] J. Kim and F. X. Kartner, "Attosecond-precision ultrafast photonics," *Laser & Photonics Reviews,* vol. 4, pp. 432-456, May 2010.

[63] T. Udem, *et al.*, "Optical frequency-comb generation and high-resolution laser spectroscopy," in *Few-Cycle Laser Pulse Generation and Its Applications*. vol. 95, ed Berlin: Springer-Verlag Berlin, 2004, pp. 295-316.

[64] S. T. Cundiff, *et al.*, "Optical frequency synthesis based on mode-locked lasers," *Review of Scientific Instruments,* vol. 72, pp. 3749-3771, Oct 2001.

[65] J. Ye, *et al.*, "Applications of ferntosecond laser comb to nonlinear molecular spectroscopy," in *Astrophysics, Clocks and Fundamental Constants*. vol. 648, S. G. Karshenboim, Ed., ed, 2004, pp. 275-295.

[66] T. H. Tsai, *et al.*, "Frequency comb swept lasers," *Optics Express,* vol. 17, pp. 21257-21270, Nov 2009.

[67] D. C. Adler, *et al.*, "In vivo endomicroscopy using three-dimensional optical coherence tomography and Fourier Domain Mode Locked lasers - art. no. 684708," in *Coherence Domain Optical Methods and Optical Coherence Tomography in Biomedicine Xii*. vol. 6847, J. A. Izatt, *et al.*, Eds., ed, 2008, pp. 84708-84708.

[68] D. C. Adler, *et al.*, *Optical Coherence Tomography Phase Microscopy Using Buffered Fourier Domain Mode Locked (FDML) Lasers at up to 370,000 Lines per Second*, 2007.

[69] E. Ippen, *et al.*, "Optical arbitrary waveform generation," in *Lasers and Electro-Optics (CLEO) and Quantum Electronics and Laser Science Conference (QELS), 2010 Conference on*, 2010, pp. 1-2.

[70] S. T. Cundiff and A. M. Weiner, "Optical arbitrary waveform generation," *Nat Photon*, vol. 4, pp. 760-766, 2010.

[71] Z. Jiang, *et al.*, "Optical arbitrary waveform processing of more than 100 spectral comb lines," *Nat Photon*, vol. 1, pp. 463-467, 2007.

[72] Z. Jiang, *et al.*, "Line-by-line pulse shaping control for optical arbitrary waveform generation," *Opt. Express*, vol. 13, pp. 10431-10439, 2005.

[73] P. Langlois, *et al.*, "High fluence ultrafast dynamics of semiconductor saturable absorber mirrors," *Applied Physics Letters*, vol. 75, pp. 3841-3843, Dec 1999.

[74] M. Joschko, *et al.*, "Ultrafast hot-carrier dynamics in semiconductor saturable absorber mirrors," *Applied Physics Letters*, vol. 76, pp. 1383-1385, Mar 2000.

[75] J. T. Gopinath, *et al.*, "Recovery dynamics in proton-bombarded semiconductor saturable absorber mirrors," *Applied Physics Letters*, vol. 78, pp. 3409-3411, May 2001.

[76] R. Paschotta and U. Keller, "Passive mode locking with slow saturable absorbers," *Applied Physics B-Lasers and Optics*, vol. 73, pp. 653-662, Nov 2001.

[77] Y. Gan, *et al.*, "Studies on ytterbium-doped fibre laser operating in different regimes," in *4th International Symposium on Instrumentation Science and Technology*. vol. 48, J. Tan, Ed., ed, 2006, pp. 795-799.

[78] H. Byun, *et al.*, "High-repetition-rate, 491 MHz, femtosecond fiber laser with low timing jitter," *Optics Letters*, vol. 33, pp. 2221-2223, Oct 2008.

[79] V. G. Savitski, *et al.*, "Passive Mode-Locking of a Ti : Sapphire Laser by InGaP Quantum-Dot Saturable Absorber," *IEEE Photonics Technology Letters*, vol. 22, pp. 209-211, Feb 2010.

[80] P. W. Juodawlkis, *et al.*, "Optically sampled analog-to-digital converters," *Microwave Theory and Techniques, IEEE Transactions on*, vol. 49, pp. 1840-1853, 2001.

[81] G. C. Valley, "Photonic analog-to-digital converters," *Opt. Express*, vol. 15, pp. 1955-1982, 2007.

[82] F. X. Kartner, *et al.*, "Photonic analog-to-digital conversion with electronic-photonic integrated circuits," San Jose, CA, USA, 2008, pp. 689806-15.

Chapter 2

Nonlinear Optical Processes

2.1. Introduction

The optical electric field incident on a semiconductor structure interacts with the outershell electrons of the atoms and the free electrons resulting in polarization. The nonlinear polarization $P(\omega)$ at frequency ω induced by an optical signal with electric field $E(\omega)$ on a centrosymmetric semiconductor structure, can be described by [1]

$$P(\omega) = \varepsilon_0 \left(\chi^{(1)} E(\omega) + \chi^{(3)} E^3(\omega) + ... \right), \tag{2.1}$$

where ε_0 is the permittivity of vacuum, and $\chi^{(n)}$ are the nth-order susceptibility terms. While the optical susceptibilities can be tensors of order n, for simplicity, they are assumed to be scalars with real and imaginary parts. The real and imaginary parts of $\chi^{(1)}$ correspond to the refractive index, and loss or gain of the device, respectively.

The $\chi^{(3)}$ terms result in several different nonlinear optical effects such as two-photon absorption (TPA), self-phase modulation, third harmonic generation, etc. TPA, gain saturation, and free-carrier absorption (FCA) are optical effects that will be studied in this thesis using several different pump-probe techniques. These processes are examined in the following sections.

2.2. Two-photon absorption processes

When two-photons with energy below the bandgap but greater than half the band gap are incident on a semiconductor structure, they can excite an electron from the valence band to the conduction band. The excitation of the electron to a higher state can be said to be facilitated through a virtual midgap transition. However, in the presence of midgap defect states, whether created by proton-bombardment or created in the fabrication process, the electron transition takes place through actual electronics states which are created by these defects. This latter process is called two-step absorption (TSA). Because of the creation of the actual midgap states, the effects of the TSA process can be several orders of magnitude larger than the TPA process, most notably in comparing the TPA and TSA absorption coefficients of silicon and polycrystalline-silicon[2].

Although TSA may be influenced by the lifetimes of the midgap states, two-photon absorption is instantaneous and proportional to the intensity of the optical signal. An important consequence is that TPA loss may impose limitation on the pulsewidth that can be transmitted through a semiconductor waveguide structure for a given pulse energy. The free carriers generated by the TPA process may further absorb light by excitation to higher states in the conduction band. This loss is called free-carrier absorption (FCA) and is dependent on the density of carriers in the conduction band. The two-photon processes as well as free-carriers in the conduction band also result in refractive index changes in the material. The so-called optical Kerr-effect results in an intensity dependent change in the refractive index of the material. In addition, the free-carriers in the conduction band also result in a change in the index of refraction of the material which is dependent on the carrier density.

These nonlinear optical effects can be demonstrated by examining the $\chi^{(3)}$ terms in Equation (2.1) for an optical signal with an electric field described by

$$E(r,t)=\sum_{m=1}^{3}\frac{1}{2}\left(\tilde{E}_{P,m}(r,\omega_P)e^{j\omega_P t}+\tilde{E}_{S,m}(r,\omega_S)e^{j\omega_S t}+c.c.\right)\hat{e}_m\,, \tag{2.2}$$

where $\hat{e}_m$ is the unit polarization vector, $\tilde{E}_{P,m}$ and $\tilde{E}_{S,m}$ are the complex electric fields and their corresponding angular frequencies, ω_P and ω_S of the pump and probe pulses, respectively. The nth order nonlinear polarization component can be written in terms of its Fourier components using [3]:

$$P^{(n)}(r,t)=\sum_{\omega_P,\omega_S}\sum_{m=1}^{3}\hat{p}_m\left(P_{P,m}^{(n)}(r,\omega_P)e^{j(\omega_P t-k_P\cdot r)}+P_{S,m}^{(n)}(r,\omega_S)e^{j(\omega_S t-k_S\cdot r)}+c.c.\right), \tag{2.3}$$

where $P_{P,m}^{(n)}$ and $P_{S,m}^{(n)}$ can be related to the electric field components $E_{P,m}(r,\omega_P)$ and $E_{S,m}(r,\omega_S)$ by the nonlinear susceptibility terms. As discussed earlier, the third order nonlinear polarization terms are the most relevant terms to the study of the nonlinear optical effects in this thesis. Therefore, we consider as an example the case where the pump and probe pulses are both of the same frequency and both are linearly co-polarized. Therefore, substitution of Equations (2.2) and (2.3) in (2.1) to produce a nonlinear polarization at ω for a centrosymmetric crystal such as silicon while showing two of the terms that play an important part in studying the different nonlinear optical effects, results in a third-order polarization of the form

$$\begin{aligned}P^{(3)}(\omega)=&A_1\varepsilon_0\chi^{(3)}(\omega;\omega,-\omega,\omega)\left(|E_P(\omega)|^2E_S(\omega)+c.c.\right)\\&+A_2\varepsilon_0\chi^{(3)}(\omega;\omega,\omega,-\omega)\left(E_P(\omega)E_S^*(\omega)E_P(\omega)+c.c.\right)\end{aligned} \tag{2.4}$$

where A_1 and A_2 coefficients are constants and they are determined by proper summing over non-distinguishable terms[1, 3]. It is obvious from this equation that $\chi^{(3)}$ process can be considered as

an intensity-dependent variation of the $\chi^{(1)}$ process. One consequence of this nonlinear polarization then, if it has an imaginary part, is an induced absorption proportional to $|E_P(\omega)|^2$ which is in turn proportional to the intensity of the optical field. The real part of $\chi^{(3)}$ results in an intensity-dependent refractive index change, called optical Kerr-effect.

The second term in the above equation is proportional to the product of the pump and probe electric fields. This term is a result of the coherent interference between the pump and probe beams near zero time delay. Sometimes called the coherent artifact, this term is proportional in magnitude to the cross correlation term at zero time delay and contributes a factor of 2 to the magnitude of the measured response[4]. However, for a cross-polarized pump-probe measurement of population dynamics in a semiconductor, the coherent artifact diminishes to zero because of faster-than-the-pulsewidth relaxation of any transition-induced anisotropy in the excited population. The coherent artifact term is an important factor in the other components of pump-probe experiments described in this thesis.

Free-carriers generated by the TPA process results in a change of index of refraction of the material. The complex refractive index can be written as [5, 6]

$$n(I) = n_0 + n_2 I - i\frac{\lambda}{4\pi}(\alpha_{lin} + \beta I) \tag{2.5}$$

where n_0 is the refractive index of the material, n_2 is the optical Kerr coefficient, α_{lin} is the linear loss in the material, and β is the two-photon absorption coefficient. These intensity-dependent parameters are related to susceptibilities by [5]

$$\beta = \frac{-3\omega}{2c^2 n_0^2 \varepsilon_0}\mathrm{Im}\left\{\chi^{(3)}\right\} \tag{2.6}$$

$$n_2 = \frac{3}{4cn_0^2\varepsilon_0}\mathrm{Re}\left\{\chi^{(3)}\right\}, \tag{2.7}$$

where c is the speed of light in vacuum, n_0 is the refractive index and ε_0 is the vacuum permittivity. The FCA effects can also be added to the complex index of refraction of Equation (2.5) to lead the following formula:

$$n(I) = n_0 + n_2 I + \xi f_\phi(N) - i\frac{\lambda}{4\pi}\left(\alpha_{lin} + \beta I + \sigma f_\alpha(N)\right), \tag{2.8}$$

where $\xi f_\phi(N)$ and $\sigma f_\alpha(N)$ are the refractive index change and loss due to free-carriers in the conduction band with density N [7]. Several different measurement techniques have been used to extract these parameters for both direct and indirect bandgap materials. In addition to measurement techniques, models predicting the TPA and Kerr coefficients have been developed and their predictions were compared to the measured results[6].

2.3. Band-gap dependence of TPA and Kerr coefficients

The band-gap dependence of the TPA and Kerr coefficients of several different semiconductor materials have been modeled previously[6, 8]. The TPA coefficient in (cm/GW) was found to be given by[8]

$$\beta = \frac{K\sqrt{E_P}}{n^2 E_g^3} F\left(\frac{2\hbar\omega}{E_g}\right), \tag{2.9}$$

where K is empirically equal approximately to 3100 and is independent of the type of material, n is the refractive index, E_g is the bandgap of the material, E_p is nearly material independent and for most direct semiconductor materials, it is approximately 21eV, and F is a function that is dependent on the band structure and is given by[8]

$$F(2x) = \frac{(2x-1)^{3/2}}{(2x)^5} \quad for\ 2x > 1. \tag{2.10}$$

The optical Kerr-effect is similarly modeled by[8]

$$n_2 = K' \frac{G\left(\frac{\hbar\omega}{E_g}\right)}{nE_g^4}, \tag{2.11}$$

where K'=3.4×10^{-8}, E_g is the bandgap of the material, and G is a function given by the following formula:

$$G(x) = \frac{-2+6x-3x^2-x^3-\frac{1}{4}x^4-\frac{3}{4}x^5+2(1-2x)^{3/2}}{(2x)^6} \quad for\ 2x<1. \tag{2.12}$$

These models apply to direct bandgap material. In the following chapters, the effects of these nonlinear optical processes on the performance of several passive and active devices are studied. The above equations were utilized to compare the measured and theoretical TPA coefficient of InGaAsP in the slab-coupled optical waveguide amplifier (SCOWA) of Chapter 3.

2.4. References

[1] R. Boyd, *Nonlinear Optics, Third Edition*: Academic Press, 2008.

[2] K. Mehta, *et al.*, "Ehanced Two-Photon Absorption in Polycrystalline Silicon," *CLEO Conference 2011, Baltimore, MD,* vol. submitted for publication.

[3] E. P. Ippen, *Nonlinear Optics*. MIT class 6.634 class notes, Cambridge, MA 2004.

[4] E. P. Ippen and C. V. Shank, "Techniques for Picosecond Measurement," *Chapter 3, Ultrashort Light Pulses*, edited by S. Shapiro, published by Springer-Verlag, 1977.

[5] J. Leuthold, *et al.*, "Nonlinear silicon photonics," *Nat Photon,* vol. 4, pp. 535-544, 2010.

[6] M. Sheik-Bahae, *et al.*, "Dispersion and band-gap scaling of the electronic Kerr effect in solids associated with two-photon absorption," *Physical Review Letters,* vol. 65, p. 96, 1990.

[7] Q. Lin, *et al.*, "Nonlinear optical phenomena in silicon waveguides: modeling and applications," *Opt. Express,* vol. 15, pp. 16604-16644, 2007.

[8] E. W. Van Stryland, *et al.*, "Energy band-gap dependence of two-photon absorption," *Opt. Lett.,* vol. 10, pp. 490-492, 1985.

Chapter 3

Slab-Coupled Optical Waveguide Amplifiers

Abstract:

The limits imposed by two photon absorption and free-carrier absorption on the gain and output powers of an InGaAsP/InP slab-coupled optical waveguide amplifier with a confinement factor of $\Gamma = 0.5\%$ were studied. The two-photon absorption coefficient and the induced free-carrier absorption cross-section were measured to be 65cm/GW and 7×10^{-17} cm^2, respectively. The effects of two-photon absorption begin to limit the gain significantly for pulses shorter than 40ps. The carrier recovery times were observed to vary between 390 to 160ps for 1A to 4A bias currents, and the short-pulse saturation fluence of the gain was determined to be $1.4 mJ/cm^2$.

3.1. Introduction

Transmission of optical signals over long distances, whether in fiber or in free space, suffers from attenuation due to scattering and absorption. Free-space optical communication (FSO) systems also offer large data rates and have received a great deal of attention in recent years[1-4]. Optical signals transmitted over long distances must be amplified at several intervals to overcome the scattering and atmospheric losses. Eye-safe, high power optical lasers and amplifiers operating around 1.5μm can extend the transmission range and reduce the number of repeater stations. Output powers in the excess of 1W at wavelengths near 1.5μm are in demand for free space optical communication systems, optical array transmitters, and laser radar systems [5-8].

Semiconductor optical amplifiers are compact in size, have large optical bandwidths (~100nm)[9], and can produce high powers in the order of 400mW[10]. SOAs have also found application in the design of wavelength convertors and optical switches[11, 12], making them devices of choice for photonic integration leading to a single-chip optical system. Despite their advantages, SOAs exhibit poor coupling to optical fibers. An important goal of semiconductor optical amplifiers technology is to increase the single-mode output powers, both CW and pulsed, that can be produced by these compact devices.

The saturation energy of an SOA is defined as the output power where the amplifier gain has dropped by half of the small signal gain. This saturation power can be written[13]:

$$P_{0,SAT} = \left(\frac{G_0 \ln 2}{G_0 - 2}\right)\left(\frac{wd}{\Gamma}\right)\left(\frac{\hbar\omega}{a\tau}\right), \tag{3.1}$$

where G_0 is the small-signal gain of the amplifier, w and d are the width and thickness of the active material, respectively, Γ is the confinement factor, ie the overlap between the optical mode

and the active region, $\hbar\omega$ is the photon energy, a is the differential gain, and τ is the carrier lifetime. One approach to achieving such high powers is to increase the size of the optical mode in lateral(w), vertical(d), or both dimensions. This can be accomplished by a tapered waveguide which requires complex coupling optics to a single mode fiber. The other method is to decrease the confinement factor (Γ). A device that incorporates both strategies is the slab-coupled optical waveguide amplifier (SCOWA)[13]. The SCOW topology has also been applied to lasers (SCOWL) in both CW[14, 15] and mode-locked configurations[16-18]. The limitations related to two-photon absorption (TPA) in these devices have been discussed[19-22]. The low-confinement factor (<1%) increases the importance of nonlinearity in the passive waveguide relative to that of gain saturation in the active region. Furthermore, the fact that instantaneous nonlinearities such as TPA depend on peak power, whereas gain saturation depends principally on the optical energy within a population recovery time, imposes limitations on the output power in general and more severely on short pulses. In this chapter, the topology of a SCOWA is described, and the limitations imposed by the nonlinear optical processes are discussed and studied. In addition, the recovery times of one of these devices are measured as a function of the bias current to determine the maximum data rate through it.

The rest of this chapter consists of a section describing the SCOWA device physics followed by a model describing the evolution of a pulse as it propagates along the device. Because of the high input polarization dependence of a SCOWA, a double-modulated degenerate pump probe experiment was used to study the ultrafast carrier dynamics and nonlinear optical processes in a SCOWA. The description of this experimental setup is given in Section 3.3. The results of the pump probe experiment are presented in Section 3.4, including the extraction of the nonlinear parameters using both a model which is fit to the data and direct measurement using

the pump probe results. This chapter is concluded with suggested future work and a summary of the study.

3.2. SCOWA basics

Slab coupled optical waveguide amplifier design is based on Marcatili's coupled-mode analysis which demonstrated that a large multimode waveguide structure can be designed to operate in the single fundamental mode by coupling the higher order modes to the adjacent slab waveguide[23]. By incorporating an active region using quantum-well technology in an otherwise passive waveguide, an optical amplifier with large fundamental mode can be designed. An example of a schematic diagram of a SCOWA is shown in Figure 3-1 which illustrates the propagation of a single mode optical signal in the n-doped InGaAsP layer with a small overlap with the active multiple quantum-well region. Careful selection of the dimensions w, h, and t results in a structure that supports only the fundamental mode. The higher order modes are dissipated in the cladding. The optical mode of a SCOWA can be designed to match the fundamental mode of an optical fiber, hence butt-coupling efficiency in the order of 90% has been demonstrated [24].

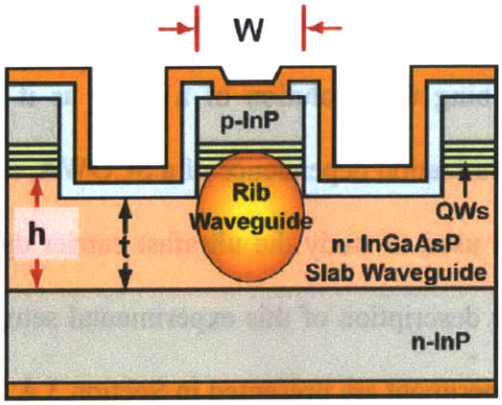

Figure 3-1 – InP based slab-coupled optical waveguide amplifier

In a SCOWA, the gain is provided by the overlap of the mode with the active region of the device, made up of p-doped multiple quantum-wells. The confinement factor Γ is designed to be in the order of 0.1 to 0.5% to achieve high saturation power (>1W). However, as the net gain coefficient of a waveguide is $g_{net} = \Gamma g_0 - \alpha_i$ (cm^{-1}), where g_0 is the active-material gain coefficient, and α_i is the intrinsic loss of the device, to achieve reasonable gains (10-15dB), the low confinement factor results in a long device. A benefit of a long device is that it facilitates heat removal, hence allowing for large bias currents to achieve higher gains and faster recovery times.

3.2.1. SCOWA device physics

The two main nonlinear optical processes, namely, two-photon absorption (TPA), and free-carrier absorption (FCA), impose limitations on the maximum achievable output power in a SCOWA device. TPA and FCA are both loss processes. To help understand their effects, the band diagram of a SCOWA is examined. The band diagram of a p-i-n SCOWA is shown in Figure 3-2, with the optical mode intensity overlayed on this diagram. The optical propagation in this figure is into and out of the page.

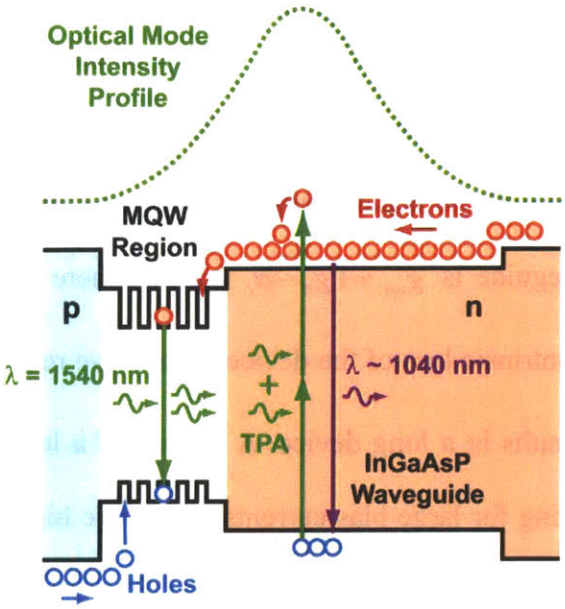

Figure 3-2 – Band diagram of a p-i-n SCOWA electronic carrier injection. Optical propagation in this figure is into and out of the page[20].

As depicted in this figure, the active region consists of a multiple quantum-well (MQW) region with a bandgap of 1540nm. This active region is placed between the p and n-doped InGaAsP regions of wider bandgap (1040nm). When the device is forward biased, the electron and holes are injected into the multiple quantum-well region of the SCOWA from the n-doped and p-doped regions, respectively. Once the carrier density in the MQW region becomes large enough, the input signals within the gain bandwidth of quantum-wells (~1540nm) experience gain through stimulated emission. As shown, the optical mode has a small overlap with the MQW region; hence the majority of the optical mode lies within the n-InGaAsP waveguide which has a bandgap of approximately 1040nm. Therefore, even as the optical signal experiences gain, the high intensity region of the optical mode self-induces loss by generation of electron-hole pairs via TPA in the waveguide. The TPA-generated carriers also cause another loss mechanism through FCA. The combination of these two mechanisms limits the maximum intensity that can be produced in these amplifiers.

3.2.2. Pulse propagation model

The pulse propagation through an active medium is a function of the material gain, the internal losses and the confinement factor. The differential equation describing pulse propagation along the length of a SCOWA is given by:

$$\frac{dI(z,t)}{dz} = I(z,t)\left[\Gamma g_m(z,t) - \alpha(z,t)\right], \tag{3.2}$$

where Γ is the confinement factor, $g_m(z,t)$ is the local material gain, and $\alpha(z,t)$ is the local loss coefficient. *I(z,t)* is defined here to be the peak intensity of the pulse and is related to the power *P(z,t)* by

$$P(z,t) = \iint I(x,y,z,t)dxdy = I(z,t)\cdot A_{mode}\,. \tag{3.3}$$

For pulses much shorter than the gain (carrier) recovery time, the local dynamic material gain, $g_m(z,t)$, can be determined from

$$g_m(z,t) = g_0 e^{-\int_{-\infty}^{t} d\tau I(z,\tau)/F_{sat}}, \tag{3.4}$$

where g_0 is the unsaturated small signal gain, and F_{sat} is the pulse saturation energy density related to the saturation energy, E_{sat}, by $F_{sat} = E_{sat}/A_{mode}$. We note that the gain is not constant over the duration of a pulse and that this can result in pulse shape changes.

The loss, $\alpha(z,t)$, is a sum of several mechanisms:

$$\alpha(z,t) = \alpha_{TPA}(z,t) + \alpha_{2FCA}(z,t) + \alpha_{\text{int}}\,. \tag{3.5}$$

The internal loss, α_{int}, is a property of the constituent material and can be approximated to be uniform along the length of the device and independent of optical power. The two-photon loss is a function of the incident intensity and is described by

$$\alpha_{TPA}(z,t) = \beta' I(z,t), \tag{3.6}$$

where β' differs from the plane wave TPA coefficient β according to

$$\beta' = \beta \frac{\iint I^2(x,y,z,t)dxdy}{I^2(z,t)\cdot A_{mode}}. \tag{3.7}$$

This is equivalent to defining an effective area for a Gaussian mode as described in [19] and for a Gaussian mode profile this results in $\beta' = \beta/2$.

In addition to TPA loss, the free carriers generated by this process can further absorb energy from the incident beam. This free-carrier absorption (FCA) depends on the square of the intensity of the pulse and, for pulses much shorter than the carrier lifetime and diffusion time, the FCA loss can be expressed by:

$$\alpha_{2FCA}(z,t) = \int_{-\infty}^{t} \sigma' \frac{\beta I^2(z,\tau)}{\hbar\omega} d\tau, \tag{3.8}$$

where $\hbar\omega$ is the incident photon energy. The effective FCA cross-section σ' used in this expression is related to the plane wave cross section σ by

$$\sigma' = \sigma \frac{\iint I^3(x,y,z,t)dxdy}{I^3(z,t)\cdot A_{mode}} \tag{3.9}$$

For a Gaussian mode profile $\sigma' = \sigma/3$.

Using the above definitions, the differential equation of (3.2) can be written as:

$$\frac{dI(z,t)}{dz} = I(z,t)\left[\Gamma g_0 e^{-\int_{-\infty}^{t} d\tau I(z,\tau)/F_{sat}} - \beta' I(z,t) - \int_{-\infty}^{t} \sigma' \frac{\beta I^2(z,\tau)}{\hbar\omega} d\tau - \alpha_{\text{int}}\right]. \tag{3.10}$$

This differential equation was solved numerically for different pulse energies. The result of this analysis is compared to the measured data and presented in Section 3.4.

3.2.3. SCOWA Device Structure

The devices used in this study are InGaAsP/InP slab-coupled optical waveguide amplifiers fabricated at the MIT Lincoln Laboratory. They were grown on n-type InP substrate using organic-metallic vapor-phase epitaxy method, and consist of n-InP cladding layers of 1μm thickness. The device waveguide is constructed from a lightly-doped n-InGaAsP layer with 5μm thickness. The active region consists of 5 compressively strained (1%) InGaAsP quantum wells of 8nm thickness with composition yielding a peak photoluminescence at 1530nm[20]. The lateral confinement is achieved by etching a strip-loaded waveguide into the InGaAsP waveguide with a width of 5.4μm and depth of 0.5μm. As a result, the fundamental mode of the optical wave in this structure is 5×7μm comparable to the mode size of single-mode fiber. To minimize the optical feedback into the device, and hence lasing, the output facets were cleaved at a 5 degree angle. The device is then mounted on a copper baseplate with a thermoelectric cooler to stabilize the temperature of the device. Figure 3-3 depicts the actual device as mounted on a metal block. The optical input is coupled into the device using a lensed-tip fiber, and the output is collected using a high NA lens.

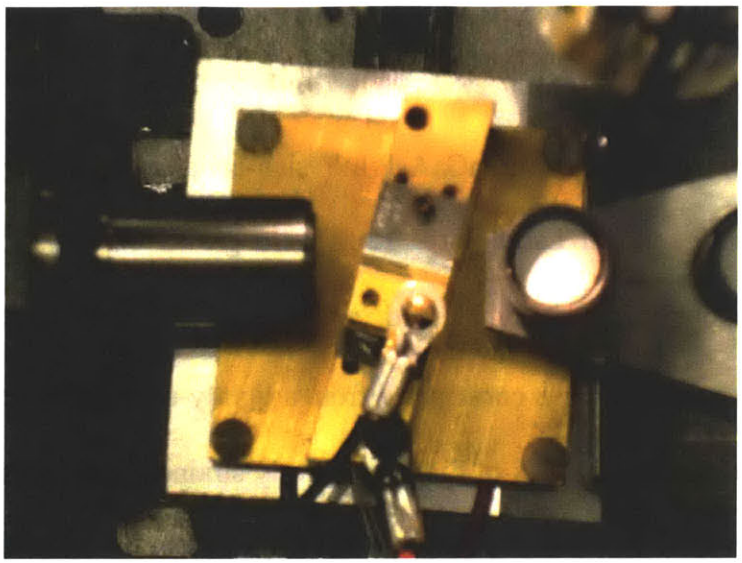

Figure 3-3 – SCOWA device mounted on a copper plate in the center of the picture. The mount on the right hand side of the picture contains a lens-fiber to couple light into the device. The output is collected using a large NA lens as shown on the left hand side of the picture.

3.3. Experimental Setup

To study the ultrafast nonlinear processes and the recovery times of a SCOWA, a pump probe experiment is utilized. Because of the large polarization dependence of the gain of the SCOWA (~20dB), a degenerate double-chopped pump-probe experiment as shown in Figure 3-4 was set up. The optical source is an optical parametric oscillator (OPO) pumped by a femtosecond Ti:Sapphire laser (Spectra-Physics MaiTai and OPAL). The output wavelength of the OPO can be tuned between 1100 and 1600nm. The output pulses are 150fs in duration with the repetition rate of 80 MHz.

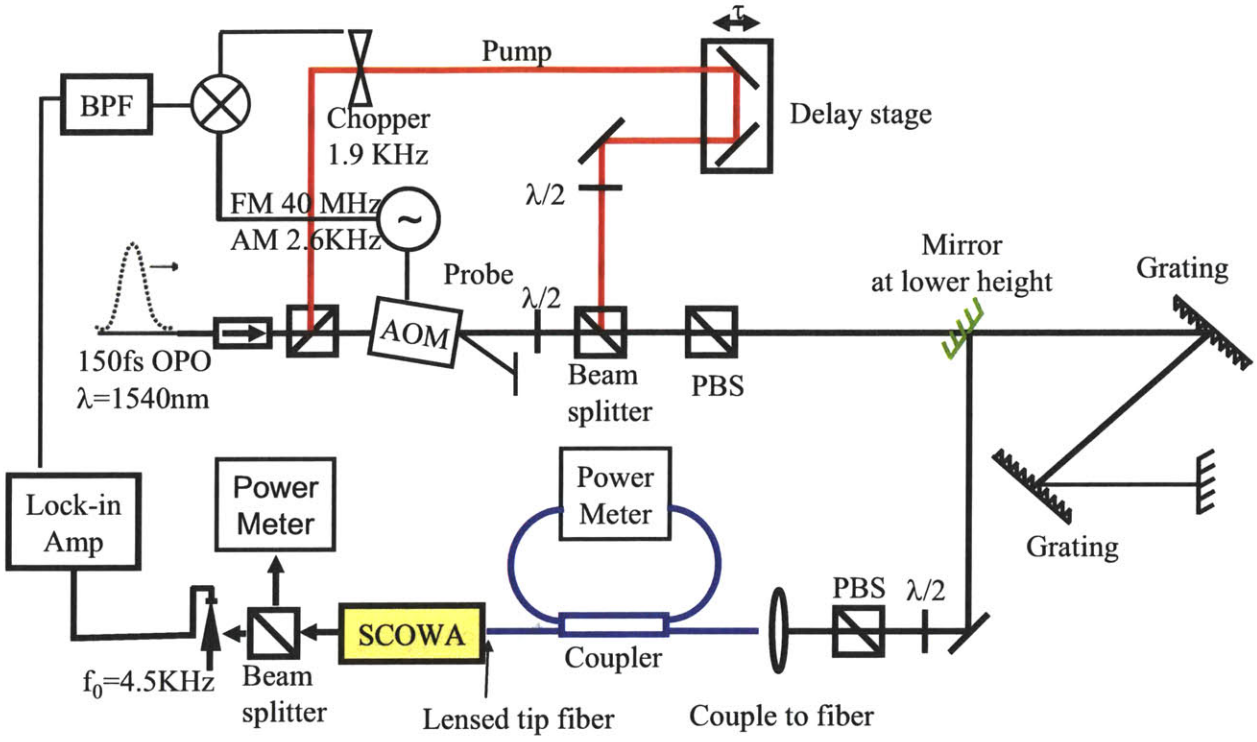

Figure 3-4 – Double-chopped degenerate pump probe setup

The light from this laser source is split into two paths, the pump and the probe, at the ratio of 70:30, respectively. The pump path traverses through an optical delay stage, and is recombined with the probe at the beam splitter with the same polarization. The pump is chopped at 1.9KHz, and the probe at 2.6KHz. Two halfwave plates, one in each arm of the pump and the probe signals, in combination with a polarization beam splitter are used as variable attenuators to control the incident pump and probe power levels. The pump and probe beams are passed through a double-pass grating pair separated by a variable distance *D*. The grating pair is used to stretch the 150fs pulses from the OPO, to pulses with duration in the range of 1.4ps to 40ps. These stretched pulses are then utilized to study the effects of the nonlinear optical processes in a SCOWA, as a function of the signal pulsewidth.

The stretched pulses are then coupled to a short length of fiber and a polarization controller. To monitor the optical power that is coupled into the SCOWA, the combined pump-probe pulses are passed through a 10:90 coupler with the 10% port used to monitor the input power. A lensed-tip fiber with mode profile matching that of a SCOWA is utilized to couple the incident light to the SCOWA. The amplified light from the output of the SCOWA is collected with a high NA lens and passed through a 50:50 beam splitter. One port is utilized for measuring the absolute power, while the other port is connected to a lock-in amplifier where the magnitude of the signal at the sum of the two chopping frequencies, i.e. 4.5KHz is measured. The 4.5KHz reference signal is generated by mixing and filtering the pump and probe chopping frequencies. This method ensures that any variations in the probe chopping frequency caused by the mechanical chopper are tracked by the lock-in amplifier. The detected signal from the lock-in amplifier is collected and analyzed later.

This setup was further utilized to make direct gain measurements of the SCOWA as a function of the pulsewidth and input power. For this, the probe path was blocked, and the output of the SCOWA was detected using the power meter and the lock-in amplifier. In the direct gain measurement, the combination of chopper and lock-in amplifier technique eliminates the offset due to the ASE.

3.4. Results and Discussion

The pump-probe traces as a function of the pulse energy for 10ps pulses are shown in Figure 3-5. In double-chopped pump-probe, unlike in cross-polarized and heterodyne pump-probe techniques, at low powers, the traces are symmetric around t=0. The symmetric pump probe traces is an inherent property of the double-chopped pump probe technique when the pump and

the probe are not optically separated. When the probe is leading the pump, the probe induces changes on the pump at its chopping frequency, and vice versa. Since the product of the pump and probe signals is measured, the resulting trace is symmetric around t=0. This symmetry holds for low powers.

As shown in Figure 3-5, the pump-probe data yielded an instantaneous induced absorption followed by a longer recovery time of the depleted gain. The large induced absorption at zero time delay consists of two components: the smaller component which is due to the depletion of the carrier as the pump and the probe signals get amplified in the device, and the larger component is due to the two-photon absorption when the pump and probe are perfectly overlapped in time domain. This instantaneous response is followed by a slow gain recovery time which is a function of the carrier lifetime in the device. As a result, the pump probe traces are the result of the convolution of the device transfer function and the pulse. The transfer function of the device can be modeled using

$$h(t) = a_0 \delta(t) + a_1 e^{-t/\tau_r} u(t), \tag{3.11}$$

where a_0 is the amplitude of the instantaneous response and it is proportional to the TPA induced effect, a_1 is a function of the FCA loss which is a function of the number of free-carriers, $u(t)$ is a unit step function, and τ_r is the carrier recovery time of the device.

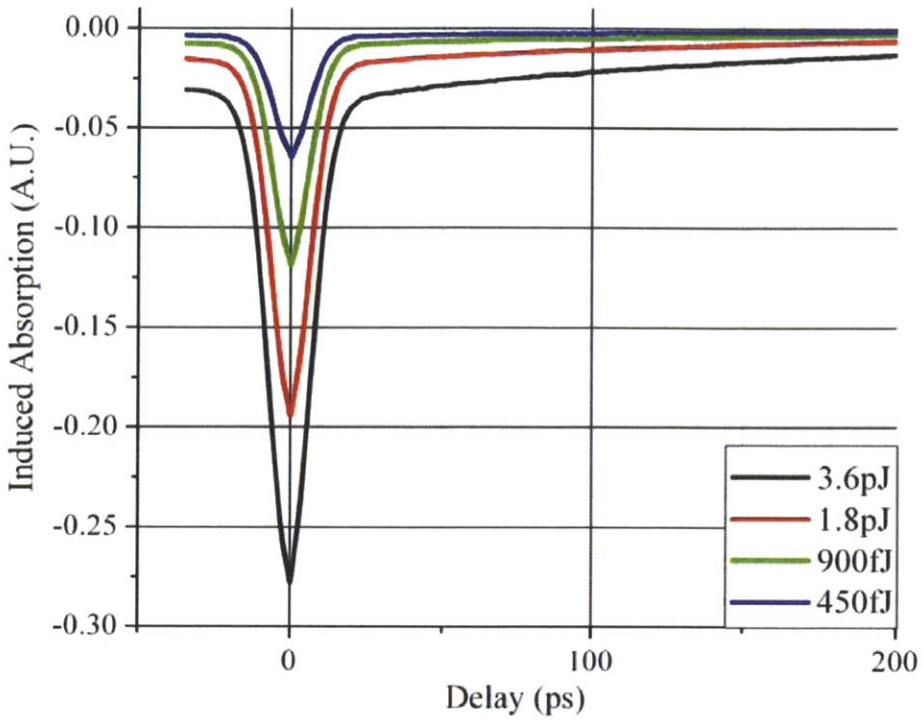

Figure 3-5 – Double-chopped pump traces of the SCOWA device with 10ps pulses. Consists of TPA induced absorption at the delay, t=0, and long a recovery time.

As Figure 3-5 shows, the induced loss due to the TPA process is proportional to pulse energy for a fixed 10ps pulse duration. As demonstrated in Figure 3-6, for the same pulse energy, the induced absorption due to the TPA decreases with increasing pulsewidth as expected for a process that depends on peak intensity. From the same figure, we can see that after about 60ps, the longer-lived gain compression is the same for all pulse durations since the number of carriers depleted as a result of the stimulated emission depends only on total pulse energy which is the same for all traces.

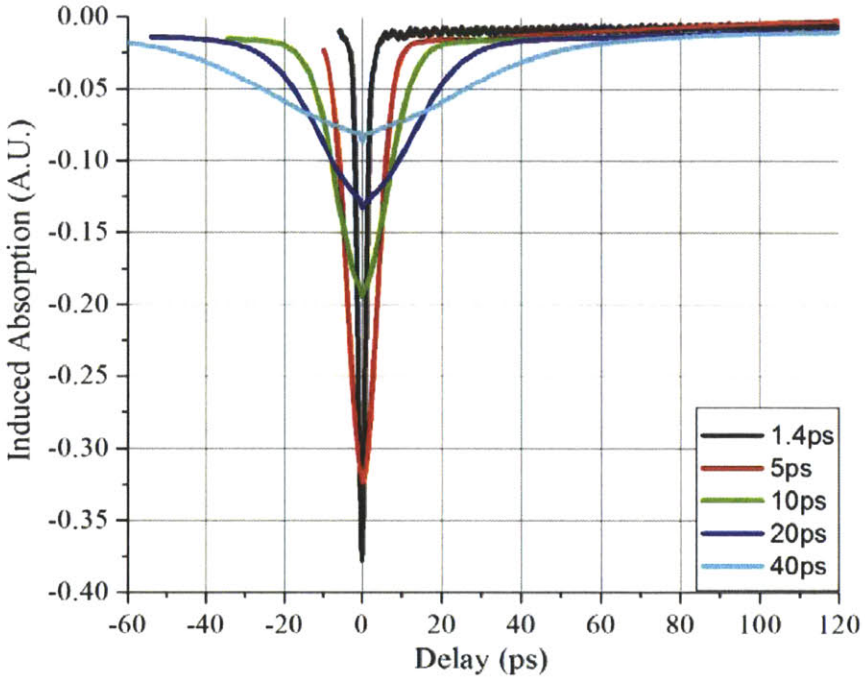

Figure 3-6 – Induced absorption as a function of input pulsewidth. The input energy of each pulse is 1.8pJ.

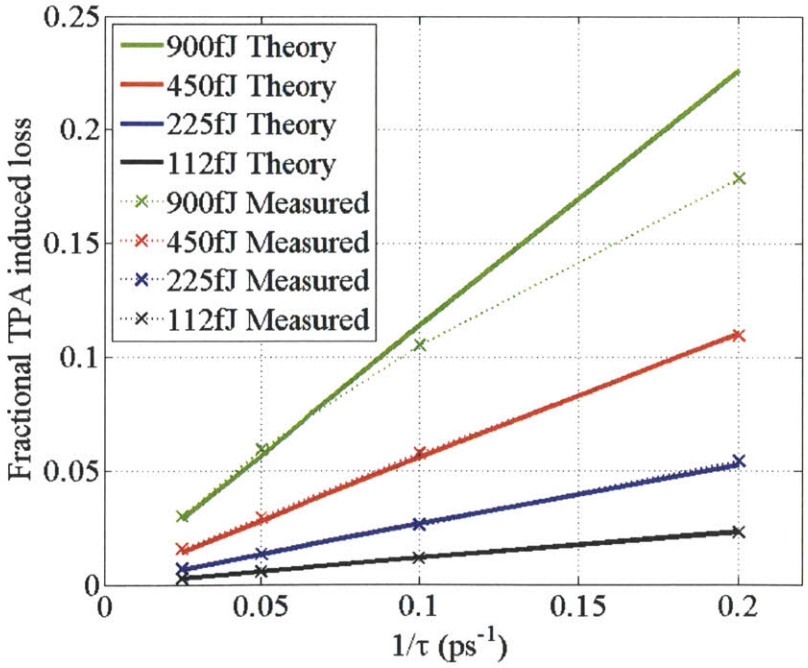

Figure 3-7 – Fractional TPA induced loss as a function of inverse pulsewidth, measured vs theory.

The peak value of the instantaneous TPA loss was measured for different pulse widths at a 4A bias current. With adjustment for the coherent artifact at t=0[25], the results are plotted in Figure 3-7 as a function of inverse pulse width $1/\tau$. For a given input pulse energy, absorption due to TPA is expected to vary linearly with $1/\tau$ given by (Appendix A):

$$\frac{\Delta I_s}{I_s(L)} = -2\beta\left(\frac{1-e^{-g\Gamma L}}{g\Gamma L}\right) L I_p(L)\cos(\omega_1+\omega_2)t \propto \frac{E}{\tau} \tag{3.12}$$

where I_p is the pump intensity, ω_1 and ω_2 are the pump and probe chopping frequencies, L is the length of the device, g is the material gain, Γ is the confinement factor, and β is the two photon absorption coefficient. For pulse energies below 900fJ, there is an excellent agreement between the above formula and the measured results. From this figure and the slope of the line, the TPA coefficient was measured to be 65cm/GW. However, at higher pulse energies, the curves deviate due to higher order effects such as absorption of the pump and induced FCA losses. This is evident in Figure 3-7 for the input energy of 900 fJ.

In addition to the nonlinear optical process, from the pump-probe traces, we can determine the gain recovery times of the SCOWA. The longer gain recovery characteristic was studied at different bias currents for a time delay of up to 400ps. The results, shown in Figure 3-8, reveal a recovery time that varies from 390ps at 1A to 160ps at 4A. These measurements are important for the design of modelocked systems and also provide an accurate determination of the relative magnitudes of the ultrafast TPA response and the carrier depletion. At the higher pulse energies the additional gain suppression due to FCA is also evident on this time scale.

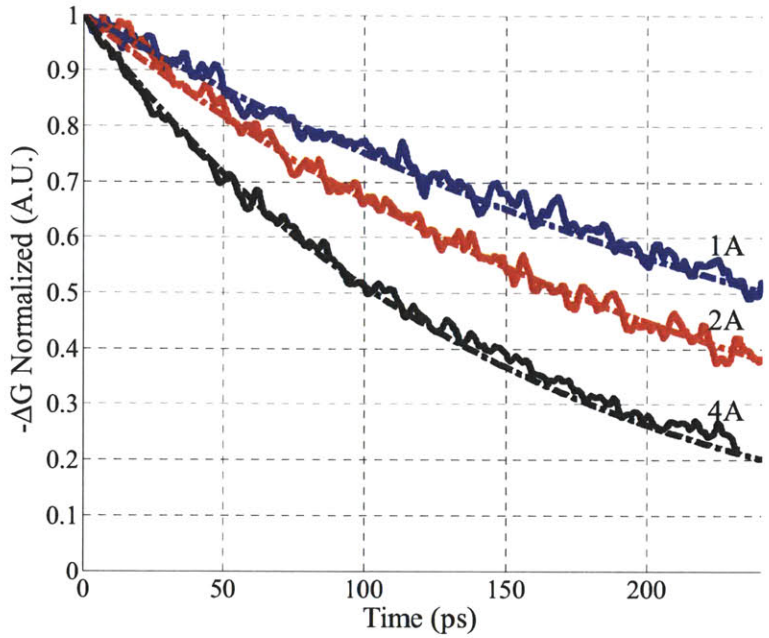

Figure 3-8 – Carrier recovery times of the SCOWA as a function of the bias current.

The net saturated gain of the device, biased at 4A, was measured as a function of input pulse energy, for several different input pulse durations. The results are shown by the dotted lines in Figure 3-9. These measurements demonstrate that the 3dB gain roll off moves to lower pulse energies as pulse duration is decreased. This can be directly attributed to the effects of the TPA and FCA losses which are proportional to the intensity and the square of the pulse intensity, respectively. The solid lines in Figure 3-9 are the results of simulations of pulse propagation through the device using the analysis described in Section 3.2.2. The close fit between the simulations and the measured results were achieved with a single set of parameters for all curves: unsaturated gain g_0 = 640/cm, confinement factor Γ = 0.5%, material loss α_{int} = 0.5/cm, FCA effective cross section σ = 7x10^{-17} cm^2, saturation energy density, F_{sat} = 1.4mJ/cm^2, and TPA coefficient, β = 65cm/GW. The resulting TPA coefficient of 65cm/GW is in close agreement with the calculation of the TPA coefficient based on its dependence on the inverse cube of the

bandgap energy[26], assuming the TPA coefficient of InP as reported in[27]. The FCA effective cross section, σ is in close agreement with the value reported in[20]. The small deviations between the measured and simulated results at high pulse energies may be due to the pulse shaping in the amplifier due to self-phase modulation and dispersion. The instantaneous components in the pump-probe data at low energy show that dispersion by itself is not a significant factor.

The 3dB saturation-energy level which is defined to be the input energy level that results in the gain of the device to be half of that of the small-signal linear region is calculated and its difference with respect to an ideal case where there is no TPA or FCA in the device is determined. The result of this calculation is shown in Figure 3-10. As can be seen in this figure, the 3dB input energy level is decreased dramatically at very short pulsewidths (150fs). In fact, even at very low input pulse energies, the effects of the TPA can be observed.

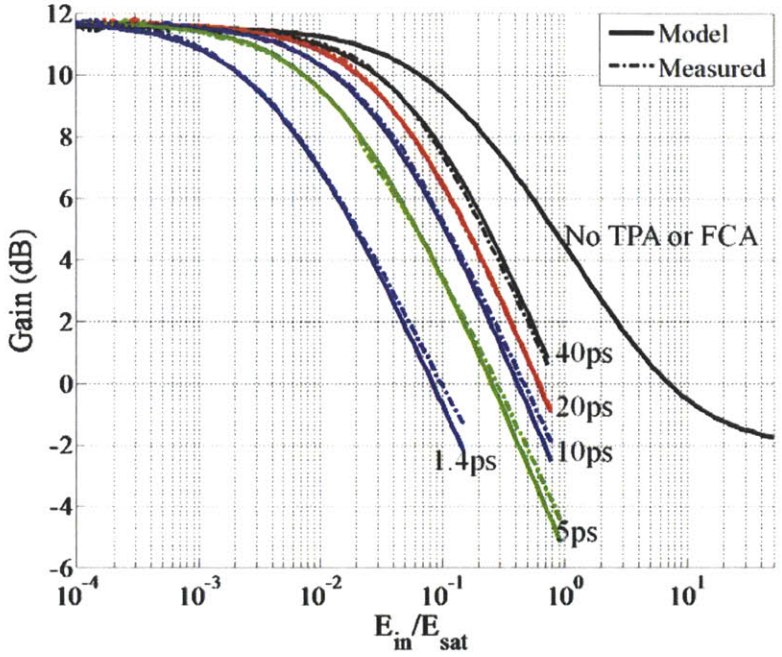

Figure 3-9 – SCOWA gain dynamics at 4A bias current. The dashed lines are the measured data and the solid lines are the modeled results.

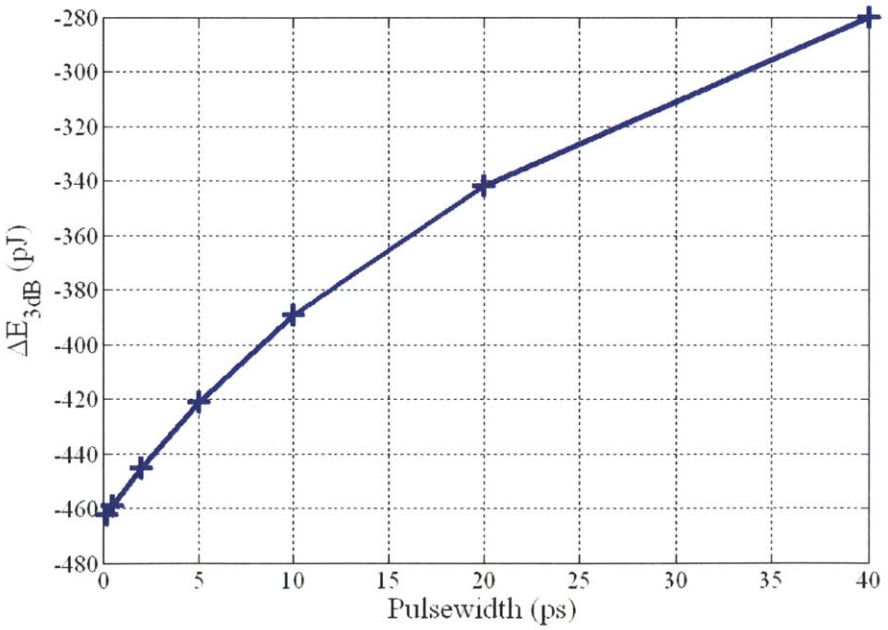

Figure 3-10 – 3dB gain roll-off penalty relative to a SCOWA with zero TPA and FCA effects, as a function of the input pulsewidth.

3.5. Conclusion

In this chapter, the limitations imposed on the saturation output power of a SCOWA device by TPA and FCA processes, have been demonstrated. The quantities of the ultrafast nonlinear coefficients were determined. A model was developed to predict the saturation energy of the amplifier as a function of the input pulsewidth. The gain of the SCOWA rolls-off at very low input pulse energy levels for pulses of 150fs, and it becomes a challenge to produce significant output energy to transmit such pulses over long distances. This also creates a challenge to design femtosecond mode-locked lasers using SCOWAs. Solutions to reduce the effects of the TPA may facilitate implementation of these amplifiers in the ultrafast optical systems. A solution may be to construct the slab layer, where the optical intensity is the highest, from higher bandgap materials compatible with the InP technology.

3.6. References

[1] S. Bloom, *et al.*, "Understanding the performance of free-space optics [Invited]," *J. Opt. Netw.*, vol. 2, pp. 178-200, 2003.

[2] V. W. S. Chan, "Free-space optical communications," *Journal of Lightwave Technology,* vol. 24, pp. 4750-4762, Dec 2006.

[3] P. T. Dat, *et al.*, "Studies on characterizing the transmission of RF signals over a turbulent FSO link," *Optics Express,* vol. 17, pp. 7731-7743, May 2009.

[4] K. Kazaura, *et al.*, "Performance evaluation of next generation free-space optical communication," *IEICE Transactions on Electronics,* vol. E90C, pp. 381-388, Feb 2007.

[5] F. Amzajerdian, *et al.*, "Utilization of 3-D Imaging Flash Lidar Technology for Autonomous Safe Landing on Planetary Bodies," *Quantum Sensing and Nanophotonic Devices Vii,* vol. 7608, 2010.

[6] C. J. Karlsson, *et al.*, "All-Fiber Multifunction Continuous-Wave Coherent Laser Radar at 1.55 ?m for Range, Speed, Vibration, and Wind Measurements," *Appl. Opt.,* vol. 39, pp. 3716-3726, 2000.

[7] V. Philippov, *et al.*, "High-energy in-fiber pulse amplification for coherent lidar applications," *Opt. Lett.,* vol. 29, pp. 2590-2592, 2004.

[8] T. D. Vu, *et al.*, "Grid-based localization and local mapping with moving object detection and tracking," *Information Fusion,* vol. 12, pp. 58-69, 2011.

[9] A. Tomoyuki, *et al.*, "An ultrawide-band (120 nm) semiconductor optical amplifier having an extremely-high penalty-free output power of 23 dBm realized with quantum-dot active layers," 2004, p. PD12.

[10] M. Mikhail, *et al.*, "High power InGaAsP/InP broad-waveguide single-mode ridge-waveguide lasers," 2001, p. WC2.

[11] S. A. Hamilton and B. S. Robinson, "40-Gb/s all-optical packet synchronization and address comparison for OTDM networks," *IEEE Photonics Technology Letters,* vol. 14, pp. 209-211, Feb 2002.

[12] J. P. Wang, *et al.*, *40-Gbit/s all-optical header processing for packet routing*, 2006.

[13] G. P. Agrawal and N. K. Dutta, *Semiconductor lasers*, 2nd ed. New York: Van Nostrand Reinhold, 1993.

[14] P. W. Juodawlkis, *et al.*, *Narrow-linewidth, high-power 1556-nm slab-coupled optical waveguide external-cavity laser*, 2005.

[15] J. Klamkin, *et al.*, "Directly modulated narrowband slab-coupled optical waveguide laser," *Electronics Letters,* vol. 46, pp. 522-C55, Apr 2010.

[16] S. Gee, *et al.*, "Intracavity dispersion effect on timing jitter of ultralow noise mode-locked semiconductor based external-cavity laser," *Optics Letters,* vol. 34, pp. 238-240, Feb 2009.

[17] S. Ozharar, *et al.*, *Ultra Stable Coupled Optoelectronic Oscillator based on Slab-Coupled Optical Waveguide Amplifier*, 2008.

[18] J. J. Plant, *et al.*, "High power 1.5-mu m InGaAsP/InP colliding-pulse mode-locked slab-coupled optical waveguide laser," in *2006 IEEE LEOS Annual Meeting Conference Proceedings, Vols 1 and 2*, ed, 2006, pp. 794-795.

[19] F. R. Ahmad, *et al.*, "Energy limits imposed by two-photon absorption for pulse amplification in high-power semiconductor optical amplifiers," *Optics Letters,* vol. 33, pp. 1041-1043, May 2008.

[20] P. W. Juodawlkis, *et al.*, "Continuous-wave two-photon absorption in a Watt-class semiconductor optical amplifier," *Optics Express,* vol. 16, pp. 12387-12396, Aug 2008.

[21] A. R. Motamedi, *et al.*, "Ultrafast nonlinearities and gain dynamics in high-power semiconductor amplifiers," *Applied Physics Letters,* vol. 93, 2008.

[22] A. R. Motamedi, *et al.*, "Nonlinear Absorption and Carrier Dynamics in Slab-Coupled Optical Waveguide Amplifiers," *2009 Conference on Lasers and Electro-Optics and Quantum Electronics and Laser Science Conference (Cleo/Qels 2009), Vols 1-5,* pp. 319-320, 2009.

[23] Marcatil.Ea, "Slab-coupled waveguides," *Bell System Technical Journal,* vol. 53, pp. 645-674, 1974.

[24] P. W. Juodawlkis, *et al.*, "Packaged 1.5-mu m Quantum-Well SOA With 0.8-W Output Power and 5.5-dB Noise Figure," *IEEE Photonics Technology Letters,* vol. 21, pp. 1208-1210, Sep 2009.

[25] K. L. Hall, *et al.*, "Femtosecond index nonlinearities in InGaAsP optical amplifiers," *Applied Physics Letters,* vol. 62, pp. 1320-1322, 1993.

[26] E. W. Vanstryland, *et al.*, "Energy band-gap dependence of 2-photon absorption," *Optics Letters,* vol. 10, pp. 490-492, 1985.

[27] A. M. Darwish, *et al.*, "Short-pulse wavelength shifting by four wave mixing in passive InGaAsP/InP waveguides," *Applied Physics Letters,* vol. 68, pp. 2038-2040, 1996.

Chapter 4

Ultrafast Nonlinear Optical Processes in Silicon Nanowaveguides

Abstract:

Optical nonlinear processes in high-index contrast waveguide circuits consisting of 106nm x 497nm silicon waveguides with SiO_2 and HSQ cladding layers were studied using a heterodyne pump probe experimental setup. The linear loss of the device was determined to be 6.5dB/cm. The two-photon absorption coefficient and free-carrier absorption effective cross-section were determined to be 0.68cm/GW, and 1.9×10^{-17} cm^2, respectively. The plasma dispersion effects, Kerr coefficient, and free-carrier induced refractive index change were determined to be 0.32×10^{-13} cm^2/W, and -5.5×10^{-21} cm^3. The effects of the proton bombardment on the linear loss and the carrier lifetime of the devices were also studied. Carrier lifetime reduction to 33ps with a linear loss of only

14.8dB/cm was achieved using a proton bombardment level of $10^{15}/cm^2$.

4.1. Introduction

Silicon-based optical devices have received a great deal of attention in recent years in both telecomm and electronics industries[1-12]. Nonlinear optical properties of silicon provide both advantages and disadvantages in the design and implementation of such optical devices. They have been utilized in the design of modulators, receivers, and filters to achieve optical communication systems with bit rates in the order of 1Tbits/sec[3]. At a component level, high-sensitivity sensing[13], optical switches[14-16], and broadband electro-optic modulators[17-21] have been demonstrated. Although similar performance can be achieved using III-V devices, silicon optical devices can be produced efficiently, taking advantage of the mature silicon technology that has been extensively developed and perfected over the last century to permit low-cost, large-volume production. This leads to optical devices compatible with the CMOS technology for on-chip integration. The high bandwidths and the high speeds of optical communication systems allow for on-board communication systems at speeds greatly surpassing the electronic alternative[22].

To realize on-board all-optical processing, it's necessary to design and implement both passive and active optical components. Some of the inherent properties of silicon that facilitate the design and implementation of such components are the ultrafast and slow nonlinear optical properties of silicon that can be utilized in the design of optical switches[14-16], wavelength converters[23-25], and analog-to-digital converters[26-28]. In addition, as this technology is based on silicon-on-insulator (SOI) structures, a very high index contrast can be achieved

between Si (n=3.45) on SiO_2 (n=1.45). This high index contrast makes possible highly-confined optical modes in the 1.5μm wavelength range below the bandgap of silicon. Efficient, low-loss transmission of optical modes in waveguides with submicron features makes these devices suitable for the integration of optics and electronics on the same chip[29-33]. The high confinement factor also results in containment of the optical signal inside the silicon section of the device and maximizes the nonlinear optical effects which are solely dependent on the peak intensity of the signal. In addition, the high index contrast achieved with this technology allows for on-chip features such as small-radius ring resonators, and tight, low-loss bends that are not easily achieved using other technologies[30]. Finally, because of a century of continuous research and development driven by the demand for faster processing and communication networks, 10nm feature sizes can be efficiently and easily implemented at low cost using the CMOS technology[34]. Such small feature sizes have been utilized to make slow-light photonic crystals[35] that increase the nonlinear interaction length and enhance the nonlinear effects.

While the nonlinear optical processes are often highly desirable, other inherent properties of silicon make the implementation of silicon-based optical active and passive devices challenging. One of these properties is the indirect bandgap of silicon which makes the realization of an efficient silicon-based laser a great challenge. Another property of silicon is the centrosymmetric property of its crystal. Because of this property of silicon, the design of silicon-based electrooptic modulators is challenging since it makes a long interaction length necessary. Finally, the recovery times in silicon devices vary from several hundreds of picoseconds to several microseconds depending on the structure and the type of silicon crystal[36, 37]. This imposes another challenge in implementation of silicon-based devices in fast optical communication systems since accumulating carriers can produce loss and phase patterning

effects. Nevertheless, many of these challenges have been overcome, and silicon-based lasers [38, 39] and devices with fast recovery times[40, 41] have been demonstrated.

Silicon-based devices that are of particular importance are those that employ the high-index contrast (HIC) structure. Several different types of devices have been designed and demonstrated using HIC[30, 31, 33]. Because of this versatility and variety of designs, HIC structures have received a great deal of attention in both the computer and telecom industries. Since nonlinear optical properties of silicon and the recovery time of these structures play an important part in the performance of devices employing this technology, the rest of this chapter describes the study of these properties.

In the next sections, some of the background of nonlinear optical processes and their application in the design of optical devices is presented. In Section 4.3, the description of the device used, including fabrication process, geometry and mode profile in the waveguides is provided. To study the nonlinear optical processes in these waveguides, a heterodyne pump-probe experiment was implemented. It is described in this Section 4.4. Pump-probe results to extract the nonlinear optical parameters as well as the effect of proton bombardment on the carrier recovery times in the waveguide are discussed. In addition, in this section, an accurate method for determining the coupling loss between the waveguides and the lens fiber is described. Furthermore, the effects of proton bombardment on the carrier recovery and the linear loss of the waveguides are studied and the results are presented in Section 4.6.3.

4.2. Background

4.2.1. Linear and nonlinear optical processes

The complex refractive index of a device can be described by[42]

$$n = n_R + in_I = n_0 + n_2 I + \xi f_\phi(N) - i\frac{\lambda}{4\pi}\left(\alpha_{lin} + \beta I + \sigma f_\alpha(N)\right), \tag{4.1}$$

where n_0 is the refractive index of the device, n_2 is the Kerr coefficient, λ is the optical wavelength, α_{lin} is the linear optical loss, β is the two photon absorption coefficient, $\xi f_\phi(N)$ is the induced phase and $\sigma f_\alpha(N)$ is the loss incurred due to the interaction of the optical field with the TPA-generated free-carriers of density (N), and I is the intensity of the optical field. The imaginary part of the complex refractive-index

$$n_I = \frac{\lambda}{4\pi}\left(\alpha_{lin} + \beta I + \sigma f_\alpha(N)\right) \tag{4.2}$$

demonstrates the loss mechanisms incurred by an optical field. These losses can be divided into two categories, linear and nonlinear. Linear loss, α_{lin} is due to the impurity of the constituent elements and the surface roughness of the waveguides, both of which are dependent on the fabrication process. The linear loss is relatively constant over the length of the device and scales linearly with the length. In addition, linear losses are independent of the optical power inside the waveguide.

Nonlinear optical losses can be further divided into two processes, two-photon absorption (TPA) and free-carrier absorption (FCA). To explain these two processes, we refer to the band diagram of silicon crystal as shown in Figure 4-1. As demonstrated, the energy gap of silicon at k=0 is 3.4eV, while the lowest energy difference between the conduction and valence band is

1.12eV. However, for an electron to be excited from the valence band to the conduction band, a photon with at least 1.12eV of energy, or two photons with the sum of energy greater than or equal to 1.12eV, and a phonon are needed. The latter process is called two-photon absorption. The fact that silicon is an indirect bandgap material, and that both a photon and a phonon are needed for an optically induced transition, greatly limits silicon's use as a light emitter[43, 44]. The free-carriers that are excited to the conduction band as a result of either single photon or two-photon absorption can further absorb photons and be excited to higher energy states. This absorption process is named free-carrier absorption (FCA) and its magnitude is proportional to the number of free-carriers. Both TPA and FCA contribute to optical losses incurred in silicon devices at 1.5μm wavelengths, and their magnitude is a function of the optical intensity.

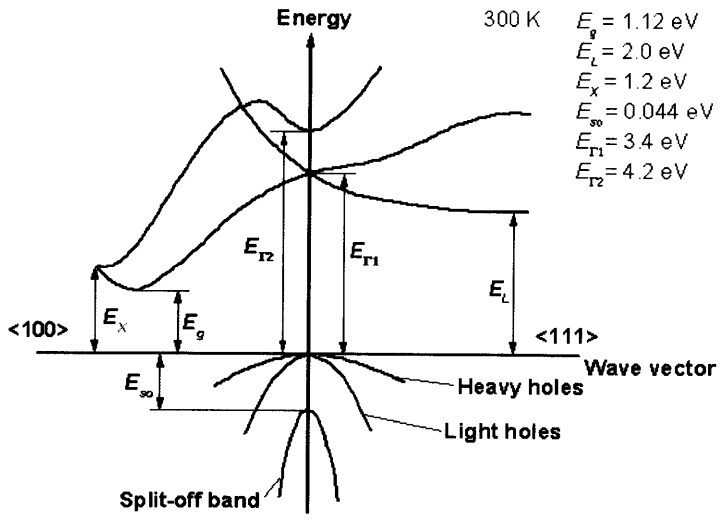

Figure 4-1 – Band diagram of silicon crystal. The indirect bandgap of silicon is 1.12eV [45].

Silicon-based devices have received attention for telecom applications in which the photon energy is in the order of 0.8eV and silicon devices are practically transparent for very low optical power transmission. In fact, due to the indirect bandgap of silicon, its TPA is much

smaller than that of III-V based devices. However, with the increasing demand for higher bit rate communication systems, the duration of optical pulses carrying data is getting shorter. To maintain the same pulse energy and the same BER, shorter pulses must have higher peak powers. As the TPA is a function of the peak intensity, the shorter pulses combined with the smaller waveguides result in peak intensities in the order of several MW/cm^2 and to significant losses and pulse broadening.

Although the TPA process results in optical losses in transmission of signals over long distances and at high optical intensities, its presence can be exploited in the design of square-law detectors and cross-absorption modulators. Square-law detectors can be utilized in optical autocorrelators for measurement of ultrashort pulses. In contrast to using a nonlinear crystal in an autocorrelator, a square law detector is independent of the phase-matching condition and the incident angle or polarization of the optical pulse. In addition, the instantaneous response of TPA can also be utilized in ultrafast cross-absorption modulation in high speed optical switches and wavelength converters[24]. Another application of TPA is in pulse compression taking advantage of the higher loss at the trailing edge of the pulse compared to that at the leading edge[46].

Measurement techniques employed to characterize the magnitude of the TPA coefficient consist of Z-scan technique[47], picosecond pump probe[41], and fitting a model to the transmission response[48, 49]. The TPA coefficients measured using these techniques vary between 0.44 to 0.9 cm/GW in the 1400-1600nm wavelength range. The large range of values emphasizes the necessity to characterize the TPA coefficient more carefully.

In addition to the imaginary part, the real part of the complex refractive index plays an important part in the design of optical devices. The real part of the refractive index indicates the

amount of phase shift that an optical pulse incurs as it propagates through a silicon layer. This phase shift is exploited in the design of optical switches[15, 16], Mach-Zehnder interferometers[50], super-continuum generation[51], and all-optical wavelength converters[23]. The phase-shift component, similar to the loss mechanism, consists of one constant term and two intensity dependent terms:

$$n_R = n_0 + n_2 I + \xi f_\phi(N). \tag{4.3}$$

The first, denoted by n_0, is the refractive index of the material and is the property of the material comprising the waveguide. The second term is a function of the optical field intensity and is characterized by the Kerr coefficient, n_2. Finally, the third component results in the refractive index change as a function of the density of free-carriers (N) generated by the TPA process.

Measurement techniques employed to extract the Kerr coefficient include, Z-scan technique[47, 52, 53], use of SPM[48, 54, 55], the four-wave mixing (FWM) in silicon waveguide[56, 57]. The extracted values of the Kerr coefficient range from $2.8\text{x}10^{-14}$ cm^2/W to $14.5\text{x}10^{-14}$ cm^2/W. Similar to TPA, the published n_2 coefficient values have a large variation. Table 4-1 and Table 4-2 provide a list of previously published TPA and optical Kerr coefficients measured using the above techniques. In this chapter, the direct measurements of all of the nonlinear optical parameters with high sensitivity are presented.

Table 4-1 – Two-photon absorption published data including references and measurement techniques[58].

TPA coefficient (cm/GW)	Wavelength (nm)	Measurement technique	Reference
0.44	1560	1/transmission fit	[38]
0.45	1536	1/transmission fit	[55]
0.5	1455	Transmission fit	[59]
0.6	1550	Transmission fit	[48]
0.67	1547	1/transmission fit	[60]
0.7	1550	Picoseconds pump-probe	[41]
0.79	1540	z-scan	[47]
0.9	1530	1/transmission fit	[61]

Table 4-2 – Optical Kerr-coefficient published data including references and measurement techniques[58].

Optical Kerr coefficient (cm^2/W)	Wavelength (nm)	Measurement technique	Reference
2.8	1500	z-scan	[53]
3.7	1559	SPM	[54]
4.5	1540	z-scan	[47]
4.5	1550	FWM	[57]
5	1500	SPM	[62]
6	1536	SPM	[55]
6	1550	z-scan	[52]
6.5	1550	Phase model	[41]
7	1530	Spectral transmission	[61]
9	1547	FWM	[56]
14.5	1550	SPM	[48]

Direct measurement of the parameters in Equation (4.1) reduces the uncertainty. For this purpose, a heterodyne pump probe experiment is conducted. This measurement technique provides both magnitude and phase information facilitating accurate characterization of all nonlinear terms with the same measurement. Specifically, the heterodyne pump-probe technique has the dynamic range and sensitivity to simultaneously extract the instantaneous response and the FCA loss and phase change as a function of the carrier density. This measurement technique involves mixing a reference signal with the probe signal to separate the probe from the pump. The mixing product of the reference and the probe signals results in a beat frequency whose amplitude and phase are modulated as a function of both the pump intensity and the delay between the pump and probe signals. A detailed description of this technique is given in Section 4.4.

4.2.2. Ion implantation and recovery times

Generation of optical carriers as a result of TPA is an instantaneous process, while the carrier lifetime in silicon waveguides can be in the range of tens of nanoseconds to subnanoseconds depending on the waveguide structure. The structure determines the diffusion time of the carriers away from the optically confined area. In applications where the speed of the optical device plays an important part, such as in high speed telecom or on-chip interconnects, it is desirable to engineer devices with short carrier lifetime. This can be achieved by reverse-biasing a p-i-n structure across a silicon waveguide[41], porous[63] or poly silicon[64], or by ion-implantation [40, 65, 66].

The reduction of carrier lifetime by reverse-biasing the waveguide structure adds complexity to the system and its efficiency deteriorates for high-intensity optical pulses. Porous

and poly silicon are other options but engineering carrier lifetimes using this method is a complex task. Another method is to introduce defects in the waveguide structures by ion-implantation of different types of ions such as hydrogen, helium, oxygen, or even silicon itself. The operation of this method is based on the principle that a charged particle traveling through matter, releases some of its energy along its path. The loss of energy is due to collision with other atoms and interaction with the electrons in the crystal atoms. As the charged particle loses its energy, the interaction effective cross section increases and at a specified range, the proton comes to a stop. Just before the charged particle comes to a stop, it releases most of its energy and creates the most defects. This location is called the Bragg peak. The penetration depth of the particles is dependent on the energy of the charged particles and the material density. The amount of ions implanted in the structure is called the dose, and it is determined by the number of atoms per area.

The defects introduced by this process result in the creation of midgap states in the material band structure. These midgap states facilitate the non-radiative recombination of the free-carriers from the conduction band with holes in the valence band. Therefore, the carrier lifetime can be reduced as a function of the proton-bombardment dose. However, the introduction of these defects in the crystal structure results in higher propagation loss along the device. So, a trade-off must be made between the linear loss and the carrier-lifetime as will be demonstrated in Section 4.6.3. In the following section, a description of the structures that are going to be studied in the following sections is given.

4.3. Device structure

Photonic devices employing high index contrast designs, such as the device shown in Figure 4-2, result in strong confinement of light with moderately low propagation loss. Strong mode confinement facilitates the implementation of bends of small radius in the order of a few microns with very small loss. This features results in more compact filter and coupler designs. The silicon waveguides for this experiment were fabricated using scanning electron-beam lithography (SEBL) as described in [29, 30, 32]. Several different structures, such as ring-resonators, waveguides of different lengths were designed and employed on a single chip. These waveguides were fabricated on a silicon substrate consisting of a 3μm SiO_2 (n=1.45) undercladding and 1μm HSQ overcladding (n=1.37) layers. The waveguides are 106nm in height and 498nm in width, made of silicon (n=3.45). A 100nm thick layer of SiO_2 was sputtered on the top cladding layer. The structure of the waveguide as well as the SEM of the cross section of the chip are shown in Figure 4-2.

(a) (b)

Figure 4-2 – a) Silicon waveguide structure grown on silicon substrate with SiO2 and HSQ cladding layers[67]. b) SEM of the cross section of the chip showing the waveguide and the cladding layers[68].

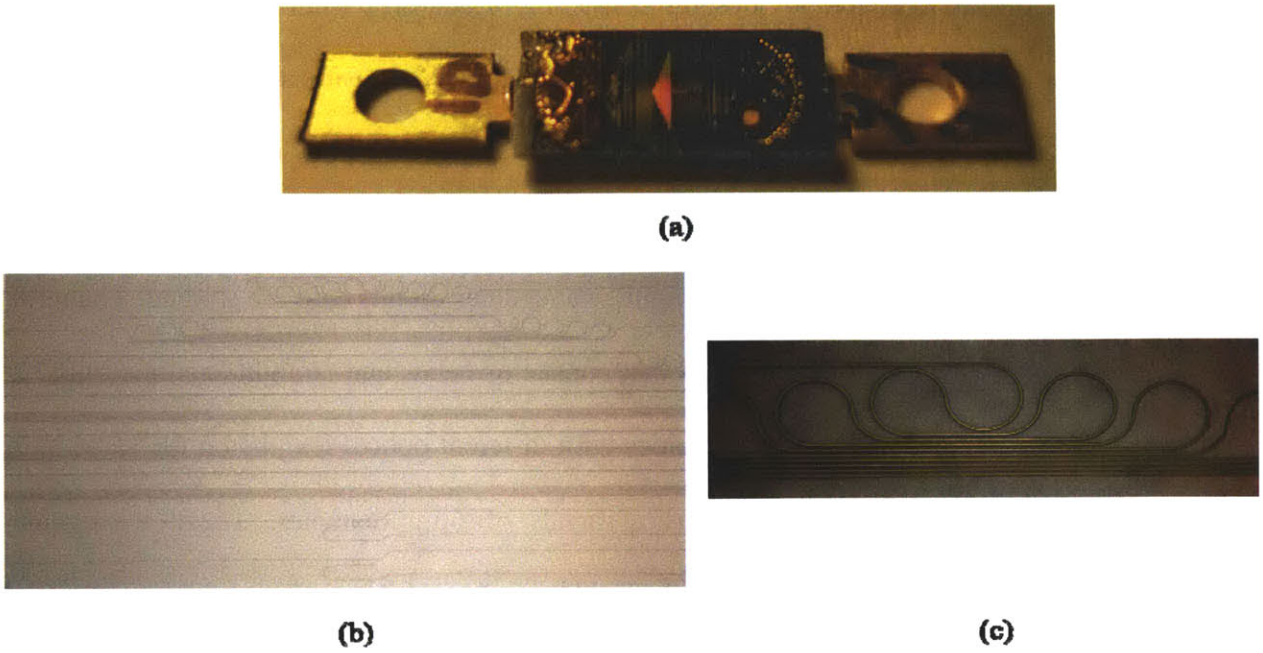

Figure 4-3 – (a) The physical chip on a mount. The metallic section on the top and the bottom of the chip can be bonded for temperature tuning of filters, (b) The top part of the figure shows the paper-clip waveguides of different lengths, while the bottom part of the figure shows the ring-resonators, (c) paper clips and bends implemented using HIC waveguides. The diameter of the bends are 6μm.

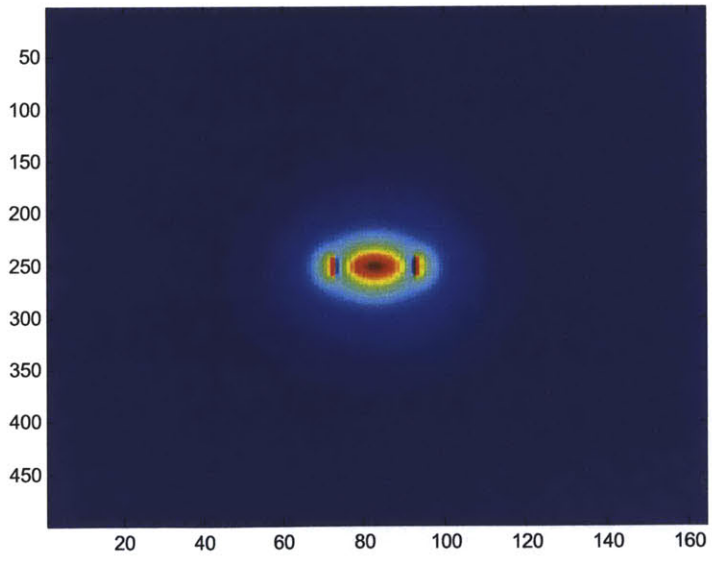

Figure 4-4 – Mode profile of the 106x497nm silicon waveguide with HSQ overcladding and SiO_2 under cladding (courtesy of Anatol Khilo).

One of the HIC chips that will be studied in this thesis is shown in Figure 4-3. This chip contains several different waveguide designs consisting of add-drop multiplexers, tunable ring-resonator filters, and different lengths of straight waveguides as demonstrated in Figure 4-3b where the central part of the chip is magnified under microscope. To study the ultrafast nonlinear optical processes in silicon and to determine the effect of proton bombardment on the recovery time and linear loss of HIC devices, the "straight" waveguides on this chip are studied. The term "straight" refers to waveguides on the chip that consist of bends and straight sections only. As shown in Figure 4-3c, to implement waveguides with different optical lengths on the same chip, paper-clip structures were implemented using bends of 6μm diameter. These waveguides facilitate the characterization of optical coupling and linear loss in the device.

Using finite-difference time-domain (FDTD) simulation, the optical mode in these waveguides was simulated. The mode profile of a 106nm x 497nm optical waveguide using the structure as described above is shown in Figure 4-4. The results of this simulation also show that these waveguides can support only one polarization. Therefore, in the experiments to follow, the input polarization of the light into these waveguides needed to be carefully adjusted. Furthermore, the mode profile and its overlap with the waveguide structure will need to be reconsidered again in the following section in defining "effective area" for the TPA and FCA analyses.

4.4. Theory

The propagation loss in an optical waveguide is a function of the linear loss, TPA, and FCA losses. The differential equation describing the energy of the pulse as it propagates along the length of the device, z, is given in general by:

$$\frac{dI(z,t)}{dz} = -(\alpha_{NL} + \alpha_{lin}) I(z,t), \tag{4.4}$$

where $I(z,t)$ is the instantaneous pulse intensity in the waveguide, and the losses are divided into linear, α_{lin} and nonlinear α_{NL} processes. The nonlinear loss is modeled by

$$\alpha_{NL}(z,t) = \beta I(z,t) + \sigma \int_{-\infty}^{t} \frac{\beta}{\hbar\omega} I^2(z,t) d\tau', \tag{4.5}$$

where β is the TPA coefficient, σ is the FCA effective cross section, and $\hbar\omega$ is the energy of a photon. The first term in this equation is the loss introduced by TPA which is proportional to the optical intensity. The second term is due to the free-carrier absorption, is a function of the free-carrier density generated by the TPA process, and is determined from the integral.

As determined from the FDTD simulation, the mode is highly confined within the waveguide. The high mode-confinement results in optical mode with many k-vectors, and especially a non-negligible E_z component. Since the TPA process is isotropic, the magnitude of the electric field must be accounted for, and this is incorporated in the calculation of the effective area as outlined in Appendix B. If the differential Equation (4.4) is solved using a plane-wave approximation, the intensity of the optical signal inside the waveguide is defined as the ratio of the optical power to an effective area which accounts for the optical mode profile and its interaction with the nonlinear media. By introducing an effective area for the TPA and FCA processes, the above equation can be written as:

$$\frac{dI(z,t)}{dz} = -\left(\beta \frac{P(z,t)}{A_{TPA}} + \sigma \int_{0}^{t} \frac{\beta}{\hbar\omega} \frac{P(z,\tau')}{A_{TPA}} \frac{P(z,\tau')}{A_{FCA}} d\tau' + \alpha_{lin} \right) I(z,t), \tag{4.6}$$

where two effective areas, A_{TPA} and A_{FCA}, defined as the effective areas of the TPA and FCA are introduced. These effective areas are defined so that the intensities

$$TPA: I(z,t) = \frac{P(z,t)}{A_{TPA}} \tag{4.7}$$

$$FCA: I(z,t) = \frac{P(z,t)}{A_{FCA}}, \tag{4.8}$$

may be defined in terms of a plane-wave mode with the optical power *P(z,t)* propagating in the optical waveguide. The overlap of the pump and probe fields, and the waveguide geometry is incorporated in the calculation of the TPA and FCA effective areas A_{TPA} and A_{FCA}, respectively. The calculations of A_{TPA} and A_{FCA} for highly confined structures are described in Appendix B.

4.5. Heterodyne pump probe

As described in previous chapters, a pump-probe measurement technique can be utilized to extract the ultrafast carrier dynamics of an active or passive device. In this method, a pump pulse leads a weaker pulse, the probe, which experiences the change induced by the pump. At the output, a technique to separate the pump and the probe pulses must be implemented. The separation of the pump and the probe pulses can be accomplished using spatial separation, wavelength separation, or orthogonal polarization of the two signals. In the case of our experiments, where pulses of the same wavelength pass through a single-mode single-polarization waveguide, none of these methods are applicable. The heterodyne method described previously to distinguish between the pump and the probe is used. In the heterodyne pump-probe technique[69] the reference and probe signals are RF frequency shifted from the pump via acousto-optic modulators (AOMs), with slightly different amounts. Then, the probe signal is detected using the RF mixing product of the probe with a reference signal. Therefore, the beat frequency can be designed to be in the RF range for easy detection by conventional electronic

equipment. One of the main advantages of the heterodyne pump probe technique is that it is phase sensitive to allow separate extraction of the loss/gain and the refractive index changes of the device under test and that it works for both degenerate and orthogonally polarized pump and probe signals.

4.5.1. Principles of operation

The schematic diagram of the heterodyne pump-probe experimental setup of this study is shown in Figure 4-5. The optical source in this experiment consists of a two stage optical parametric oscillator generating 180fs pulses at a repetition rate of 80 MHz and a center wavelength of 1.5μm. The input pulses entering the experimental setup are split into two paths. The splitting ratio is determined using a half-wave plate and a polarizing beamsplitter (PBS). The lower power signal passes through an acousto-optic modulator (AOM) modulated at the RF frequency of 35MHz. The resulting pulses are used in this experiment as the probe signal. The higher power signal passes through another variable power splitter, where the higher power signal is the pump signal and while the lower power signal is the reference signal. The pump signal is further passed through a variable attenuator and a variable delay stage. The pump and the probe are then combined on a 50:50 splitter with the same polarization. The delay stage in the pump path varies the temporal spacing between the pump and the probe signals.

The combination of the pump and the probe pulses is coupled into a short piece of fiber attached to a 10:90 coupler. The 10% port of the fiber coupler is connected to a power meter to monitor the input optical power. Spliced to the 90% port is a lens-tip fiber. This lens-tip fiber is used to couple the combined pump and probe signals into the waveguide. To optimize the coupling between the fiber and the waveguide, a lens-tip fiber with 1.7μm focal-point beam-

diameter was utilized. After traversing the length of the waveguide, pump and probe signals are collected using another 1.7μm lens-tip fiber at the output port. The collected signal is then combined with the reference signal using a fiber-based 50:50 coupler.

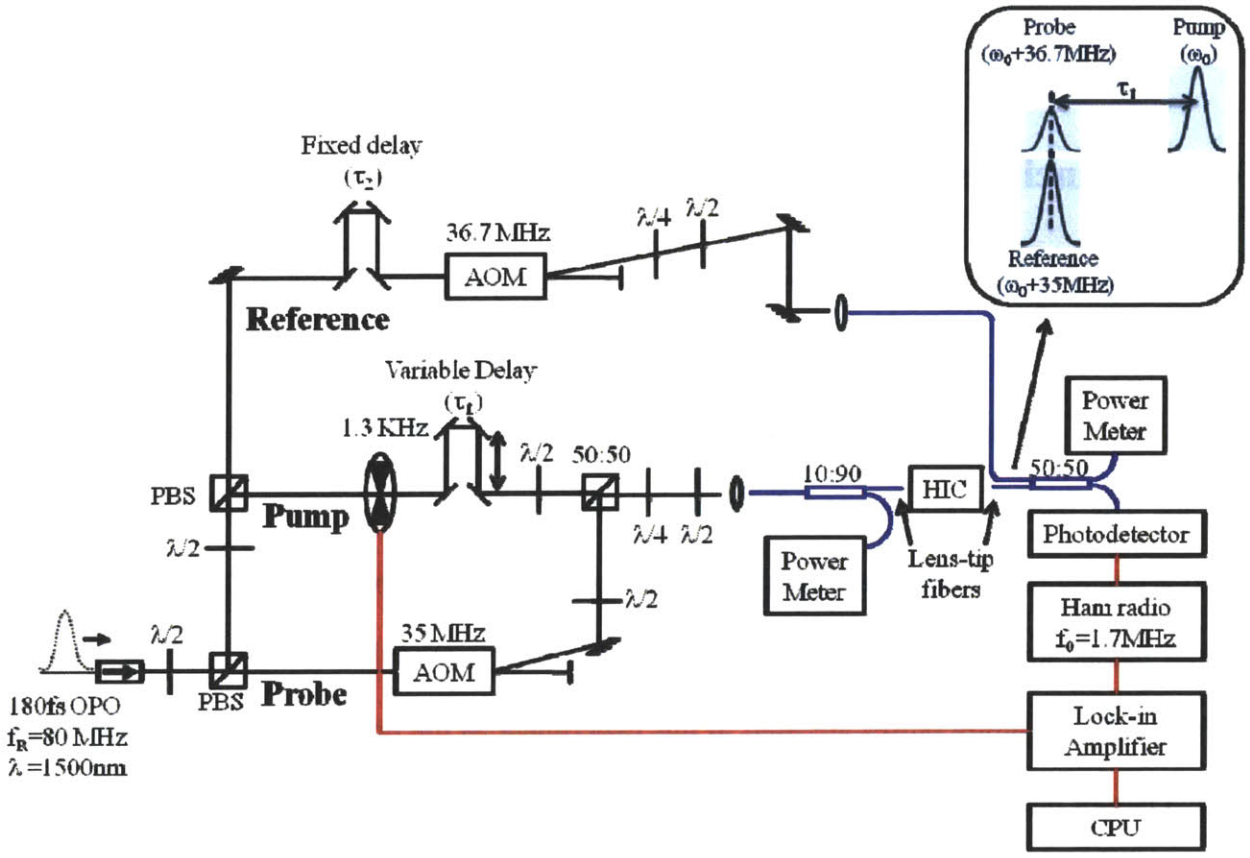

Figure 4-5 – Schematic diagram of a heterodyne pump probe experimental setup. The inset shows the relation between the pump, probe, and reference signals.

The reference signal, prior to being combined with the pump probe signal, is first, passed through a separate AOM modulated at an RF frequency of 36.7MHz. The reference and probe pulses must arrive at the photodetector at the same time with the same polarization. Therefore, a fixed delay is built into the reference path to ensure the temporal overlap of the reference and probe pulses. In addition, a combination of a quarter-wave and a half-wave plate is placed in the reference path just before the reference pulse is coupled into the 50:50 coupler. As a result of the

interference of these two pulses on the detector, a beat frequency equal to the difference between the two RF frequency-shift is generated.

To obtain background-free measurements, the pump signal is amplitude modulated at 1.3 KHz using a mechanical chopper. The interaction of the pump with the waveguide material, induces changes in the magnitude and phase of the probe signal. The magnitude of the variation is a function of the pump power and the delay between the pump and the probe signals. The amplitude and phase variation in the probe signal is translated to the phase and amplitude modulation on the 1.7MHz beat signal with sidebands of 1.3KHz.

$$P_s(t,\tau_1) \propto \left(1+m_{AM}(\tau_1)\cos(\omega_c t)\right)\cos\left(\omega_b t + m_{FM}(\tau_1)\cos(\omega_c t)\right), \tag{4.9}$$

where $P_s(t, \tau_1)$ is the probe power, ω_c is the pump chopping frequency (1.3KHz), ω_b is the beat frequency (1.7MHz), and $m_{AM}(\tau_1)$ and $m_{FM}(\tau_1)$ are modulation depths of the AM and FM modulated signals as a function of the relative delay, τ_1, between pump and probe signals, respectively. The AM modulation depth is a function of the absorption induced by the pump, and the FM modulation depth is proportional to the index change induced. The signal is demodulated using a Ham radio tuned to the carrier frequency of 1.7MHz. The magnitude of the audio output of the radio, in AM or FM mode, is detected using a lock-in amplifier with the reference frequency of 1.3KHz. In the AM mode, the two-photon absorption coefficient and free-carrier induced absorption can be determined, while in the FM mode the Kerr nonlinearity and the free-carrier induced index of refraction change can be characterized.

One of the advantages of utilizing a Ham radio for detection of the AM and FM modulated beat-frequency signal is the narrow-bandwidth of its input filter, resulting in low-noise signal detection. Alternatively, a spectrum analyzer can be used for amplitude detection;

however, the filters in a high frequency Ham radio are as narrow as those of the spectrum analyzer, and the ratio has the additional capability to detect FM signals.

4.5.2. Receiver setting

As described in Equation (4.9), both AM and FM modulations are present on the 1.7MHz carrier frequency. One of the important intricacies in implementation of this method is to minimize the cross-coupling of AM and FM modulations. The cross modulation interference is caused by the conversion of one modulation type to another can occur because of limited bandwidth and nonlinearity of the receiver electronics, and result in erroneous detected signal levels. To minimize this interference, the following parameters in the experiment must be carefully controlled: the RF input power to the radio, RF gain and volume control settings of the radio, and the chopping frequency of the pump signal. The first three parameters must be set to ensure the linear operation of the Ham radio at the beat signal RF level. The chopping frequency must be selected to avoid operating near the band edges of the audio filters of the radio, and away from the vibration noise generated as a result of the movement of the translation stage, and the mechanical chopper itself. The filter bandwidth of the radio was measured to be 2.8KHz. Furthermore, because of the high sensitivity of the heterodyne setup, the vibration due to the motion of the delay stage is translated to a peak frequency at 800Hz. These two parameters set a constraint on the chopping frequency. The next step is to determine the optimum settings for the RF and AF gain of the radio. For this purpose, the experimental setup shown in Figure 4-6 is utilized.

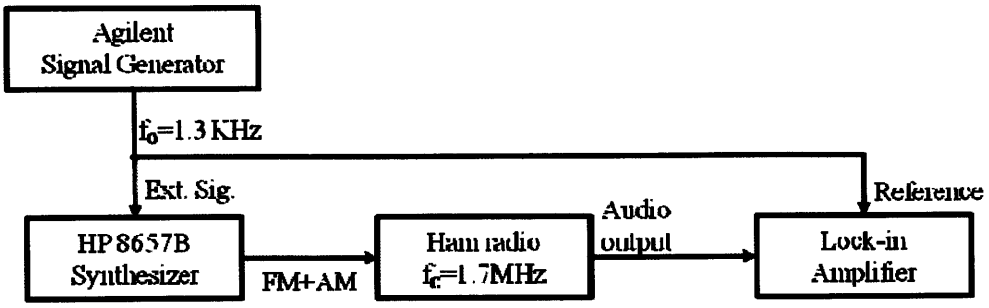

Figure 4-6 – Experimental arrangement to set the radio parameters for the linear operation of the radio receiver

The HP8675B synthesized signal generator is used to generate a signal that is both AM and FM modulated. The carrier frequency of the signal generator is set to 1.7MHz which is the equal to the beat frequency as a result of the mixing product of the pump and probe signals. An Agilent 33250A function generator is used to generate the modulating signal at a frequency f_0. The output of the signal generator is connected the RF input of an IC-R71 Ham radio and is set to -60dBm. The modulation depth of each of the AM and FM modulations can be controlled independently. The RF gain on the radio and the chopping frequency f_0 are varied until the AM/PM or PM/AM conversion for modulation depths of up to 100% are eliminated, while ensuring a linear response for modulation depths between 0 to 100% for the AM and 0 to 300% for the FM modulated signals. Therefore, 1.3KHz chopping frequency was found to be an excellent compromise to reduce noise and minimize modulation interference effects. The receiver adjustments were completed, and the heterodyne pump probe was conducted to study the nonlinear optical properties of the silicon waveguides.

4.6. Results and discussion

In this section, the results of the study of the HIC silicon waveguides as described in Section 4.3 are given. First, a technique to characterize the linear loss and optical coupling loss is discussed. Second, the results of the heterodyne pump probe experiments characterizing the nonlinear optical losses are presented. Finally, the study of the effects of the proton bombardment on the carrier recovery times and linear optical losses are presented.

4.6.1. Characterization of linear and coupling losses

To study the nonlinear optical effects in the silicon waveguides, we need to accurately determine the optical power in the waveguides. Three loss mechanisms consisting of input coupling, output coupling, and linear losses need to be fully characterized. The linear loss is an inherent property of the waveguides and fabrication process and is assumed constant over the length of the waveguide. The optical coupling loss is dependent on several mechanisms some of which are, the Fresnel reflection at the boundary of air and silicon, mode mismatch between the lens-tip fiber and the waveguide, and surface roughness. Optical coupling at the input and output ports are achieved using lens-tip fibers as demonstrated in Figure 4-7. These lensed fibers focus the beam to a 1.7(-0/+3)μm beam diameter at their focal planes. Due to the variation in the beam waist diameter and variations at the input and output interfaces of the chip, the input and output coupling losses cannot be assumed to be equal. Therefore, they need to be accurately characterized. For this purpose, we used the 'cut-back' technique.

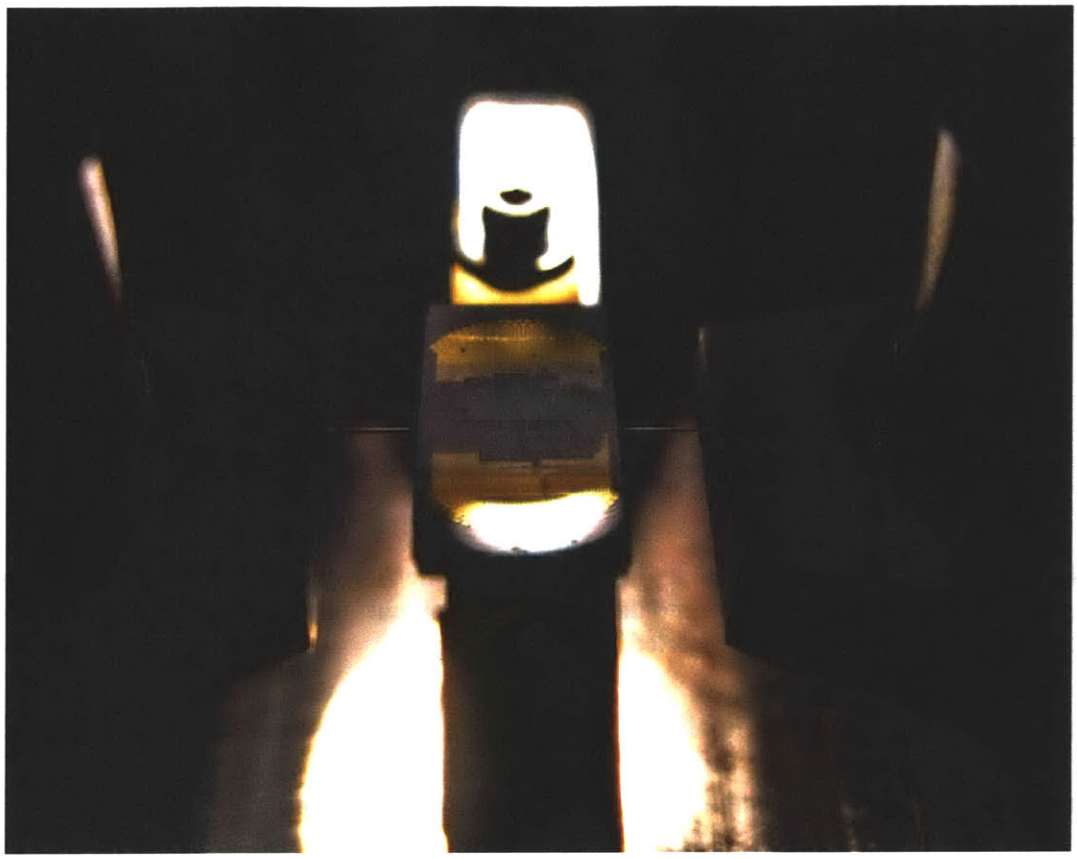

Figure 4-7 – Input and output coupling of light into the silicon waveguides using two lens-tip fibers.

In this method, the light is coupled into waveguides of different lengths and the total loss is plotted as function of the device length. As demonstrated in Figure 4-8, the total loss can be written as:

$$Loss = P_{in} - P_{out} = C_{in} + \left(\alpha_{lin} + \alpha\left(I\right)\right)L + C_{out}, \tag{4.10}$$

$$C_{in}\left(dB\right) = P_{in}\left(dBm\right) - P_{iw}\left(dBm\right) \tag{4.11}$$

$$C_{out}\left(dB\right) = P_{ow}\left(dBm\right) - P_{out}\left(dBm\right) \tag{4.12}$$

where P_{in} and P_{out}, measured in dBm, are the power-levels coupled into the input and output lens-tip fibers, respectively, C_{in} and C_{out} are the coupling losses in dB at the input and output ports, respectively, α_{lin} is the linear loss in dB/cm, while $\alpha(I)$ is the nonlinear loss as a function

of the intensity *(I)* of the beam inside the waveguide, and L is the length of the waveguide in cm. In this figure, the "input" port is defined to be the port where the pump and probe pulses are coupled into the device, while the "output" port is that end of the device where the light is collected and directed to the detector.

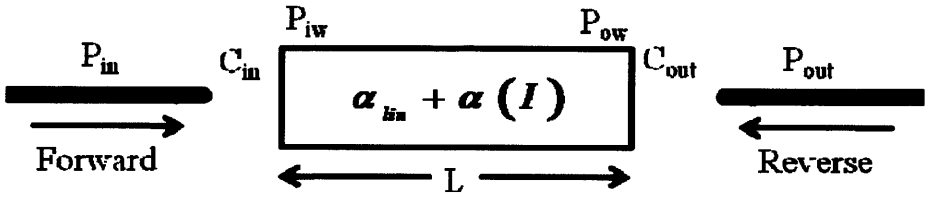

Figure 4-8 – Input, output, and linear losses in a waveguide. The "input" port is defined to be the port that the pump and probe pulses are coupled into the device. The "output" port is defined to be the port that the light is collected from the device and directed to the photodetector.

For intensity levels such that the nonlinear effects become negligible, Equation (4.10) describes a line with slope α_{lin}, and y-intercept point of $C_{total}=C_{in}+C_{out}$. To minimize the nonlinear loss in the above equation, the cut-back method is performed at -30 dBm input power level and the linear response of the device is verified. Since the transverse dimensions of all the waveguides of different lengths on this chip are equal, and they use the save cleaved facet of the chip, we assume, the total input and output coupling losses are the same for all waveguides.

To extract the above parameters, we need at least two waveguides of different lengths. Measurements using input power of -30dBm were conducted on five waveguides with differential length of 6.1mm between any two adjacent waveguides. The length of different waveguide sections were measured using the same setup as in Figure 4-5. The pump signal was blocked, while the probe was coupled into one waveguide after another. The magnitude of the beat frequency between the probe and the reference at 1.7MHz was monitored using a spectrum analyzer. The reference path was adjusted to maximize the magnitude of this beat frequency, and the differential length between two adjacent waveguides was measured to be 6.1mm. In the next

step, the probe and reference signals were blocked while the pump power was coupled into the waveguide. The output power was measured for each of the waveguides, and the result was plotted as a function of the length of the waveguides as shown in Figure 4-9. Using this data, the total coupling loss of 20.8dB and linear loss of 6.5dB/cm were measured.

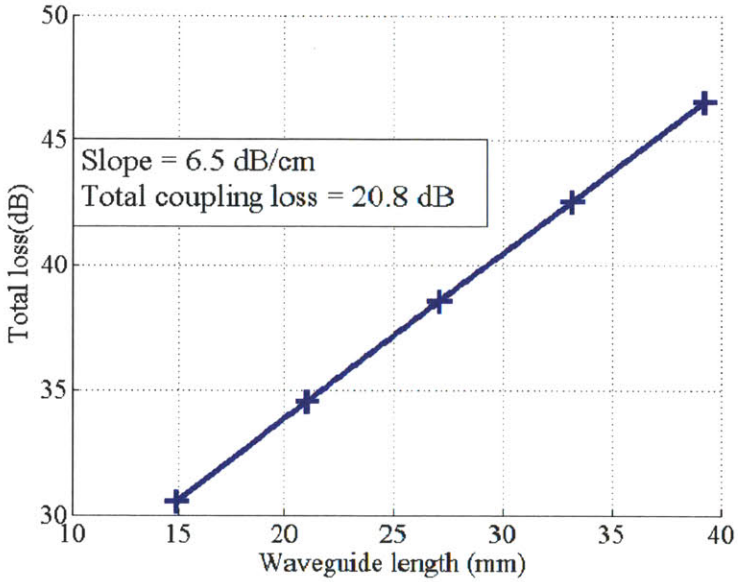

Figure 4-9 – Total loss as a function of waveguide length. Linear loss of 6.5dB/cm and total coupling loss of 20.8dB were measured.

To determine individual coupling losses at the input and output ports of the device, we refer back to Equation(4.10). We can take advantage of the fact that absorption due to nonlinear effects is a function of the intensity of the coupled-light inside the waveguide. Therefore, the total loss deviates from a linear line as a function of the power coupled in the waveguide. To obtain the coupling loss at each port, the device was tested in the two directions "forward" and "reverse" as demonstrated in Figure 4-8. The output power collected by the lens-tip fiber as a function of the input power at the end of the lens-tip fiber was obtained. The higher coupling loss results in lower input power in the waveguide, hence smaller nonlinear optical effects, therefore, it is expected that the port with higher input power roll-off also exhibits larger coupling loss. The

output powers obtained as a function of the input power in each direction are shown in Figure 4-10.

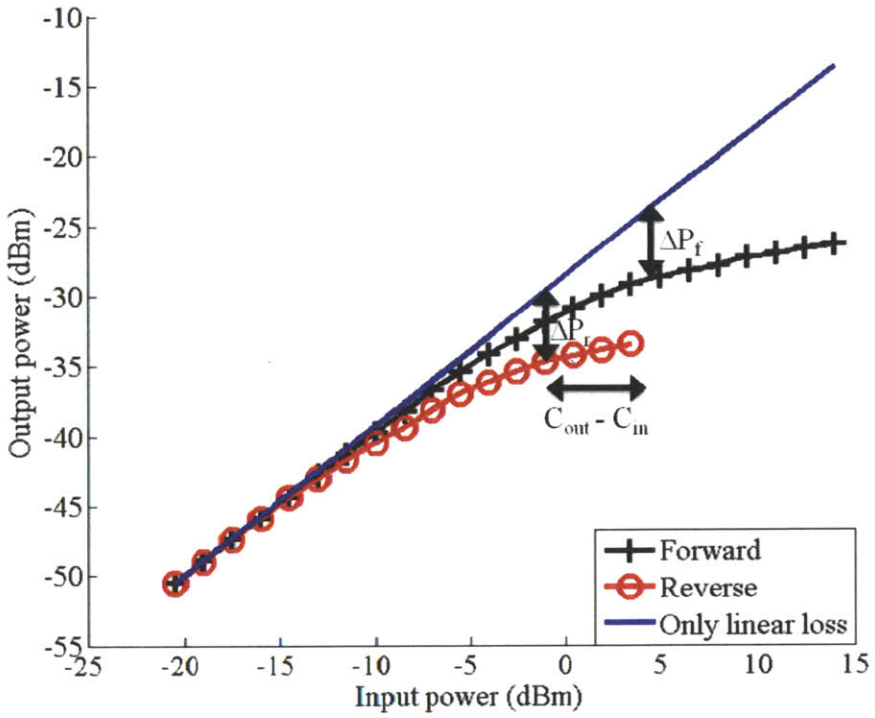

Figure 4-10 – Response of the silicon waveguide when the input and output ports are switched. The linear line is a linear response of the input vs output when there are no nonlinearities present.

The black and red curves are obtained in the "forward" and "reverse" directions, respectively, and since the output power rolls-off at higher input power in the forward direction, clearly, the coupling loss at this port is larger than that of the reverse direction. The blue line is the linear response of the device, hence any variation from this linear line is deemed to be the nonlinear loss and is a function of the light intensity inside the waveguide. Therefore, any two points on the forward and reverse curves that deviate from the linear response by the same amount correspond to having the same input powers inside the waveguide. Therefore, the difference between the input powers corresponding to any two such points is equal to the difference between the coupled powers. This is graphically shown in Figure 4-10. The deviation

of the output power response from the linear response at the input and output ports is calculated and shown in Figure 4-11a. The difference between the input powers corresponding to the same loss level is plotted in Figure 4-11b.

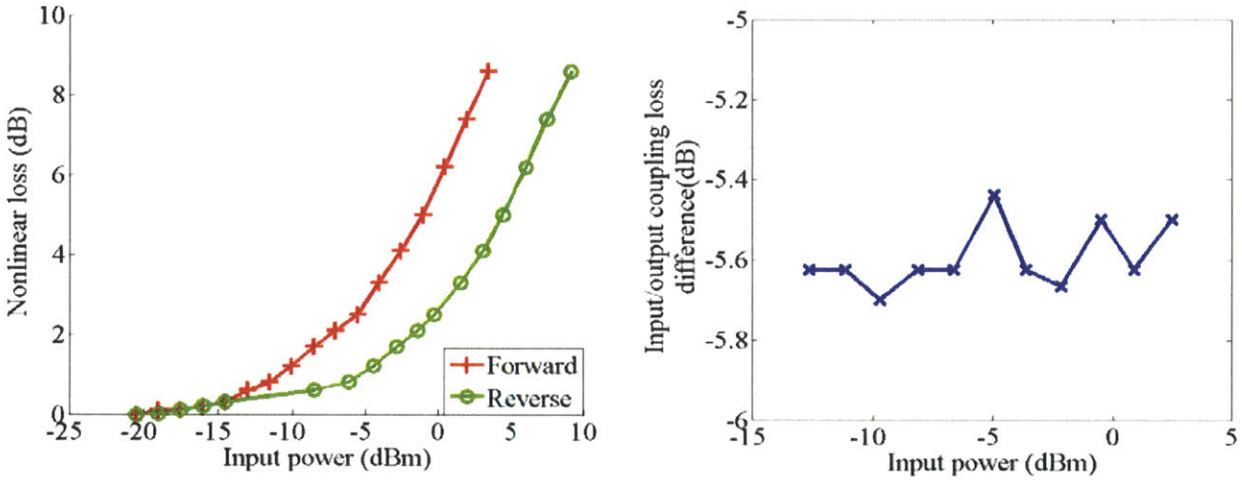

(a) (b)

Figure 4-11 – a) Nonlinear loss in the forward and reverse direction as a function of the input power, b) the difference between the two coupling losses resulting in 5.6dB loss difference.

From this set of measurements, we can see that there is a 5.6dB coupling-loss difference between the input and output coupling losses, C_{in} and C_{out}, while the total coupling loss from Figure 4-9 is 20.8 dB, resulting in C_{in}=13.2dB and C_{out}=7.6dB. We can see that there is a large difference between the input and output coupling losses emphasizing the importance of a careful measurement.

4.6.2. Heterodyne pump probe results

To study the carrier dynamics and nonlinear properties of these devices, the heterodyne pump-probe method which was described in Section 4.4 was utilized. Due to the geometry of the waveguides, only a single polarization is supported, hence a copolarized pump probe experiment

was needed. To study the magnitude of TPA and FCA, the radio was set to detect AM modulation, while to study nonlinear index and plasma dispersion effects, the radio was set to FM. In the following sections, the results of these studies are presented.

4.6.2.1. TPA and FCA magnitudes

Figure 4-12 shows the measured change in the probe signal as a function of the delay of the probe with respect to the pump. When the pump is lagging the probe, there is no modulation induced on the probe, hence no signal is detected. However, when the probe signal coincides with or lags the pump pulses, TPA and FCA induced losses modulate the magnitude of the probe signal at the chopping frequency of the pump. After traversing the length of the device, the probe and the reference signals are mixed on a detector, resulting in the 1.7MHz beat frequency whose amplitude is modulated by the probe signal level at the chopping frequency. This AM modulated signal is detected using the Ham radio which produces a signal level proportional to the modulation depth of the AM signal. This voltage is then compared to that of a known modulation depth to determine how much of the probe signal is absorbed due to the various nonlinear processes. This reference level is determined by blocking the pump signal and chopping the probe at the same modulation frequency as that of the pump, so that 100% AM modulation is induced on the 1.7MHz beat frequency. Since as described in the previous section, we ensured that the radio is operating in a linear regime, the amplitude of the pump probe traces can be normalized using the voltage obtained from chopping the probe signal. The pump probe traces of Figure 4-12 are normalized using this technique.

The ultrafast carrier dynamic of the silicon devices as demonstrated in this figure, consists of two distinct processes, an instantaneous component at time delay (τ_1=0), followed by

a slow recovery time of several hundreds of picoseconds. The amplitude of the instantaneous component is proportional to the intensity of the light inside the waveguide and is caused by two photon absorption, while the magnitude of the slow response is due to absorption of the probe pulse by the free carriers generated in the TPA process. The magnitude of this response is proportional to the square of the intensity. The long recovery time is a function of the quality of the material and the surface roughness of the waveguide structures.

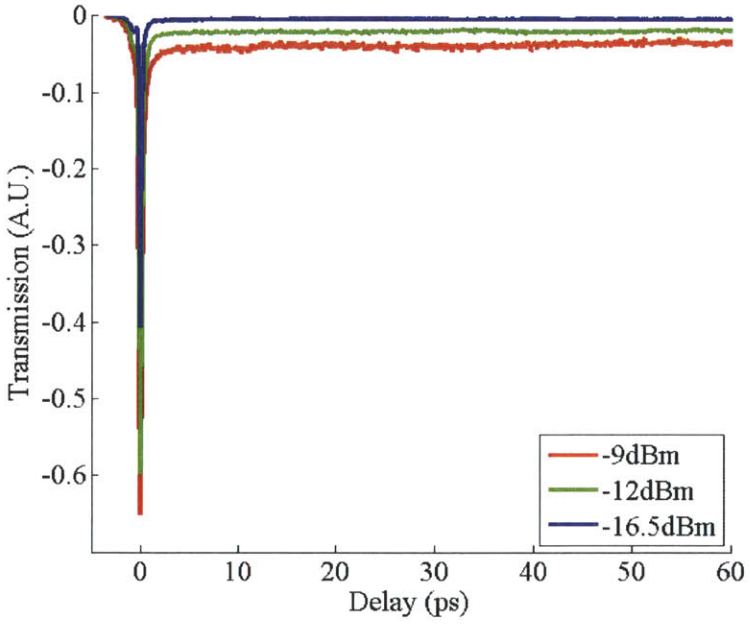

Figure 4-12 – Magnitude response of probe transmission as a function of delay between the pump and probe signals.

Magnitudes of TPA and FCA induced absorptions are plotted as a function of optical signal power inside the waveguide as shown in Figure 4-13. The measured TPA-induced loss is shown in this figure in blue and it consists of a linear section at lower power levels, while at higher input power levels, the magnitude of this loss saturates. The linear section of the curve is dominated by the TPA effect, and as derived in the previous section, is proportional to the

intensity and the TPA coefficient (β). The instantaneous response due to TPA can be described by the following equation

$$\frac{dI_s}{dz} = -\left(\beta I_p + \alpha_{lin}\right) I_s , \tag{4.13}$$

where I_p and I_s are the pump and probe intensities in the waveguide, respectively. Integrating this equation and solving for a change in I_s due to I_p (Appendix C), we have

$$\frac{\Delta I_s}{I_s} = \beta I_p \left(\frac{1 - e^{-\alpha_{lin} L}}{\alpha_{lin}} \right) = \beta I_p L_{eff} , \tag{4.14}$$

where the new variable L_{eff} is the effective length of the device and is given as a function of length (L), and the linear loss (α_{lin}), and I_p is the pump intensity defined as the ratio of the pump power to the TPA effective area. For long waveguides, the effective length reduces to $1/\alpha_{lin}$. The silicon waveguides in this study had a cross-sectional size of 106nm × 497nm and length equal to 14.9mm, $A_{TPA,eff}$, calculated via an overlap integral of E-field and the nonlinear medium, to be 0.1μm^2 and L_{eff} is 0.6cm. The instantaneous response of the device is plotted in Figure 4-13. From the slope of this plot, we extract the TPA coefficient to be 0.68 cm/GW. This compares with the mid range of values previously published as tabulated in Table 4-1. We can see that the TPA induced absorption is linear with optical power up to 20μW and deviates from the line for higher powers. This can be due to the fact that the pump itself is getting increasingly absorbed by TPA at these higher powers.

Each pair of photons absorbed as a result of the TPA process, generates an electron and a hole. Both the electrons in the conduction band and the holes in the valence band in turn absorb photons and result in further optical loss. The total absorption is a function of the number of free-carrier pairs and is described by:

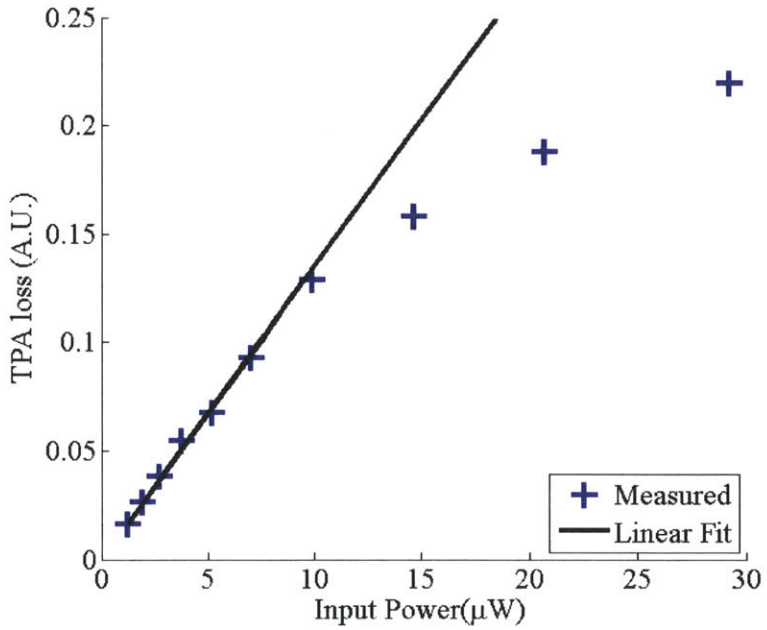

Figure 4-13 – Two photon absorption both measured (+) and with linear fit (line) as a function of the optical power in the waveguide. β=0.68cm/GW is measured.

$$\alpha_{T,FCA} = \int_0^L \sigma N dz = \sigma \int_0^L dz \int_{-\infty}^{t} \frac{\beta I^2(z,t')}{\hbar\omega} dt' = \sigma \frac{N_{total}}{A_{FCA}}, \tag{4.15}$$

where the new variables, $\alpha_{T,FCA}$ is the total loss due to free-carrier absorption, N is the density of carrier pairs per cm^3, and N_{total} is the total number of carrier pairs generated. The effective area in calculating the intensity in this formula is the geometric mean of the TPA and FCA effective cross sections, that is

$$I^2(z,t) = \frac{P(z,t)}{A_{TPA}} \frac{P(z,t)}{A_{FCA}}. \tag{4.16}$$

The total FCA loss is proportional to the total number of carriers generated which is in turn a function of the square of the optical intensity. To calculate the FCA effective cross-section, first, we need to calculate the number of carriers in the waveguide as a function of the input power. Referring back to Equation (4.6), we can see that in the absence of any nonlinearity, the optical

output power of the device would be a linear function of the input power. Therefore, any deviation from a linear response is due to the TPA and FCA processes. To calculate the number of TPA-induced free-carriers the output power of the device as a function of the input power is measured. The direct input versus output power measurement was performed by direct detection of the output power using a power meter, and by chopping the input signal and detecting the modulated output signal at the chopped frequency using a lock-in amplifier. The result is shown in Figure 4-14.

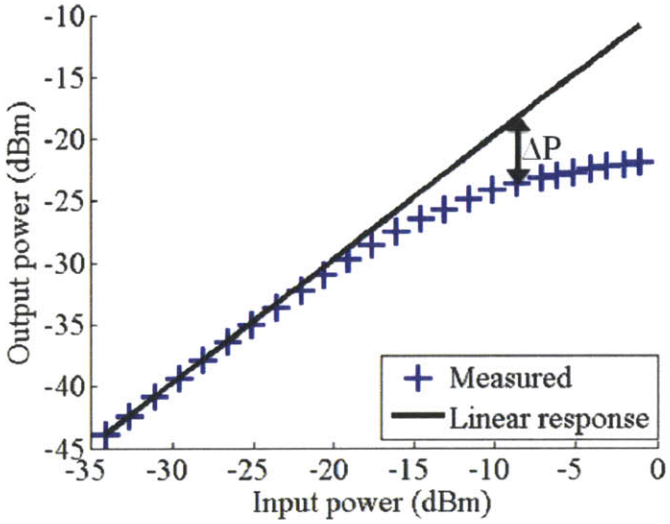

Figure 4-14 – Measured (+) output power as a function of the input power in the silicon waveguide of length 1.49cm. The linear response is also plotted. ΔP demonstrates the loss due to the nonlinearity in the device.

Since, the waveguides are undoped, the densities of the electrons and holes are equal and are given by (Appendix D):

$$N_{Total,e} = N_{Total,h} = \frac{\alpha_{NL}}{2}\frac{E_{in}}{2\hbar\omega}\left(\frac{1-e^{-2\alpha_{lin}L}}{1-e^{-\alpha_{lin}L}}\right), \tag{4.17}$$

where ΔP is the deviation of the output power from a linear response, T is the repetition rate of the laser, $\hbar\omega$ is the energy of the photons, α_{lin} is the linear loss, and L is the physical length of the device. The remaining term α_{NL} is the total nonlinear loss and can be calculated from

$$\alpha_{NL} = 1 - 10^{\left[\left(P_{out,meas}(dBm) - P_{out,lin}(dBm)\right)/10\right]}, \tag{4.18}$$

where $P_{out,lin}$ is the output power of the device without any nonlinear effects, and $P_{out,meas}$ is the actual measured output power. The result of this calculation is shown in Figure 4-15 which demonstrates a quadratic dependence on the input power.

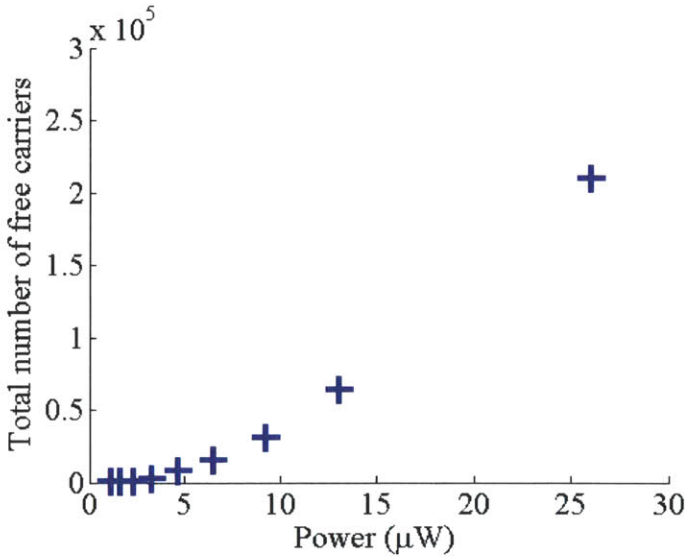

Figure 4-15 – Total number of carriers as a function of the input power of the waveguide.

Free-carriers generated by this process diffuse at 36cm^2/sec[70] and redistribute evenly across the waveguide cross section. Therefore, an effective area for the overlap of the E-field of the propagating mode with this rectangular cross section is calculated and is equal to 0.075μm^2. These carriers are distributed along the length of the device over the FCA effective length, $L_{FCA,eff}$ given by (Appendix C):

$$L_{FCA,eff} = \frac{1 - e^{-2\alpha_{lin}L}}{2\alpha}. \tag{4.19}$$

The total FCA loss is calculated from the heterodyne pump probe experimental results by measuring the transmission loss at time delays larger than 5ps, which is approximately how long it takes for the carriers to diffuse throughout the device. The magnitude of this loss as a function of the input power is calculated from the pump probe traces of Figure 4-12 and shown in Figure 4-16. The fit to the measured data is accomplished using the carrier density calculated using Equation(4.17) and Figure 4-15 with the FCA effective cross section σ=1.9x10^{-17} cm^2. The summary of extracted parameters from this section is given in Table 4-3.

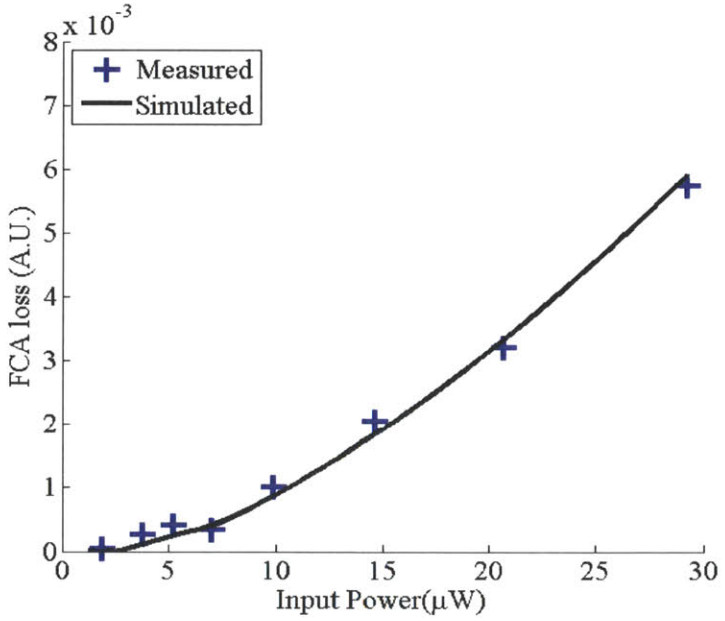

Figure 4-16 – Total loss due to FCA in a silicon waveguide with cross section of 106nm x 497nm and length of 14.9mm. Measured results are shown with (+) markers. The quadratic fit was achieved using the calculated carrier density in the device with FCA effective cross section of 1.9x10^{-17}cm^2.

Table 4-3 – The extracted parameters of the imaginary part of the refractive index

Parameter	Value
TPA coefficient (β)	0.68 (cm/GW)
FCA effective cross section (σ)	1.9×10^{-17} (cm^2)
Linear loss (α_{lin})	1.50 (cm^{-1})
Wavelength (λ)	1.5 (μm)

4.6.2.2. Numerical solution of output response

To further verify the linear and nonlinear parameters extracted thus far, the differential equation describing the pulse evolution along the length of the device was solved numerically using the parameters given in Table 4-3. This differential equation is given by (4.6) and repeated here for convenience

$$\frac{dI(z,t)}{dz} = -\left(\beta \frac{P(z,t)}{A_{TPA}} + \sigma \int_0^t \frac{\beta}{\hbar\omega} \frac{P(z,\tau')}{A_{TPA}} \frac{P(z,\tau')}{A_{FCA}} d\tau' + \alpha_{lin} \right) I(z,t)$$

Using this simulation, the output power of the device as a function of the input power was predicted and compared to the direct input vs output power measurement described in the previous section. The result is shown Figure 4-17. The solid line is the simulation result while the measured data are shown with (+) markers. The results show an excellent agreement between the model and the measured data.

Knowing the nonlinear parameters of the silicon waveguides, we can determine the maximum power that can be transmitted through these waveguides as a function of the pulsewidth before nonlinearity in the waveguides result in significant loss. We study the

limitations imposed by the nonlinear optical properties of the material by determining the 3dB roll off of the output power as a function of the input power. Using the above mode, the responses of the waveguides are simulated for various different pulse widths from 100fs to 40ps at 80MHz repetition rate. The simulation results are shown in Figure 4-18. As demonstrated, there is a significant loss for 100fs pulses at very low powers. This demonstrates the limitations imposed by the TPA and FCA processes in nanowaveguides. The results from this simulation may be utilized to determine the optimum geometry [71] and the maximum power that can be transmitted in a waveguide.

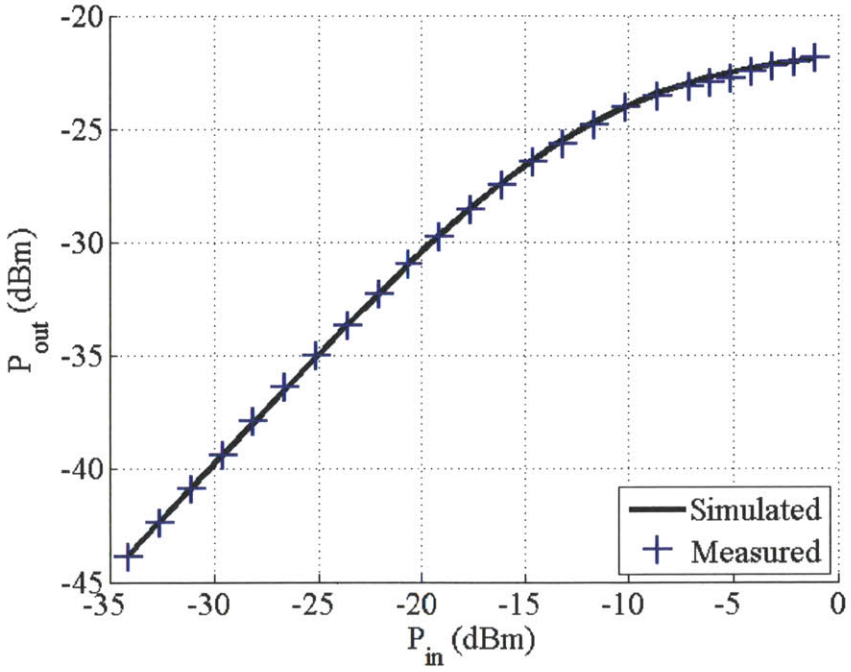

Figure 4-17 – Output power as a function of the input power of the 14.9mm long silicon waveguide. The simulation was performed using β=0.68 cm/GW and σ=1.9x10^{-17} cm^2, α_{lin}=150 cm^{-1}, τ=180fs, λ=1500nm, repetition rate = 80MHz.

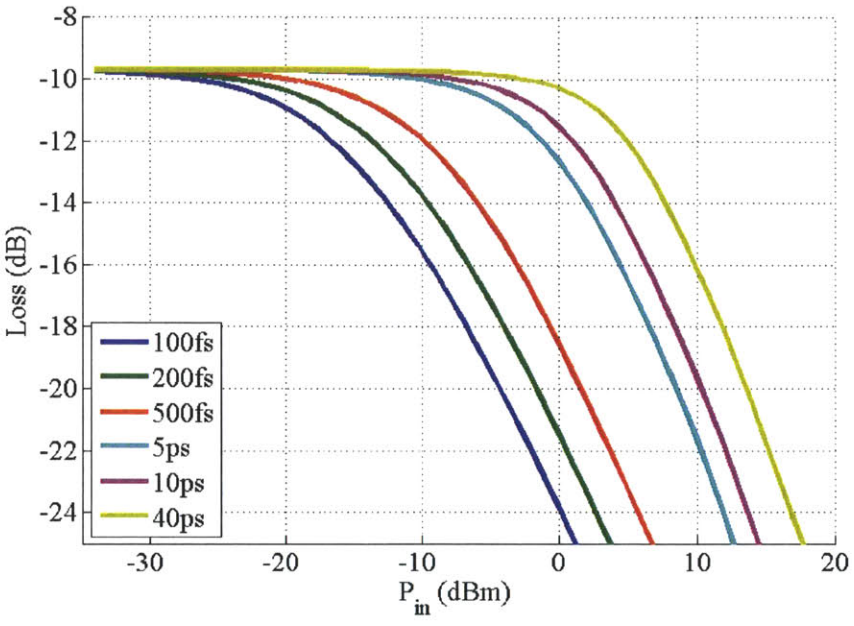

Figure 4-18 – Simulated output power as a function of the input power for input pulsewidths varying between 100fs to 40ps and repetition rate of 80MHz.

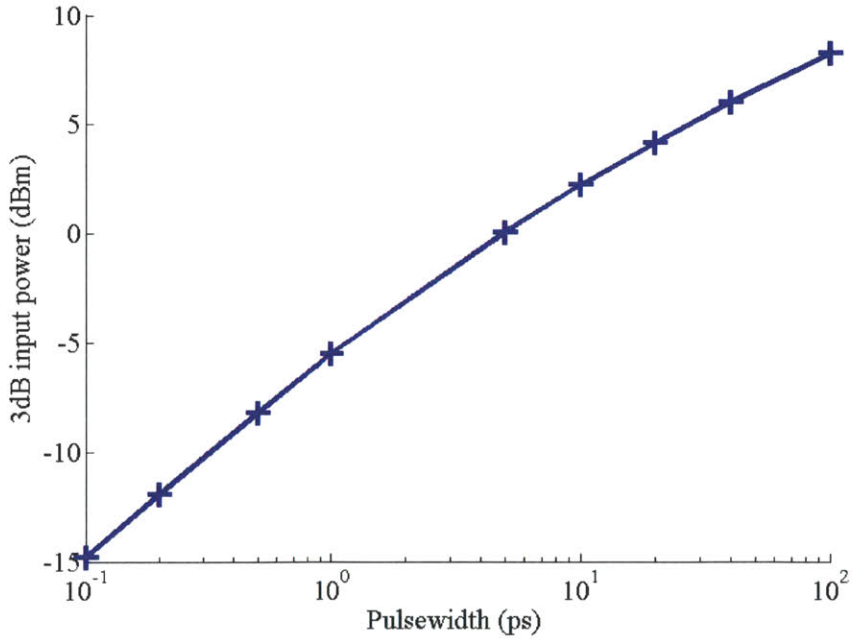

Figure 4-19 – The input power at the 3dB transmission roll-off as a function of the input pulsewidth for an 80MHz repetition rate laser.

Using this simulation technique, we can also calculate the carrier density inside the waveguide as a function of the length of the device. This calculation can be performed by keeping track the amount of light absorbed in the TPA process which is given by:

$$N_{Total,e} = N_{Total,h} = \int_0^L N(z) A_{FCA} dz = \int_0^t \frac{\beta}{\hbar\omega} \frac{P(z,\tau')}{A_{TPA}} \frac{P(z,\tau')}{A_{FCA}} d\tau' \left(/cm^3\right) A_{FCA} dz \,. \qquad (4.20)$$

The result of this calculation as a function of the input optical power is shown in Figure 4-20and compared to the direct measurement of Figure 4-15. We can see the simulated total number of carriers agrees very closely with the measured results. The carrier distribution as a function of the length of the device is shown in Figure 4-21. The carrier concentration follows an exponential decay with the highest concentration at the input of the device. It emphasizes the importance of using an effective length in calculating the total phase shift as a result of refractive index change.

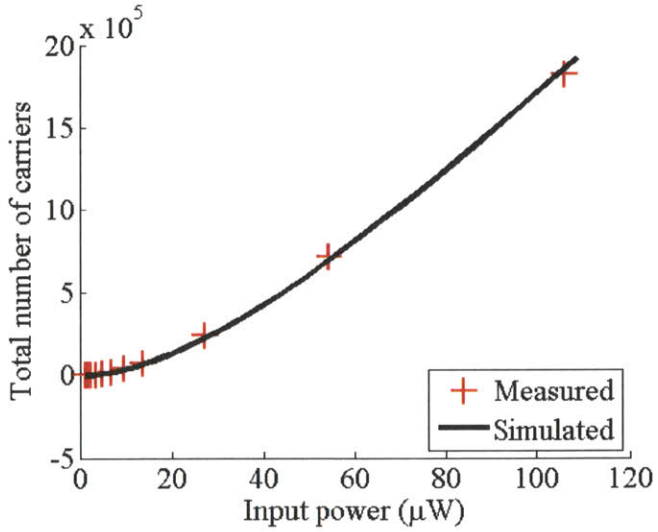

Figure 4-20 – Total number of carriers in the waveguide as a function fo the input power. (+) are measured from the output power vs input power response of the device. The line is the result of the simulation by solving the differential equation describing the pulse propagation along the device.

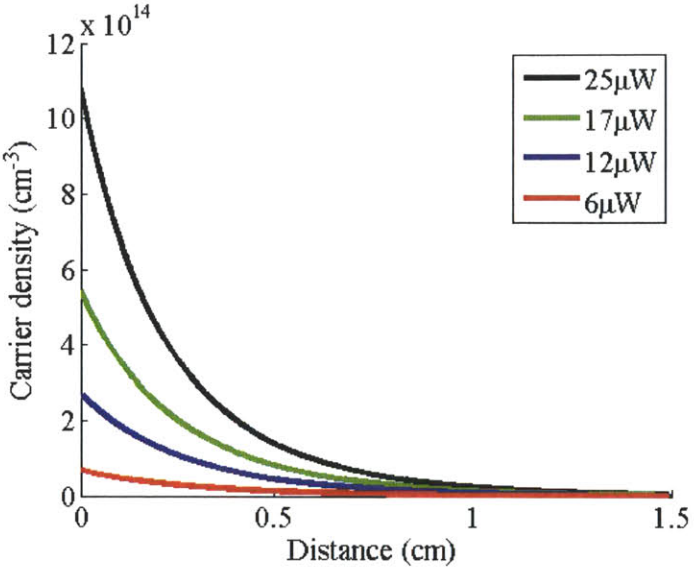

Figure 4-21 – Free-carrier distribution as a function of the length of the device

4.6.2.3. Optical Kerr effect and free-carrier index changes

It is well known that the optical Kerr effect plays an important role in the transmission of short pulses through waveguides since it affects the chirp and the spectrum of the pulses. In addition, the refractive index changes induced by this process can be exploited in all-optical switching and signal processing[14, 16]. When free carriers are generated at the same time by TPA, additional, longer-lived changes in index of refraction are also induced. To study these effects, the heterodyne pump probe technique at 1.5μm was again used here. The optical phase of the probe signal which is launched after the pump, experiences changes proportional to these refractive index changes. Since the pump is amplitude modulated using a chopper, the phase-change in the probe signal is modulated at chopping frequency. The magnitude of the phase change is a function of the number of generated free-carriers, hence a function of the pump power. To detect this optical phase change, the radio in Figure 4-5 is set to detect FM modulations. A major advantage of the FM radio is that it automatically tracks and locks onto the RF carrier and thus,

circumvents the need to interferometrically stabilize the optical phase between probe and reference. The radio output voltage, proportional to the FM modulation depth of the beat frequency is also linearly proportional to the optically induced phase changes of the probe, and is modulated at the chopping frequency. The amplitude and phase of the output signal from the Ham radio are then further detected with a lock-in amplifier.

To determine the FM modulation depth on the probe signal, the output of the lock-in amplifier must be calibrated. The calibration is performed by applying a 100% FM modulated signal to the RF port of the AOM driver in the probe path. The resulting beat frequency between the probe and the reference is passed through the radio which is set for FM detection and the resulting output is measured using the lock-in amplifier. The output of the lock-in is a reference for a 100% FM modulation. The pump probe traces are normalized using this reference level.

Figure 4-22 shows the result of the normalized heterodyne pump probe traces using FM detection. In this figure, the horizontal axis indicates the delay between the pump and probe traces, and the vertical axis is the measured phase change incurred by the probe signal. As demonstrated in this figure, the device response consists of an instantaneous response at time delay of zero which is linearly dependent on the pulse intensity. This instantaneous component is followed by a slow recovery response of several hundreds of picoseconds. The instantaneous response is attributed to the phase response incurred by the probe due to Kerr nonlinearity. The change in sign is due to the opposite signs in the induced refractive index changes for Kerr nonlinearity and for free carriers.

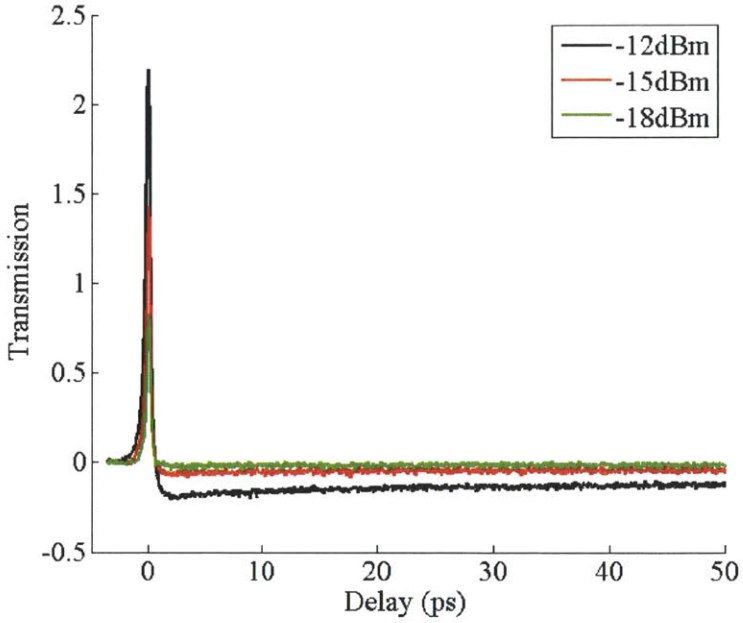

Figure 4-22 – Measured probe phase change as a function of the delay between the pump and probe pulses.

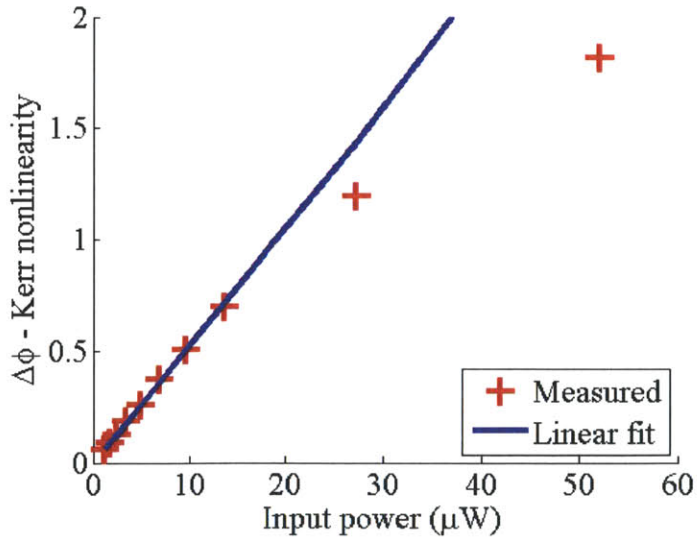

Figure 4-23 – Kerr coefficient induced phase change at $\tau=0$ as a function of the optical power. n_2 is calculated to be 3.2×10^{-14} cm^2/W.

From this measurement, we can determine both the Kerr nonlinearity and refractive index change as a function of carrier density for these HIC silicon waveguides. As with TPA characterization of the previous section, the magnitude of the induced phase change at zero time delay (τ_1=0) as a function of the coupled optical power inside the waveguide. These results are shown in Figure 4-23. The measurement consists of a linear region at powers up to 30μW and the maximum phase change starts to deviate from the linear line at higher powers. The Kerr coefficient can be determined from:

$$\Delta n = \frac{\lambda}{2\pi L_{eff}} \Delta\phi = n_2 I , \tag{4.21}$$

where λ is the wavelength of the optical signal, L_{eff} is the effective length of the device as defined in pervious section, $\Delta\phi$ is the induced phase change, I is the intensity of the optical signal inside the waveguide, and n_2 is the Kerr coefficient. The effective length and effective area are defined as for the TPA measurement. From the slope of this plot, we extracted the Kerr coefficient to be n_2=3.2x10^{-14} cm^2/W. This value is in close agreement with the previously published data using z-scan technique as tabulated in Table 4-2.

In addition to the instantaneous response, we can observe an induced phase change after a 5ps delay which has a long recovery time. This induced phase change, similar to the induced FCA loss, is a function of the number of free carriers generated by the TPA process. Therefore, we can take advantage of the earlier calculations of the number of carriers and determine the index of refraction change as a function of the carrier density.

As discussed in Section 4.6.2.1, the free-carriers are distributed over the cross-section of the waveguide and over the effective length, $L_{FCA,eff}$. Using the total number of carriers, we define the refractive index change as a function of carrier density as:

$$\Delta n = \xi \frac{N_{total}}{A_{FCA}}, \tag{4.22}$$

where Δn is the total change in the refractive index, ξ is a proportionality constant, N_{total} is the total number of carrier pairs generated[72]. The fit as shown in Figure 4-24 was achieved using ξ=-5.5x10^{-21} cm^3. The results obtained in this section are summarized in Table 4-4.

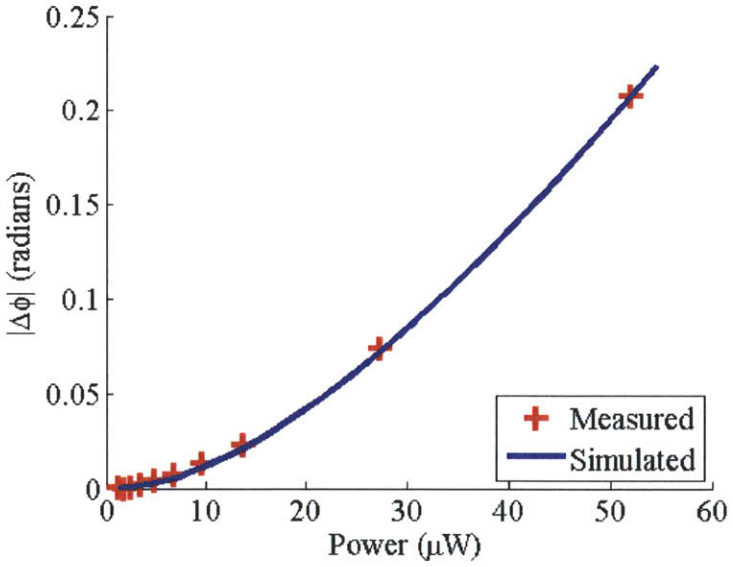

Figure 4-24 – $|\Delta\phi|$ vs power both measured and fitted with ξ= -5.5x10^{-21} cm^3.

Table 4-4 – Kerr coefficient and refractive index change due to free carriers

Parameter	Value
Kerr coefficient (n_2)	3.2x10^{-14} (cm^2/GW)
Refractive index change per free-carrier pair volume(ξ)	-5.5x 10^{-21} (cm^3)
Wavelength (λ)	1.5 (μm)

4.6.3. Carrier recovery time and proton bombardment

In addition to the optical nonlinear processes discussed up to this point, the carrier recovery time in the silicon waveguides will dictate their usefulness in high speed optical systems. In this section, a study of the effects of ion implantation on the carrier recovery time and linear loss of the silicon samples is presented. Proton bombardment of samples results in creation of defects in the crystal structure. These defects create midgap states which speed up the recovery time of the device. It has been shown that with higher dosages of ion implants which results in the desired effect of reducing the recovery times, the defects in the crystal structure result in higher scattering and absorption through the device, hence higher linear loss.

For the purpose of this study, several silicon waveguide chips were ion implanted at dosages varying from 10^{12} to 10^{15} /cm^2. First, it was necessary to determine the energy level of protons that will penetrate different layers of the structure. These layers are illustrated in Figure 4-2. Therefore, for the protons to reach the silicon waveguides they must penetrate through 100nm layer of SiO_2, 1μm of HSQ, and get implanted in the 100nm-thick silicon waveguide. To determine the proper energy levels, the SRIM program was utilized (www.srim.org). SRIM program is based on the Monte-Carlo analysis and simulates the penetration depth of protons of different energy accounting for scattering, energy loss, and non-uniformity of proton energy levels. The result of this simulation is shown in Figure 4-25. The devices were proton-bombarded using three different energy levels of 80, 90, and 100KeV. Three energy levels were used to account for variations in the density of HSQ layer, which is highly dependent on the fabrication process, and to still create the desired distribution of defect states in the silicon waveguides. In this figure, the silicon waveguides start at the depth of 1100nm and extend to 1206nm where the largest number of defect states is created.

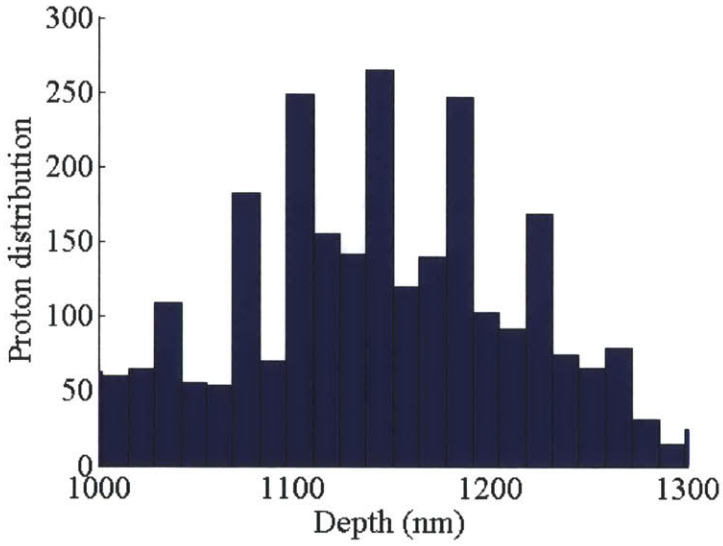

Figure 4-25 – Cumulative distribution of ions utilizing the SRIM simulation of waveguides using a combination of 80, 90, and 100KeV proton energy levels and a dose of $10^{12}/cm^2$ protons (www.srim.org).

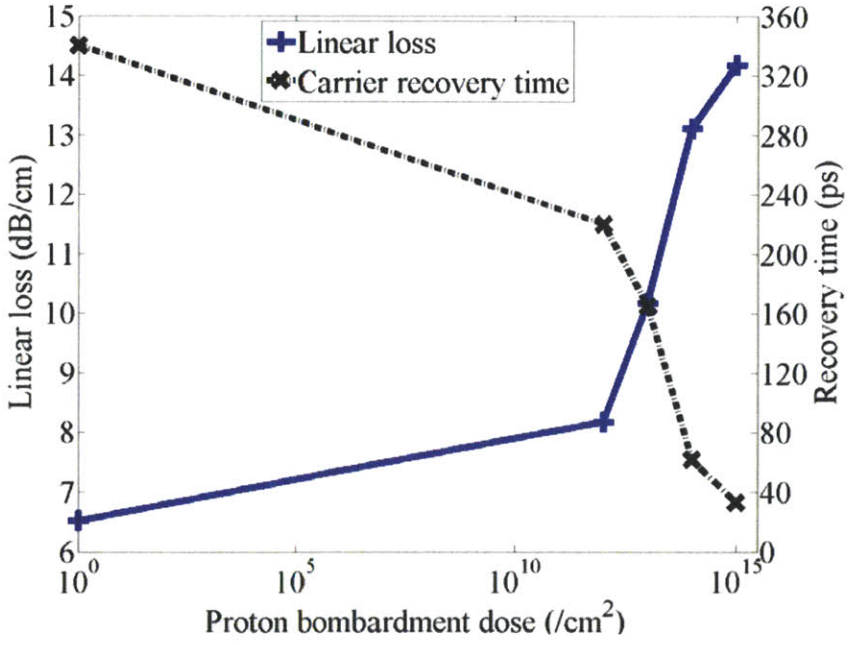

Figure 4-26 – Linear loss and carrier recovery time as a function of the proton bombardment.

After processing the samples, their linear loss and recovery times were measured and are plotted in Figure 4-26. A recovery time as short as 33ps for a linear loss of only 14.8dB/cm was obtained at the highest proton-bombardment level of using $10^{15}/cm^2$. This combination of recovery time reduction and degradation in linear loss seems the best thus far reported for the proton bombardment technique[40].

4.7. Conclusion

In this chapter, the ultrafast nonlinear optical properties of high-index contrast silicon waveguides of 106nm×497nm cross section were studied. Input and output optical coupling was accomplished using lens-tip fibers, and a 6 dB difference between the coupling efficiencies at the input and output ports was observed. A heterodyne pump-probe technique was utilized to characterize the magnitude of the TPA and FCA losses as well as the Kerr nonlinearity and the refractive index change as a function of the carrier density. The high sensitivity of the heterodyne technique has allowed for this characterization using very small carrier densities with great accuracy. The parameters extracted were applied to the model predicting the output power response of the waveguides as a function of the input power. This model was utilized to predict the limitations imposed by the nonlinearity on the transmission of pulsewidths of different duration. As the carrier recovery of silicon can be in the order of several hundreds of picoseconds to nanoseconds, the devices were proton bombarded with different doses. Carrier lifetime of 33ps with proton bombardment level of 10^{15} $/cm^2$ with an increase of linear loss to 14.8dB/cm was achieved.

4.8. References

[1] D. Englund, *et al.*, "Ultrafast photonic crystal lasers," *Laser & Photonics Reviews,* vol. 2, pp. 264-274, 2008.

[2] N. Fujioka, *et al.*, "Compact and Low Power Consumption Hybrid Integrated Wavelength Tunable Laser Module Using Silicon Waveguide Resonators," *Journal of Lightwave Technology,* vol. 28, pp. 3115-3120, 2010.

[3] H. Ji, *et al.*, "1.28-Tb/s Demultiplexing of an OTDM DPSK Data Signal Using a Silicon Waveguide," *IEEE Photonics Technology Letters,* vol. 22, pp. 1762-1764, 2010.

[4] G. L. Li, *et al.*, "Ultralow-power silicon photonic interconnect for high-performance computing systems," *Optoelectronic Interconnects and Component Integration Ix,* vol. 7607, 2010.

[5] B. Jalali and S. Fathpour, "Silicon photonics," *Journal of Lightwave Technology,* vol. 24, pp. 4600-4615, 2006.

[6] R. M. De La Rue and Ieee, "Sensitive Silicon and Silica Based Photonics," in *2009 IEEE Leos Annual Meeting Conference Proceedings, Vols 1and 2*, ed, 2009, pp. 63-64.

[7] M. Hochberg and T. Baehr-Jones, "Towards fabless silicon photonics," *Nature Photonics,* vol. 4, pp. 492-494, Aug 2010.

[8] B. Jalali, "Silicon photonics Nonlinear optics in the mid-infrared," *Nature Photonics,* vol. 4, pp. 506-508, Aug 2010.

[9] G. Overton, "Silicon photonics Cascaded microrings convert laser pulses for wireless communication," *Laser Focus World,* vol. 46, pp. 19-+, May 2010.

[10] G. T. Reed, *et al.*, "Silicon Photonics: Optical modulators," in *Quantum Sensing and Nanophotonic Devices Vii.* vol. 7608, M. Razeghi, *et al.*, Eds., ed, 2010.

[11] R. Won and M. Paniccia, "Integrating silicon photonics," *Nature Photonics,* vol. 4, pp. 498-499, Aug 2010.

[12] W. A. Zortman, *et al.*, "Silicon photonics manufacturing," *Optics Express,* vol. 18, pp. 23598-23607, Nov 2010.

[13] J. T. Robinson, *et al.*, "On-chip gas detection in silicon optical microcavities," *Optics Express,* vol. 16, pp. 4296-4301, 2008.

[14] M. Khorasaninejad and S. S. Saini, "All-optical logic gates using nonlinear effects in silicon-on-insulator waveguides," *Applied Optics,* vol. 48, pp. F31-F36, Sep 2009.

[15] J. Y. Lee, *et al.*, "Ultrafast optical switching based on nonlinear polarization rotation in silicon waveguides," *Optics Express,* vol. 18, pp. 11514-11523, May 2010.

[16] A. Martinez, *et al.*, "Ultrafast All-Optical Switching in a Silicon-Nanocrystal-Based Silicon Slot Waveguide at Telecom Wavelengths," *Nano Letters,* vol. 10, pp. 1506-1511, 2010.

[17] F. W. Gan and F. X. Kartner, "High-speed silicon electrooptic modulator design," *IEEE Photonics Technology Letters,* vol. 17, pp. 1007-1009, 2005.

[18] T. Barwicz, *et al.*, "Silicon photonics for compact, energy-efficient interconnects Invited," *Journal of Optical Networking,* vol. 6, pp. 63-73, 2007.

[19] K. Preston, *et al.*, "2.5 Gbps Electro-optic Modulator in Deposited Silicon," *2009 Conference on Lasers and Electro-Optics and Quantum Electronics and Laser Science Conference (Cleo/Qels 2009), Vols 1-5,* pp. 1273-1274, 2009.

[20] S. Manipatruni, *et al.*, "Ultra-low voltage, ultra-small mode volume silicon microring modulator," *Optics Express,* vol. 18, pp. 18235-18242, 2010.

[21] G. T. Reed, *et al.*, "Silicon Photonics: Optical modulators," *Quantum Sensing and Nanophotonic Devices Vii,* vol. 7608, 2010.

[22] A. Andrew, *et al.*, "Demonstration of a High Speed 4-Channel Integrated Silicon Photonics WDM Link with Hybrid Silicon Lasers," 2010, p. PDIWI5.

[23] F. X. Kartner, *et al.*, "Electronic photonic integrated circuits for high speed, high resolution, analog to digital conversion - art. no. 612503," *Silicon Photonics,* vol. 6125, pp. 12503-12503, 2006.

[24] Y.-H. Kuo, *et al.*, "Demonstration of wavelength conversion at 40 Gb/s data rate in silicon waveguides," *Opt. Express,* vol. 14, pp. 11721-11726, 2006.

[25] Q. F. Xu and M. Lipson, "All-optical logic based on silicon micro-ring resonators," *Optics Express,* vol. 15, pp. 924-929, 2007.

[26] P. W. Juodawlkis, *et al.*, "Optically sampled analog-to-digital converters," *Microwave Theory and Techniques, IEEE Transactions on,* vol. 49, pp. 1840-1853, 2001.

[27] G. C. Valley, "Photonic analog-to-digital converters," *Opt. Express,* vol. 15, pp. 1955-1982, 2007.

[28] F. X. Kartner, *et al.*, "Photonic analog-to-digital conversion with electronic-photonic integrated circuits," San Jose, CA, USA, 2008, pp. 689806-15.

[29] T. Barwicz, *et al.*, "Reconfigurable silicon photonic circuits for telecommunication applications - art. no. 6872OZ," *Laser Resonators and Beam Control X,* vol. 6872, pp. OZ872-OZ872, 2008.

[30] M. A. Popovic, *et al.*, "Hitless-reconfigurable and bandwidth-scalable silicon photonic circuits for telecom and interconnect applications," *2008 Conference on Optical Fiber Communication/National Fiber Optic Engineers Conference, Vols 1-8,* pp. 2296-2298, 2008.

[31] J. S. Orcutt, *et al.*, "Photonic integration in a commercial scaled bulk-CMOS process," *Ps: 2009 International Conference on Photonics in Switching,* pp. 170-171, 2009.

[32] C. W. Holzwarth, *et al.*, "Device Architecture and Precision Nanofabrication of Microring-Resonator Filter Banks for Integrated Photonic Systems," *Journal of Nanoscience and Nanotechnology,* vol. 10, pp. 2044-2052, 2010.

[33] A. Khilo, *et al.*, "Efficient planar fiber-to-chip coupler based on two-stage adiabatic evolution," *Optics Express,* vol. 18, pp. 15790-15806, 2010.

[34] G. Tallents, *et al.*, "Optical lithography: Lithography at EUV wavelengths," *Nat Photon,* vol. 4, pp. 809-811, 2010.

[35] T. M. Shih, *et al.*, "Supercollimation in photonic crystals composed of silicon rods," *Applied Physics Letters,* vol. 93, 2008.

[36] A. Liu, *et al.*, "A high-speed silicon optical modulator based on a metal-oxide-semiconductor capacitor," *Nature,* vol. 427, pp. 615-618, 2004.

[37] R. Salem, *et al.*, "High-speed optical sampling using a silicon-chiptemporal magnifier," *Opt. Express,* vol. 17, pp. 4324-4329, 2009.

[38] R. Claps, *et al.*, "Observation of stimulated Raman amplification in silicon waveguides," *Opt. Express,* vol. 11, pp. 1731-1739, 2003.

[39] O. Boyraz and B. Jalali, "Demonstration of directly modulated silicon Raman laser," *Opt. Express,* vol. 13, pp. 796-800, 2005.

[40] P. J. Foster, *et al.*, "Optical attenuation in defect-engineered silicon rib waveguides," *Journal of Applied Physics,* vol. 99, p. 073101, 2006.

[41] A. C. Turner-Foster, *et al.*, "Ultrashort free-carrier lifetime in low-loss silicon nanowaveguides," *Opt. Express,* vol. 18, pp. 3582-3591, 2010.

[42] J. Leuthold, *et al.*, "Nonlinear silicon photonics," *Nature Photonics,* vol. 4, pp. 535-544, 2010.

[43] Y. Huang, *et al.*, "Proposal for loss reduction and output enhancement of silicon Raman laser using bi-directional pumping scheme," *Optics Communications,* vol. 283, pp. 1389-1393, 2010.

[44] H. Rong, *et al.*, "A continuous-wave Raman silicon laser," *Nature,* vol. 433, pp. 725-728, 2005.

[45] *Silicon band diagram.* Available: http://www.ioffe.ru/SVA/NSM/Semicond/Si/Figs/121.gif

[46] E.-K. Tien, *et al.*, "Pulse compression and modelocking by using TPA in silicon waveguides," *Opt. Express,* vol. 15, pp. 6500-6506, 2007.

[47] M. Dinu, *et al.*, "Third-order nonlinearities in silicon at telecom wavelengths," *Applied Physics Letters,* vol. 82, p. 2954, 2003.

[48] H. Yamada, *et al.*, "Nonlinear-optic silicon-nanowire waveguides," *Japanese Journal of Applied Physics Part 1-Regular Papers Brief Communications & Review Papers,* vol. 44, pp. 6541-6545, 2005.

[49] H. Rong, *et al.*, "Raman gain and nonlinear optical absorption measurements in a low-loss silicon waveguide," *Applied Physics Letters,* vol. 85, pp. 2196-2198, 2004.

[50] L. Liao, *et al.*, "High speed silicon Mach-Zehnder modulator," *Opt. Express,* vol. 13, pp. 3129-3135, 2005.

[51] L. Yin, *et al.*, "Soliton fission and supercontinuum generation in silicon waveguides," *Opt. Lett.,* vol. 32, pp. 391-393, 2007.

[52] A. D. Bristow, *et al.*, "Two-photon absorption and Kerr coefficients of silicon for 850–2200 nm," *Applied Physics Letters,* vol. 90, p. 191104, 2007.

[53] Q. Lin, *et al.*, "Dispersion of silicon nonlinearities in the near infrared region," *Applied Physics Letters,* vol. 91, p. 021111, 2007.

[54] O. Boyraz, *et al.*, "Self-phase-modulation induced spectral broadening in silicon waveguides," *Opt. Express,* vol. 12, pp. 829-834, 2004.

[55] H. K. Tsang, *et al.*, "Optical dispersion, two-photon absorption and self-phase modulation in silicon waveguides at 1.5 mu m wavelength," *Applied Physics Letters,* vol. 80, pp. 416-418, 2002.

[56] H. Fukuda, *et al.*, "Four-wave mixing in silicon wire waveguides," *Opt. Express,* vol. 13, pp. 4629-4637, 2005.

[57] R. Espinola, *et al.*, "C-band wavelength conversion in silicon photonic wire waveguides," *Opt. Express,* vol. 13, pp. 4341-4349, 2005.

[58] H. K. Tsang and Y. Liu, "Nonlinear optical properties of silicon waveguides," *Semiconductor Science and Technology,* vol. 23, p. 064007, 2008.

[59] H. S. Rong, *et al.*, "Raman gain and nonlinear optical absorption measurements in a low-loss silicon waveguide," *Applied Physics Letters,* vol. 85, pp. 2196-2198, 2004.

[60] T. K. Liang and H. K. Tsang, "Nonlinear absorption and Raman scattering in silicon-on-insulator optical waveguides," *IEEE Journal of Selected Topics in Quantum Electronics,* vol. 10, pp. 1149-1153, 2004.

[61] G. W. Rieger, *et al.*, "Nonlinear propagation of ultrafast 1.5 mu m pulses in high-index-contrast silicon-on-insulator waveguides," *Applied Physics Letters,* vol. 84, pp. 900-902, 2004.

[62] E. Dulkeith, *et al.*, "Self-phase-modulation in submicron silicon-on-insulator photonic wires," *Optics Express,* vol. 14, pp. 5524-5534, 2006.

[63] P. Apiratikul, *et al.*, "Nonlinearities in porous silicon opticalwaveguides at 1550 nm," *Opt. Express,* vol. 17, pp. 3396-3406, 2009.

[64] K. Preston, *et al.*, "High-speed all-optical modulation using polycrystalline silicon microring resonators," *Applied Physics Letters,* vol. 92, pp. 151104-3, 2008.

[65] P. G. Coleman, *et al.*, "Simple expression for vacancy concentrations at half ion range following MeV ion implantation of silicon," *Applied Physics Letters,* vol. 80, p. 947, 2002.

[66] A. P. Knights and G. F. Hopper, "Effect of ion implantation induced defects on optical attenuation in silicon waveguides," *Electronics Letters,* vol. 39, p. 1648, 2003.

[67] T. Barwicz, *et al.*, "Reconfigurable silicon photonic circuits for telecommunication applications," San Jose, CA, USA, 2008, pp. 68720Z-12.

[68] C. W. Holzwarth, *et al.*, "Device Architecture and Precision Nanofabrication of Microring-Resonator Filter Banks for Integrated Photonic Systems," *Journal of Nanoscience and Nanotechnology,* vol. 10, pp. 2044-2052, 2010.

[69] A. Mecozzi and J. Mørk, "Theory of heterodyne pump-probe experiments with femtosecond pulses," *J. Opt. Soc. Am. B,* vol. 13, pp. 2437-2452, 1996.

[70] S. M. Sze and K. K. Ng, *Physics of semiconductor devices*, 3rd ed. Hoboken, N.J.: Wiley-Interscience, 2007.

[71] C. Koos, *et al.*, "Nonlinear silicon-on-insulator waveguides for all-optical signal processing," *Opt. Express,* vol. 15, pp. 5976-5990, 2007.

[72] Q. Lin, *et al.*, "Nonlinear optical phenomena in silicon waveguides: modeling and applications," *Opt. Express,* vol. 15, pp. 16604-16644, 2007.

Chapter 5

Semiconductor Saturable Absorbers

Abstract:

Ultrafast dynamics of semiconductor saturable absorber mirrors were studied. Addition of resonant layers to the absorbers resulted in lower saturation fluence and increased non-saturable loss. Proton bombardment of the devices was utilized to lower the carrier recovery times. Proton bombardment of single-absorber saturable absorbers with 40KeV proton energies at a dose of $10^{15}/cm^2$, a 1.5ps carrier recovery time was achieved in single-absorber structures. Double-absorber structures were fabricated and studied. Carrier lifetimes of these devices were also lowered by proton bombardment using different combinations of doses and proton energy levels.

5.1. Introduction

Ultrafast lasers generating pulses in the range of picoseconds to femtoseconds have received a great deal of attention in the recent years. Some of the applications that have benefited greatly from the recent developments in ultrafast lasers are optical arbitrary wave form generation[1-4], frequency metrology[5-8], medical imaging[9-11], surgery[12, 13], astrophysics[14], and machining[15, 16]. Even with relatively low power lasers, ultrashort pulses enable generation of high peak powers that make efficient nonlinear optics and even micro-machining possible. The ultrabroad bandwidths of such pulses provide for high resolution 3-D imaging as well as novel communication applications. Repetitive trains of such pulses allow for a range of applications, facilitating studies of nonlinear optical behavior and fundamental dynamics of materials[17-27]. The temporal resolution of these measurements is limited only by the pulsewidth and not that of the electronics. Therefore, shorter pulses improve this resolution and enable the study of the ultrafast carrier dynamics in semiconductor structures.

Generation of ultrashort pulses using solid state lasers is achieved by passive mode-locking. Some of the shortest pulses are generated using Kerr-lens mode-locking (KLM) [28, 29] or in fibers, nonlinear polarization rotation[30-35]. One drawback of both these methods is that they are often not self-starting. Semiconductor saturable absorber elements can be added to facilitate self-starting[36, 37]. Furthermore, for lasers in which the reactive nonlinearity is too weak for KLM or nonlinear polarization rotation, semiconductor saturable absorbers become the principal mode-locking elements. Short, high repetition-rate, mode-locked fiber lasers, for example, depend upon saturable absorbers[38] and are an important application for the devices investigated in this thesis.

In a mode-locked laser, the pulsewidth is related to the bandwidth of the optical signal by the Fourier transform, hence shorter pulses in the time domain require larger optical bandwidth. With the advent of bandgap engineering and semiconductor fabrication technology, the bandwidth of the saturable absorbers can be designed to cover bandwidths in the order of 100nm [39, 40]. Other important characteristics of saturable absorbers are the carrier lifetime, saturation energy, and absorption wavelength. These parameters are discussed in detail in the following sections.

The work in this chapter has been a collaborative effort amongst several different groups at MIT. The saturable absorbers discussed in this chapter were designed by fellow graduate students Hanfei Shen and Michelle Sander. They were fabricated in Professor Kolodziejski's group by Dr. Gale Petrich. Reflectivity measurements were performed by Michelle Sander on the FTIR measurement equipment at MIT, and some of the SBRs investigated for this work, were tested in mode-locked lasers by Hyunil Byun in Professor Kärtner's group. In the following sections, I will present results of the study of the ultrafast carrier dynamics and pulse saturation energies of several different saturable absorbers.

5.2. Background

We start the discussion of this section with a discussion on how a typical saturable absorber works. Several parameters that must be considered include the center wavelength and bandwidth, saturation property, and the temporal response of the device. The center wavelength and the bandwidth of the device dictate the usefulness of the device for a particular application. The saturation characteristic consists of two main parameters, saturable loss and non-saturable loss. Saturable loss, as the name suggests, is the amount of the loss in the device that can be saturated

with high enough optical fluence. The non-saturable loss is dependent on the structure and the purity of the constituent material, and it is the amount of loss that cannot be overcome with incident fluence at any energy level. Saturation fluence is the energy level at which the saturable absorber is bleached by 2dB. Several carrier dynamics contribute to the temporal response of a saturable absorber to short pulses, including instantaneous nonlinearity, carrier-carrier scattering, carrier cooling, and carrier lifetime. The faster times inherent to the material, but shows carrier lifetime in semiconductor can be reduced by low-temperature growth techniques[41-43] or proton bombardment[18, 44, 45] both of which result in defect states in the band structure that facilitate non-radiative recombination. In the following sections, we will describe investigations and observations of each of these properties.

5.2.1. Optical bandwidth and center wavelength

Figure 5-1 shows a typical structure of a semiconductor saturable absorber mirror or saturable Bragg reflector (SBR). The index profile of the structure and the square of the electric field standing wave pattern at 1560nm are shown. In this figure, the light impinges on the sample from the right-hand side. The SBR consists of an absorber layer grown on a Bragg stack consisting of several alternating layers of high and low index materials. The absorber layer can be made up of bulk semiconductor, quantum wells, or even quantum dots. The common feature amongst all is that the absorber must be designed to have a bandgap near the wavelength of interest. As depicted in this figure, the absorber layer consists of a thin layer of $In_{1-x}Ga_xAs$ where x is selected for a bandgap corresponding to a 1.56μm wavelength. This absorber layer is grown on top of a Bragg stack consisting of 20 to 40 pairs of GaAs/AlGaAs layers. The thickness of each layer is chosen to be quarter-wave thick at the center wavelength of interest. The overlap of the

E-field with the absorber layer determines how effective the incident fluence is at saturating the absorber. Generally, the SBR is designed so that the peak of the E-field intensity coincides with the absorber layer. This results in lower saturation fluence levels. Since the thickness of each layer is designed to be a quarter-wave long for a particular wavelength, the peak of the square of the E-field moves as a function of the wavelength. Therefore, the level of overlap between the absorber and the field intensity also changes as a function of wavelength. This demonstrates that the saturation fluence is a function of the wavelength and needs to be carefully characterized. In an SBR, the combination of the Bragg stack and bandgap engineering of the absorber layer dictate the center wavelength and the bandwidth. The desirable feature of this device is that the SBR itself can be used as one of the end mirrors in a laser cavity.

Figure 5-2 shows an example of a mode-locked fiber laser. The gain medium consists of an Er-doped fiber section pumped by a 977nm diode laser. At one end of the laser cavity a saturable absorber is mounted on a heat sink and is utilized as one of the cavity mirrors. At the other end of the cavity, a dichroic mirror is used as a partial reflector and as an input/output coupler. The dichroic beam splitter transmits the pump and reflects the laser output for use.

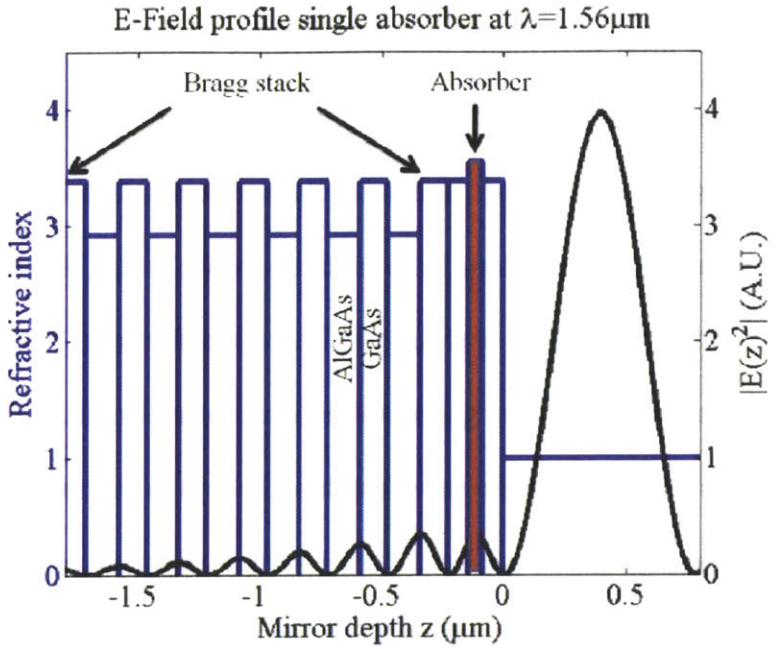

Figure 5-1 – Typical structure of a semiconductor saturable absorber consisting of an InGaAs absorber layer grown on top of a Bragg-stack made up of AlGaAs and GaAs. The peak of the E-field intensity overlaps with the absorber. The light impinges on the sample from the right side of the figure.

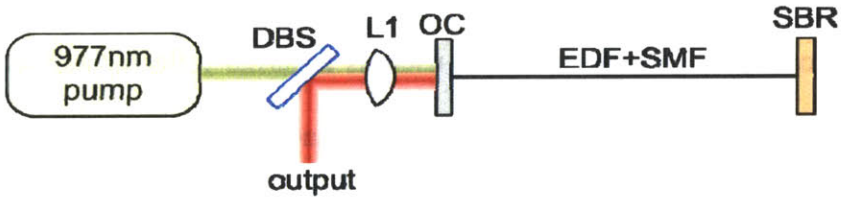

Figure 5-2 – Semiconductor saturable absorber (SBR) mounted on a heatsink in a mode-locked fiber laser at 1560nm. The gain medium consists of an Er doped fiber pumped by a 977nm pump diode. The output at 1560 is taken out of the cavity using a dichroic beam splitter (DBS). (Courtesy of Hyunil Byun.)

5.2.2. Saturation properties

The dynamic behavior of an SBR consists of multi-temporal response. The light incident on an SBR excites the electrons in the valence band of the absorber layer to the conduction band. As more electrons are excited with increasing intensity, the device becomes more transparent. At

high enough intensities, the absorber is fully "bleached" and transparent to the incident beam, therefore, the optical signal is fully reflected by the Bragg-mirror. This mechanism favors laser operations at high intensity which in turn leads to pulsed and mode-locking operation. In addition, saturable absorbers offer spatial beam shaping by resulting in higher attenuation of the low-intensity regions of a spatially Gaussian beam. An example of the saturation behavior of a saturable absorber is depicted in Figure 5-3. In this figure, the reflectivity of a semiconductor saturable absorber is plotted as a function of the pulse fluence which is the measure of pulse energy per area.

The important saturation parameters of a saturable absorber are saturable loss, non-saturable loss, modulation depth, and saturation fluence. The saturation behavior of an SBR, as shown in Figure 5-3, starts with low-reflectivity at low fluences. With the rising fluence, the reflectivity of the device increases, and in an ideal case, it would reach a maximum that is only dictated by the quality of the material and the reflectivity of the Bragg mirror. However, before it reaches this maximum, the reflectivity of the SBR rolls-off and starts to decrease with increasing fluence due to nonlinear effects such as two-photon absorption (TPA). A saturable absorber also exhibits a certain non-saturable loss which is independent of the pulse fluence. This non-saturable loss is dependent on roughness scattering as well as the fundamental properties of the material. It is an undesirable factor since it adds additional loss to the laser cavity. The modulation depth of an SBR is the maximum differential reflectivity that can be obtained. In this example, it is approximately 3%. The maximum saturable loss alone is demonstrated in this figure by ΔR. This maximum is typically unattainable since the TPA and other nonlinearities start to dominate at high fluences and reduce the reflectivity of the device. Finally, saturation fluence is the fluence at which the saturable loss is bleached by 2dB and is influenced by the

material composition and the geometry of the device. In high repetition rate lasers, it is desirable to reduce the saturation fluence, and this can be accomplished by placing the absorber layer at the peak of the electric field standing wave and/or placing a resonant coating on the top layer to enhance the peak of the electric-field standing wave.

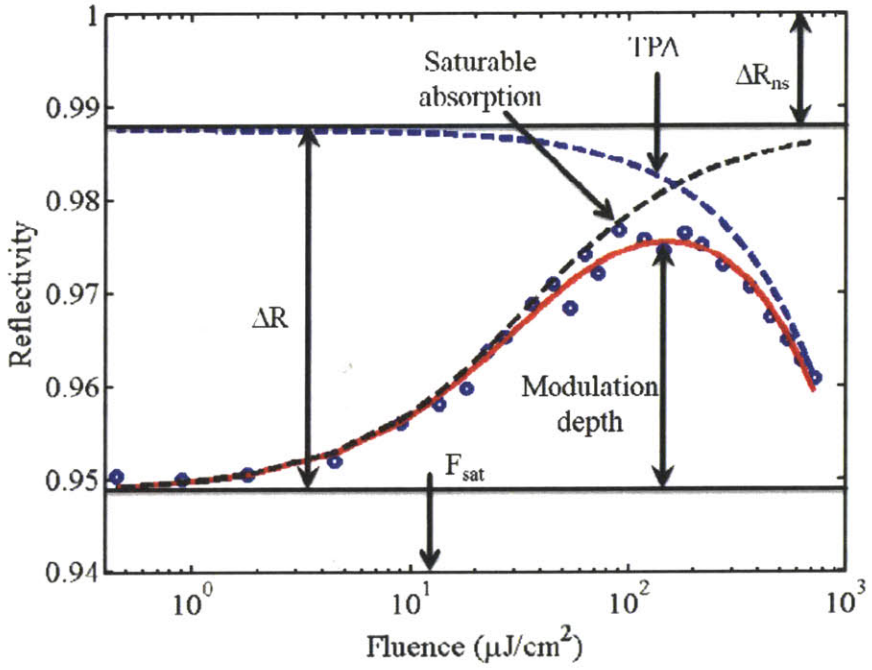

Figure 5-3 – An example of a saturation response of a semiconductor saturable absorber. Starting from low fluence levels, the reflectivity rises with increasing fluence. However, at high fluences, nonlinear processes such as two-photon absorption (TPA) dominate and limit the reflectivity.

5.2.3. Temporal dynamics

The temporal dynamics of a saturable absorber are measured using a pump probe technique which is discussed in detail in Section 5.3. In general, in a pump probe experiment, the device is excited with a high power optical signal, called 'pump', and a much lower-power pulse 'probe' measures the induced changes by the pump. An example of a pump probe trace on an InGaAs saturable absorber is shown in Figure 5-4. In this figure, the change in the reflectivity of the saturable absorber is plotted as a function of time after the pump has passed through the device.

As discussed in the previous section, there are two phenomena that occur in the device as a function of the fluence. One is bleaching which occurs at low fluences and results in increased reflectivity, while nonlinear intensity-dependent processes such as two-photon absorption and free-carrier absorption result in increased losses and dominate the saturable absorber response at high fluences. When light impinges on an absorber above the bandgap, there is an instantaneous response which results in the excitation of the electrons in the valence band to the conduction band. The carriers in this instant occupy bands of states corresponding to the spectral width of the pulse as demonstrated in Figure 5-4a. This creates a spectral 'hole' in the absorption spectrum. The hot carriers that are generated in this process then undergo carrier-carrier scattering which breaks up the coherence of electrons and holes, diffuses the spectral-hole and redistributes the carriers into a new "hot" Fermi distribution as indicated in Figure 5-4b. All of this process occurs in less than 200fs. The redistributed carriers then interact with the lattice emitting phonons and losing their energy. In about 1 to 2ps a Fermi distribution at equilibrium with the lattice temperature is reached as illustrated in Figure 5-4c. The extent of absorption bleaching that can be accomplished by the optical pulse is a function of pulse duration and photon energy relative to the band-edge. The saturation fluence, F_{sat} is that at which a specific pulse reduces its own saturable absorption by *(1-1/e)*.

Over a much longer period the electrons and holes recombine via non-radiative as well as radiative processes. This recombination process can take from a few picoseconds to several nanoseconds depending on the purity of the material and defects in the crystal structure.

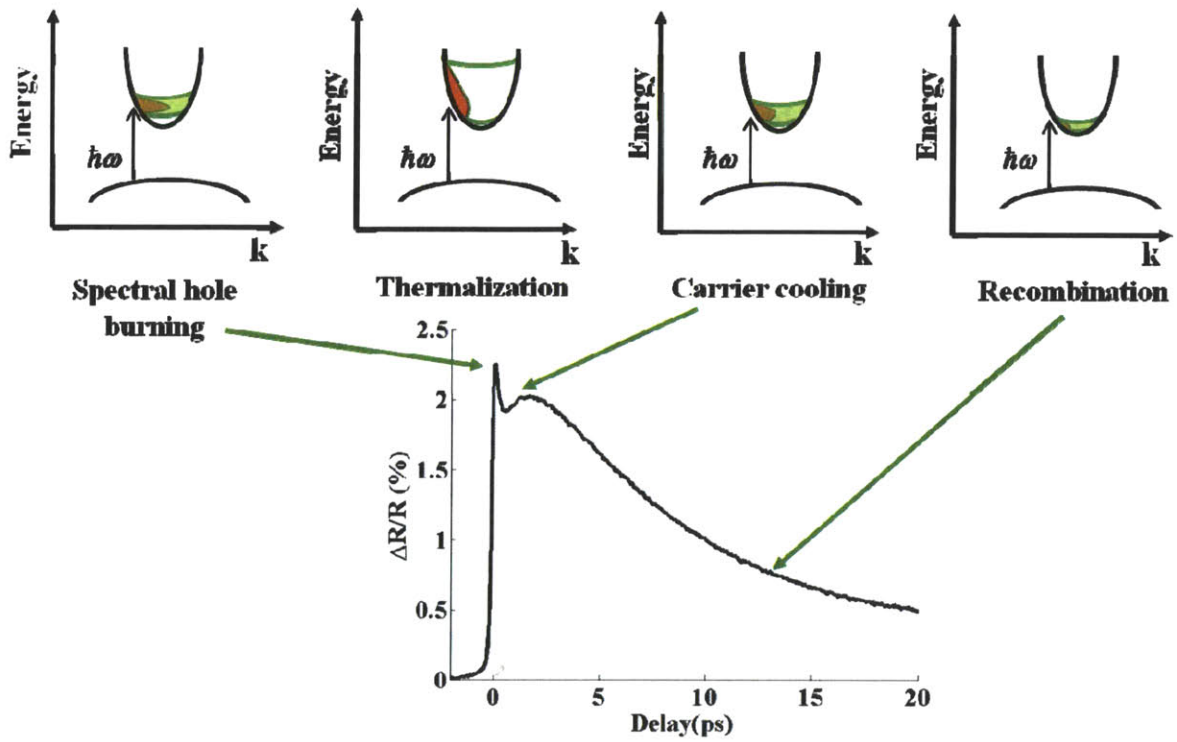

Figure 5-4 – An example of the pump probe traces obtained from a saturable absorber demonstrating the different carrier dynamics.

The nonlinear optical losses as discussed in previous sections occur due to TPA and FCA processes. The TPA occurs when the pump and probe are at zero delay with respect to each other. In this process, two photons are absorbed generating an electron-hole pair. The carriers in the conduction band can also absorb light and get further excited in the conduction band, resulting in further loss called free-carrier absorption.

5.3. Measurement techniques

To study the ultrafast carrier dynamics and saturation characteristics of variety of semiconductor saturable absorbers, a cross-polarized pump probe experiment was utilized. This is applicable in this case because the reflections and responses of the devices are polarization independent. In these experiments, the device under test (DUT) is excited by a high power pump signal, and at a

variable delay after the pump, a much weaker "probe" signal is incident on the device to probe the changes imposed by the pump pulse. The pump-induced modulation of the reflected probe signal is detected. The function of the pump is to excite the sample from its equilibrium state and the probe to determine the amount of change imposed as the device relaxes back to equilibrium. From the differential change in the amplitude of the probe signal, the effects of the various nonlinearities of the device can be observed, including the TPA, carrier-carrier scattering, and carrier lifetime. The schematic diagram of a cross-polarized pump probe measurement technique is shown in Figure 5-5.

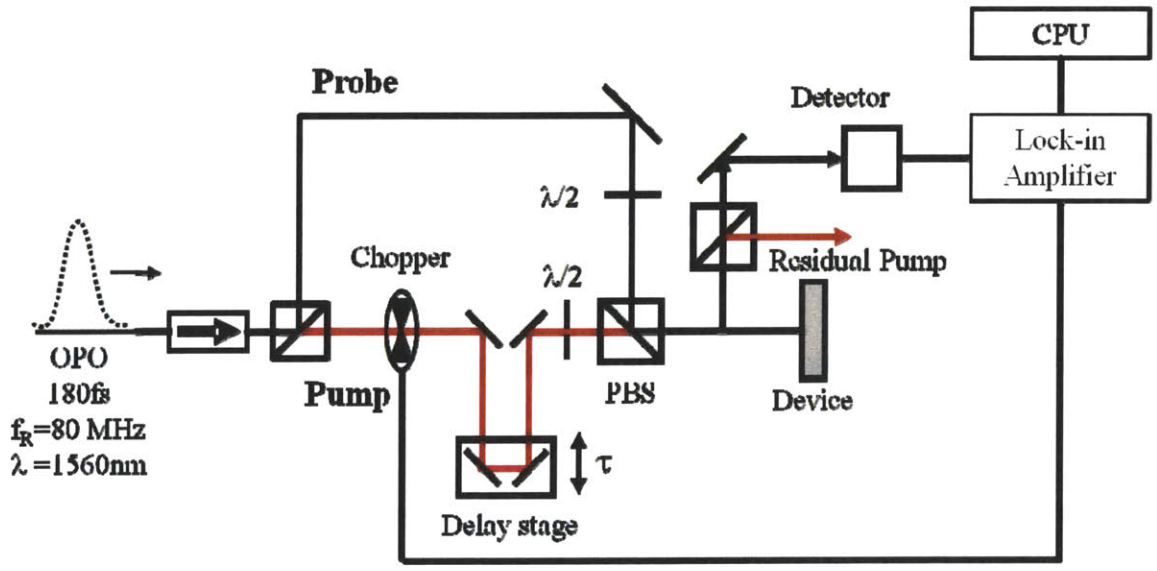

Figure 5-5 – Schematic diagram of a cross-polarized pump probe experiment using an optical parametric oscillator tunable between 1.1 to 1.6 μm producing pulses of 150fs duration at 80MHz repetition rate.

The optical source for this experiment is a Spectra-Physics optical parametric oscillator (OPO) tunable between 1.1 and 1.6μm. The OPO is synchronously pumped by 80fs pulses generated by a Ti:Sapphire laser at 810nm. The OPO produces 150fs pulses at a repetition rate of 80MHz. The maximum temporal resolution of this setup is limited by the full-width half-

maximum of the cross-correlation between the pump and probe signals, and in this case the best temporal resolution is 212fs. The optical pulses from the OPO after passing through an isolator, are split into two paths using a 30:70 coupler. The higher power being the pump is passed through a mechanical chopper, a delay stage, and a half-wave plate. The lower power signal is the probe signal and is passed through a half-wave plate and combined with the pump signals on a polarizing beam splitter (PBS). The combination of the half-wave plates and the PBS in each arm of the pump and probe paths allows for independent control of the pump and probe powers incident on the sample. The combined pump and probe signals are at this point cross-polarized and they are co-linearly focused using a lens onto the sample. A small fraction of the reflected beam from the sample is directed towards a photodetector. A polarizing beamsplitter filters the pump signal, and only the probe is detected. The output of the detector is connected to a lock-in amplifier which detects the modulation on the probe signal at the chopping frequency. The output of the lock-in amplifier is connected to a computer which collects the data as a function of the delay.

The saturable absorption dynamics described in the previous section are dependent on the fluence of the incident light. In the above experiment, a lens was utilized to focus the beam on the sample, therefore, with changes in the focal length of the lens as well as by attenuating the beam, a wide range of fluences can be achieved. To determine the fluence on the sample, the beam diameter of the optical beam at the focal plane of the lens has to be measured. The "knife-edge" technique was used to measure the beam diameter [46]. In this method, a sharp razor blade was placed on a translation stage and the blade was used to gradually block the optical beam as the unblocked power of which was measured using an optical power meter. The optical power as a function of the position of the blade in the optical field plotted and fit to an erf function. The

measurement was made at several different points away from the lens and the beam diameter at the focal plane of the lens was determined. Knowing the beam waist, we can determine the fluence from

$$F = \frac{PT}{\pi w^2}, \tag{5.1}$$

where P is the average optical power, T is the repetition period of the laser, and w is the full-width half maximum beam radius on the sample.

5.4. Theoretical Models

In this section, the models used to extract the saturation parameters and the recovery times of the saturable absorbers are described.

5.4.1. Saturable absorption energy

The models predicting the saturation fluence of a saturable absorber require an assumption about the dynamic recovery time of the device. A device that has a recovery time longer than the pulsewidth of the laser, saturates with pulse energy, while a saturable absorber has a recovery time shorter than the pulsewidth saturates with intensity. Detailed derivations of these models are given in several references [47, 48]. In this chapter, devices are tested using 150fs pulses from an optical parametric oscillator (OPO). Although these saturable absorbers have fast recovery components, they all exhibit recovery times from a few to tens of picoseconds. For simplicity, we will compare experimental saturation fluence results with the theory for a slowly recovering absorber.

The reflectivity of a saturable absorber is given by

$$R = 1 - q - q_{TPA} - R_{ns}, \tag{5.2}$$

where R is the SBR reflectivity, q is the saturable absorption, q_{TPA} is the TPA loss, and R_{ns} is non-saturable loss. The saturable absorption is determined from pump-probe experiments in which the probe beam-waist was 0.75 times that of the pump, and is given by (Appendix E):

$$q(F) = q_0 \left(\frac{F_{sat}}{F} \right)^m \int_0^{F/F_{sat}} \frac{\left(1 - e^{-z}\right)}{mz^2} z^m dz, \tag{5.3}$$

where q_0 is saturable loss, F_{sat} is the saturation fluence, F is the fluence of the incident pump, and m is the square of the ratio of the pump and probe beam-waists given by

$$m = \frac{w_{pump}^2}{w_{probe}^2}. \tag{5.4}$$

Using the above equation, we were able to extract out the saturable loss, saturation fluence, and non-saturable loss of the samples.

5.4.2. Recovery time

The differential reflectivity measured using a pump-probe experiment is the convolution of the cross-correlation intensity with the transfer function of the saturable absorber. This can be described by [49]

$$\Delta R\left(\tau_{probe}\right) = \int_{-\infty}^{\infty} h\left(\tau_{probe} - t'\right) X\left(t'\right) dt', \tag{5.5}$$

where ΔR is the change in the reflectivity of the SBR, $X(t)$ is the cross-correlation of the pump and probe pulses, and *h(t)* is the transfer function of the sample. The transfer function *h(t)* is based on the temporal dynamics described in Section 5.2.3, and is modeled by [46]

$$h(t) = a_0\delta(t) + \left(a_1 e^{-\frac{t}{\tau_1}} + a_2 e^{-\frac{t}{\tau_2}} + a_3 \right) u(t), \tag{5.6}$$

where a_0 is the instantaneous response, $\delta(t)$ is the Dirac delta function, τ_1 and τ_2 are the carrier cooling, and long recovery times, respectively, a_3 is a rise in temperature, and $u(t)$ is a unit step function. This model is utilized to extract the various different relaxation times.

5.5. Saturable absorbers

Several different types of SBRs were designed and tested for this work. The goal of using different designs is to study and understand the trade-offs among saturation fluence, non-saturable loss, saturable loss, and recovery time of an SBR and to provide data for comparison with results obtained from their use in laser mode-locking. One of the main challenges in the design of high-repetition rate lasers is to generate high enough fluence per pulse to fully bleach a saturable absorber. In a mode-locked laser, for a constant intracavity average power, with increasing repetition rate, the energy per pulse is reduced, resulting in lower fluence on the saturable absorber. Therefore, it is necessary to engineer devices with lower saturation fluence. This can be accomplished by designing the layer thicknesses so that the absorber layer is placed at the peak of the incident field. The saturation fluence can be further reduced by enhancing the standing-wave field pattern with a resonant coating on the top layer of the SBR [46, 48].

Another parameter of a saturable absorber that plays an important part in the design of high repetition lasers is the recovery time of the device. As discussed in the previous Sections, the recovery time depends on the purity and quality of the crystal structure of the absorber material. Certainly, the recovery time of an SBR should be shorter than the round-trip time of

cavity to ensure maximum per-pulse effect. The optimum relationship between ultrafast recovery that can lead to the shortest pulses and a somewhat longer component that can assist in self-starting to the mode-locking, is not yet fully understood.

SBR samples in the first group that were studied were designed with a single InGaAs absorber on top of a Bragg reflector consisting of AlGaAs and GaAs. Effects of proton bombardment at various energies and doses on the temporal and saturation properties of these SBRs were also investigated as part of the pump-probe study. The design of the second group of SBRs was based on a single absorbing layer with an additional resonant coating on the top layer. Temporal and saturation properties of these SBRs were also studied in detail. Finally, the third group of SBRs consisted of two absorbing layers placed in layers of GaAs and grown on top of a Bragg reflector consisting of AlGaAs and GaAs layers. The goal of multilayer absorbers in the SBR was to increase the amount of available saturable absorption.

5.5.1. Single absorber

Saturable absorbers discussed in this section consisted of a 60nm $In_{0.537}Ga_{0.463}As$ absorber embedded in a half-wave cladding layer on 22-pairs of $GaAs/Al_{0.95}Ga_{0.05}As$ reflector mirror centered at 1550nm. The InGaAs absorber layer was designed to have 1580nm band edge and it was placed inside a layer of GaAs. The structure of this device is shown in Figure 5-6 with the E-field standing-wave pattern at λ=1560nm superimposed. The optical field impinges on the sample from the right hand side. The $\lambda/2$ top cladding layer is designed to maximize transmission of the optical field into the device.

The structure of the device consists of, from the left, 22 pairs of AlGaAs/GaAs. Each layer is fabricated to be λ/4 thick at the center wavelength of interest. The E-field standing wave in this figure is calculated for a single wavelength of 1560nm. Since the optical path length of each layer varies with the wavelength, the overlap between the absorber layer and the E-field standing wave pattern will also change as a function of wavelength. Therefore, careful fabrication of the devices plays an important part in the saturation properties of the device as will be discussed in the later section. The reflectivity of the device was measured and compared to that predicted by the design. The measurement demonstrates a shift in the center wavelength of the device by approximately 10nm to lower wavelengths as depicted in Figure 5-7. This can be due to the variation in the thicknesses of different layers of the Bragg mirror. The composition and thickness of different layers of the single-absorber are given in Table 5-1.

Table 5-1 – Composition and thickness of the different layers of the single-absorber saturable absorber (VA86)

Layers	Thickness (nm)
Top Cladding (GaAs)	83.2
Absorber ($In_{0.537}Ga_{0.463}As$)	60
Bottom Cladding (GaAs)	83.2
Bragg Mirror (GaAs/$Al_{0.95}Ga_{0.05}As$)	114.7/132.9

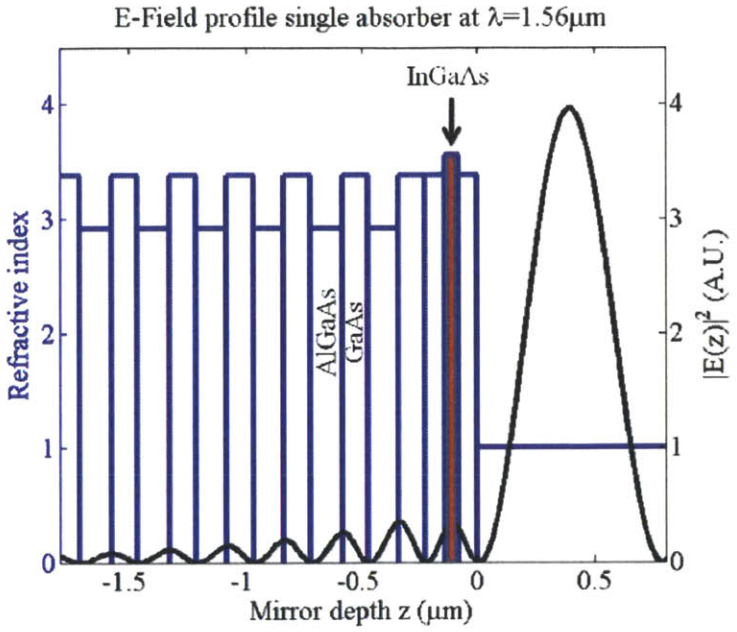

Figure 5-6 – Single absorber (VA86) saturable absorber structure and standing E-field pattern. Courtesy:Hanfei Shen.

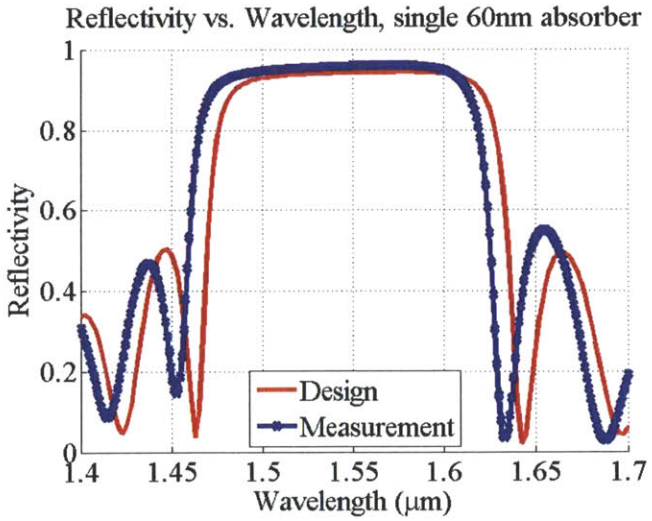

Figure 5-7 – Reflectivity of the single absorber layer measured vs design Courtesy:Hanfei Shen and Gale Petrich.

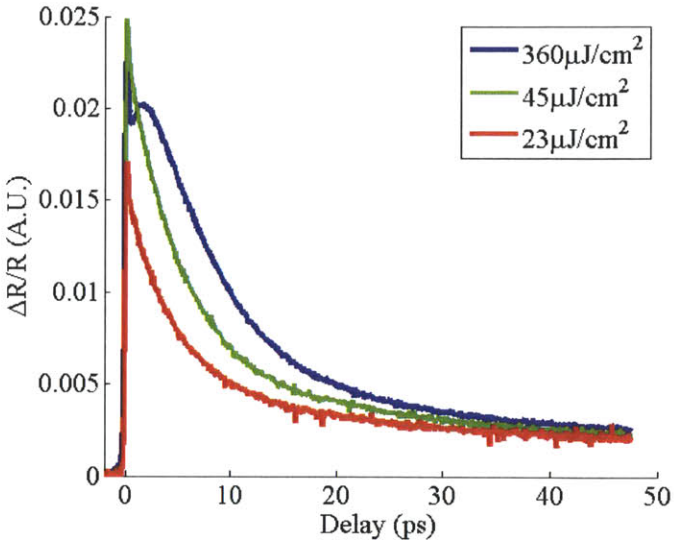

Figure 5-8 – Differential reflectivity of the single-absorber SBR as a function of the delay of the probe with respect to pump.

To study the effects of the proton bombardment on the carrier lifetime this device, the SBRs were sent out to Leonard Kroko, Inc., and were proton-bombarded with 40KeV protons and over a range of doses including 10^{13}, 5×10^{13}, 10^{14}, 3×10^{14}, and 10^{15} /cm^2. The protons of 40KeV are utilized to ensure that the defects reach the absorption layer and that with increasing dosage of proton-bombardment a larger number of defects are generated to shorten carrier lifetime. As shown in Figure 5-9, the device with no proton bombardment has a long recovery time in the order of 11ps, while the sample with 10^{15}/cm^2 proton bombardment recovers in less than 2ps.

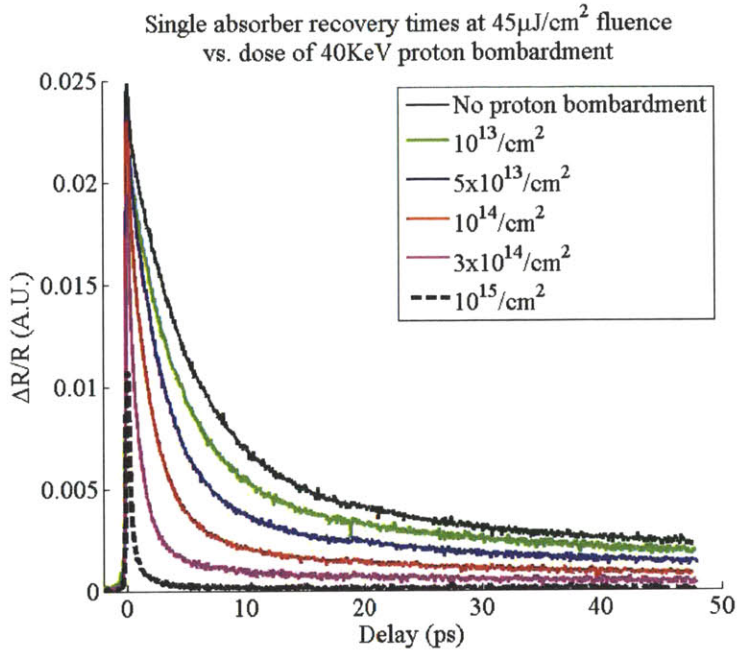

Figure 5-9 – Carrier recovery time of the single absorber device as a function of the proton bombardment doses. Proton energy used in this study was 40KeV to ensure that it reaches the absorber layers. Doses of proton-bombardment were 10^{13}, 5×10^{13}, 10^{14}, 3×10^{14}, and 10^{15} /cm^2.

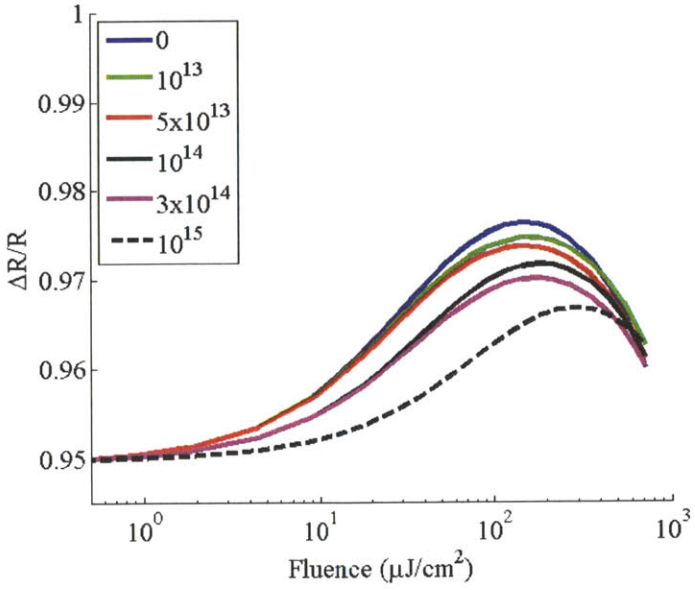

Figure 5-10 – Saturation dynamics of the single absorber (VA86) saturable absorbers as a function of the fluence on the sample. Each trace corresponds to a different proton bombardment dose.

The recovery times of these devices were extracted using Equation (5.5) and are tabulated in Table 5-2.As shown, the recovery times varied between 10.8ps with no proton bombardment down to 1.5ps with $10^{15}/cm^2$. And, from the saturation dynamics, the saturable loss, non-saturable loss, and the saturation fluence of each sample were determined and tabulated in Table 5-2.

Table 5-2 – Temporal and saturation parameters extracted for different proton bombardment levels of single InGaAs absorber design.

Proton dose ($/cm^2$)	Short recovery time, τ_1 (ps)	Long recovery time , τ_2 (ps)	Saturable loss q_0 (%)	Saturation Fluence, F_{sat} ($\mu J/cm^2$)	Non-saturable loss, R_{ns} (%)
0	1.5	10.5	3.9	12	1.1
10^{13}	1.5	9.9	3.5	11	1.5
5×10^{13}	1.5	7.5	3.3	10.5	1.7
10^{14}	1.3	5.6	3.2	12	1.8
3×10^{14}	1	4.9	3.0	14.3	2
10^{15}	0.4	1.5	2.9	34	2.1

Proton bombardment has resulted in a shorter recovery time in these samples. At doses above $3\times10^{14}/cm^2$ the recovery time of the sample is reduced below 1.5 ps, but additional non-saturable loss is introduced and the saturation fluence of the device has increased by almost 3 times to $34\mu J/cm^2$ with additional non-saturable loss. The large increase in non-saturable loss may be due to the addition of impurities and defects in the crystal structure. These implanted impurities can result in changes in the refractive indices of both GaAs and AlGaAs in the cladding layers and the Bragg stack. These variations would change the E-field standing-wave pattern inside the device, hence, altering the absorber layer overlap with the peak of the optical intensity and resulting in higher saturation fluence. Hence, although the faster recovery time of the device may be favorable for pulse-shortening, it requires 3 times higher fluence to saturate this device. And,

considering that increasing the repetition rate while keeping the average power inside the cavity constant results in lower fluence on the SBR, mode-locked operation may be difficult to achieve with a $10^{15}/cm^2$ proton bombarded sample. In the following section, we will discuss the effects of resonant layers in reducing the saturation fluence of a semiconductor saturable absorber.

5.5.2. Resonant structure

The proton-bombardment results of the previous section demonstrate the efficacy of this technique for reduction of carrier lifetimes. However, it introduces another challenge in the process, that for the highest doses, the saturation fluence of the device increases by a factor of 3. To reduce the saturation fluence, a resonant coating was added to the SBR. In this section, I will present the results obtained with such a resonant coating.

A resonant layer structure was grown on top of the single absorber design demonstrated in Figure 5-6. The addition of the resonant layer on the top results in the creation of a Fabry-Perot cavity between the top layer and the DBR stack with 70% reflectivity. The E-field standing wave pattern for this device was calculated and shows that the magnitude of the E-field on the absorber layer is 2.5 times greater than that of the SBR without the resonant cavity. The structure and the E-field standing wave for this device (VA88) are shown in Figure 5-11. The spectral bandwidth and the reflectivity of the device were also measured and compared to the design simulations. This is shown in Figure 5-11b.

Another saturable absorber using the same topology was created, except that instead of placing the single absorber layer in the cladding layer, it was placed in the first high index quarter wave layer of the mirror. This group of absorbers is named VA89. The E-field pattern and the result of the simulated and measured spectral width of the VA89 samples are shown in

Figure 5-12. Saturation fluence curves for each were measured and are shown in Figure 5-13. The composition of the two structures and the thicknesses of each layer are given in Table 5-3.

Table 5-3 – Composition and thickness of the VA88 and VA89 structure

Layers (Material)	VA88	VA89
Resonant layer ($Al_{0.95}Ga_{0.05}As$ / GaAs) x 3	133/115	133/115
GaAs	83	282
Absorber ($In_{0.537}Ga_{0.463}As$)	60	60
GaAs	83	-
$Al_{0.95}Ga_{0.05}As$	-	133
Bragg mirror (GaAs/ $Al_{0.95}Ga_{0.05}As$)	115/133	115/133
Substrate GaAs		

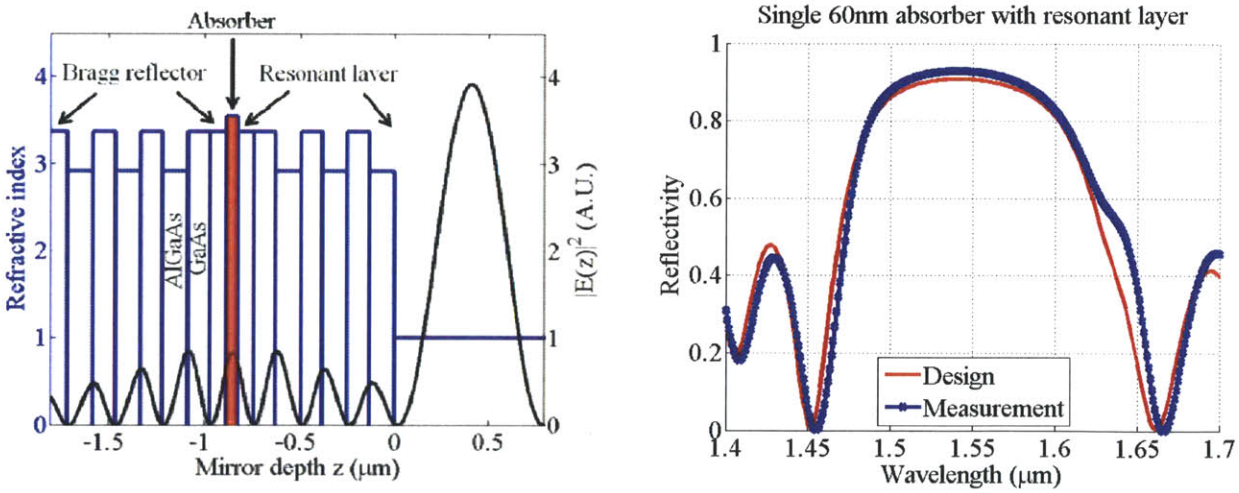

(a) (b)

Figure 5-11 – a)The structure of a single absorber saturable absorber (VA88) with the addition of resonant layer on top. The absorber consists of 60nm InGaAs layer in a GaAs cladding layer. b) Measured and simulated reflectivity of the single-absorber structure with top resonant layers. Courtesy: Hanfei Shen.

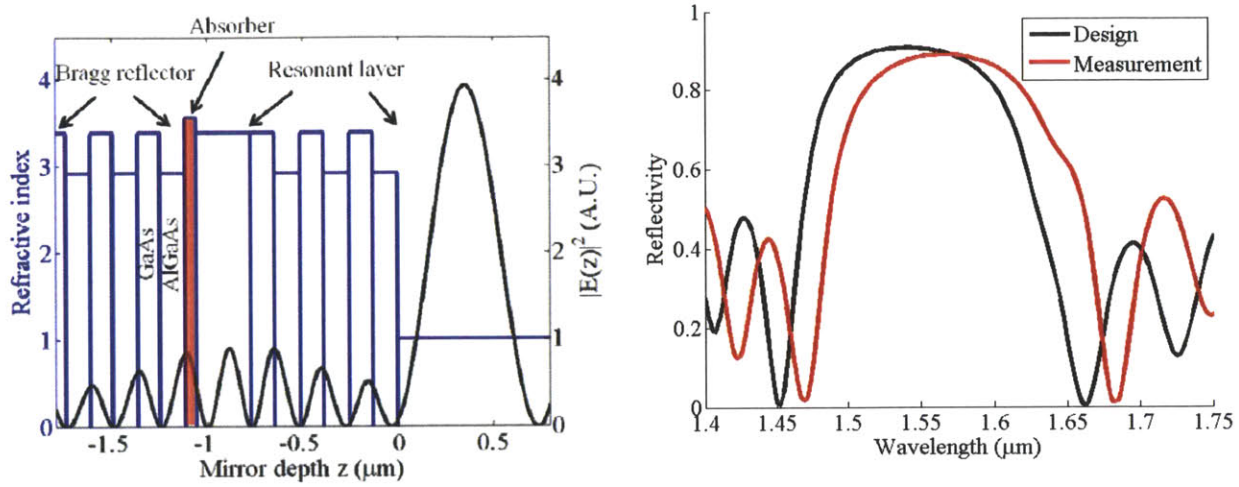

(a) (b)

Figure 5-12 – a)The structure of a single absorber saturable absorber (VA88) with the addition of resonant layer on top. The absorber consists of 60nm InGaAs layer in a GaAs cladding layer. b) Measured and simulated reflectivity of the single-absorber structure with top resonant layers. Courtesy: Hanfei Shen.

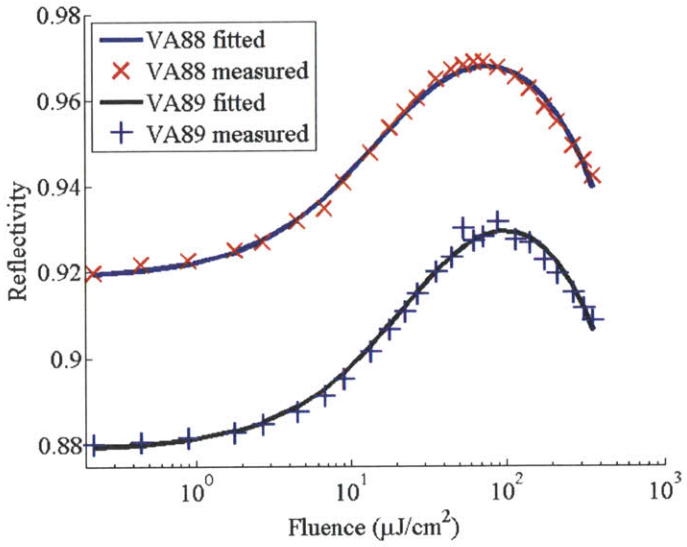

Figure 5-13 – Saturation fluence curves for VA88 and VA89, both measured and fitted.

Table 5-4 – Saturation parameters of VA88 and VA89 resonant saturable absorbers

Sample	Saturable loss q_0 (%)	Saturation Fluence F_{sat} (μJ/cm^2)	Non-saturable loss R_{ns} (%)
VA88	7	5.8	1.2
VA89	8	9.2	4.2

From the summary, we can see that the saturation fluence and nonsaturable loss of the VA89 sample are both larger than those of VA88. The larger saturation fluence can be explained by noting the fact that the absorber layer in VA89 does not perfectly align with the peak of the E-field, hence larger energy is required to saturate the device.

The resonant structure on top of a Bragg stack, creating a Fabry-perot cavity, can also be designed to exhibit a specific spectral response and provide additional optical filtering. The need for such functionality arose in the implementation of a compact 1GHz mode-locked laser that was developed in professor Kärtner's lab by Hyunil Byun. The structure of this laser is shown in Figure 5-14.

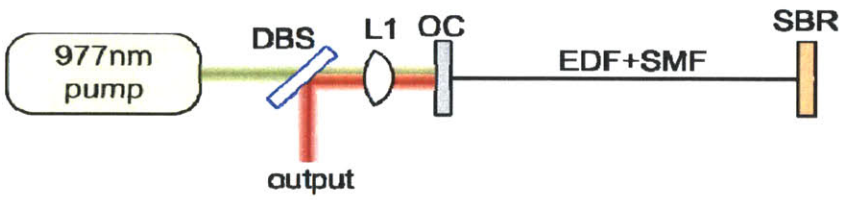

Figure 5-14 – Schematic diagram of the 1GHz compact Er doped waveguide mode-locked laser. Courtesy of Hyunil Byun

As shown in this figure, the gain in the laser cavity is provided by an Er-doped fiber section. The SBR is mounted on a heat sink and it is butt-coupled to the Er-doped fiber. The butt-coupling is meant to reduce the scattering, and coupling loss between the fiber, air, SBR, and back to the fiber. Due to the short-length of the cavity necessary to generate 1GHz repetition

rate, the length of the Er-doped fiber had to be kept fairly short which means that to achieve necessary optical powers to reach the saturation fluence of the SBR, this length of Er-doped fiber had to produce significant amount of gain. Gain of an EDFA is dependent on the length of the fiber, the doping, and the pump level. Since increasing the fiber length would reduce the repetition rate, as a solution to this problem, the increase of the pump level was explored. The active fiber was pumped with a 300mW diode pump at 977nm that was not all absorbed by the fiber. A significant portion of this power was incident on the SBR. This resulted in the operation of the laser for only a few minutes after which time the laser would fail. Careful trouble-shooting revealed burn spots on the single absorber structures. To solve this problem, a pump-reflective coating (PRC) was designed to reflect the 977nm pump wavelength and pass the 1560nm signal. The filter also resulted also in the enhancement of the E-field standing wave inside the device. The E-field profile and the structure of the device is shown in Figure 5-15.

The magnitude of the E-field on the absorber layer is approximately 3 times that of the uncoated single absorber structure (VA86). Therefore, as expected the saturation fluence of the PRC device is 3 times lower than the non-coated sample. The parameters for this device are extracted from the saturation fluence dynamics and compared to the uncoated VA86 sample.

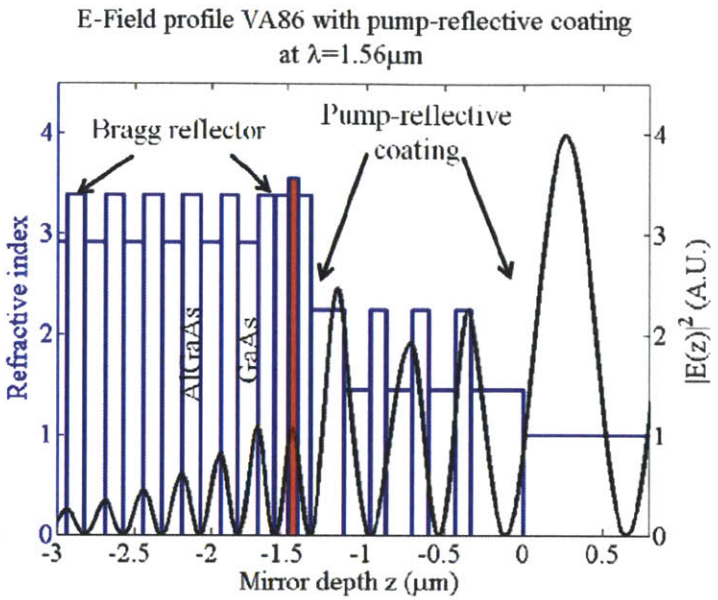

Figure 5-15 – E-field standing wave pattern of the pump-reflected coated VA86 structure.

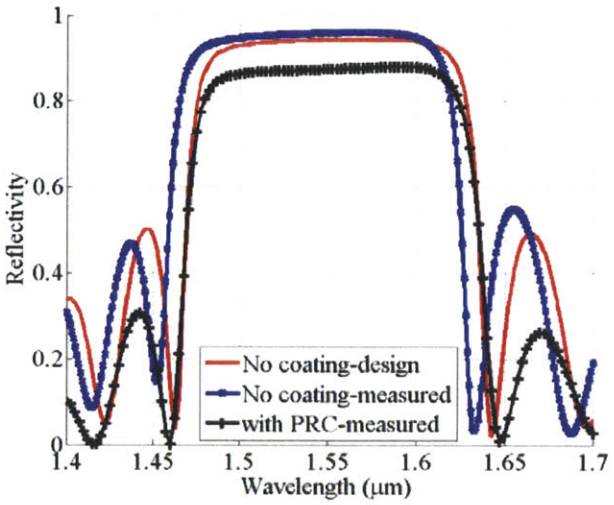

Figure 5-16 – Reflectivity of the VA86 uncoated and with pump reflective coating. The unbleached reflectivity of the PRC device is about 8% lower than the uncoated sample.

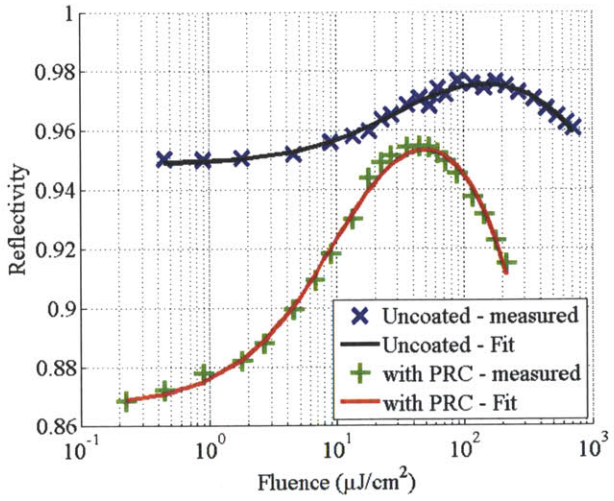

Figure 5-17 – Saturation dynamic of VA86 sample with and without pump-reflective coating (PRC). Addition of PRC results in larger modulation depth, and lower saturation fluence.

Table 5-5 – Saturation parameters of the VA86 with and without PRC.

Sample	Saturable loss q_0 (%)	Saturation Fluence F_{sat} (μJ/cm^2)	Non-saturable loss R_{ns} (%)
VA86 – with PRC	12	3.7	1.1
VA86 – no coating	3.9	12	1.1

The PRC layer has resulted in obtaining larger saturable loss and the saturation fluence has decreased by a factor of 3 down to 3.7 μJ/cm^2, while the non-saturable loss has not changed. The additional functionality of reflecting 977nm wavelength range has allowed for the integration of this saturable absorber in the compact 1GHz mode-locked laser with at least 60hours of stable operation [38].

5.5.3. Double-absorber device

To increase the amount of saturable absorption, multiple absorber layers are used instead of a single-absorber layer. In the studies of this section, we used two-absorber devices that were designed by Michelle Sander in professor Ippen's group. Two different geometries were fabricated with two 60nm $In_{0.537}Ga_{0.463}As$ absorber layers in GaAs layers. The difference between these two structures lies in the thickness of the top GaAs cladding-layer. The VA147 has 20nm thinner top layer in an effort to optimize the overlap of the absorbing layers and the square of the E-field. The composition of the each device is given in Table 5-6. Using this information, the standing-wave electric field patterns for these devices were calculated, and they are shown in Figure 5-18. The spectral widths of the two devices were measured and the results are shown in Figure 5-19. As shown in this figure, the reflectivity of VA147 rolls-off at longer wavelengths.

Table 5-6 – Thicknesses and composition of different layers of VA147 and VA148 saturable absorbers

Layers	Thicknesses (nm)	
	VA147	VA148
Cladding layer (GaAs)	62.3	82.3
Absorber layers (GaAs/InGaAs/GaAs)×2	62.3/69.8/62.3	62.3/69.8/62.3
Bragg stack (GaAs/AlGaAs)	114.5/129.5	114.5/129.5

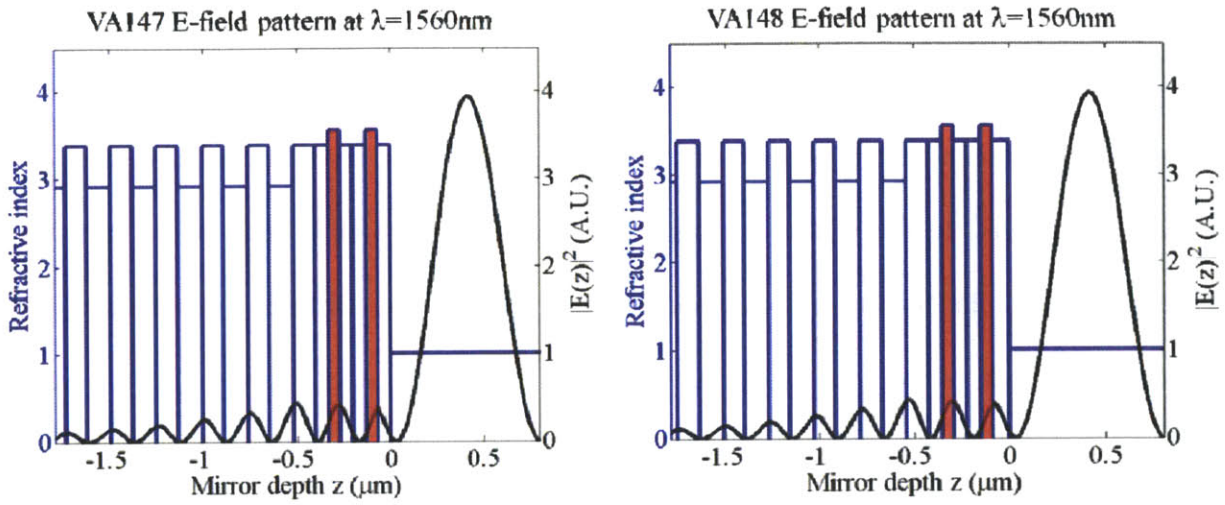

Figure 5-18 – The intensity of the optical field in the VA147 and VA148 saturable absorbers consisting of two InGaAs absorbing layers separated by GaAs cladding. The difference between the two designs lies in the thickness of the top layer. This results in a different overlap between the optical intensity and the InGaAs absorbing layers. Courtesy of Michelle Sander

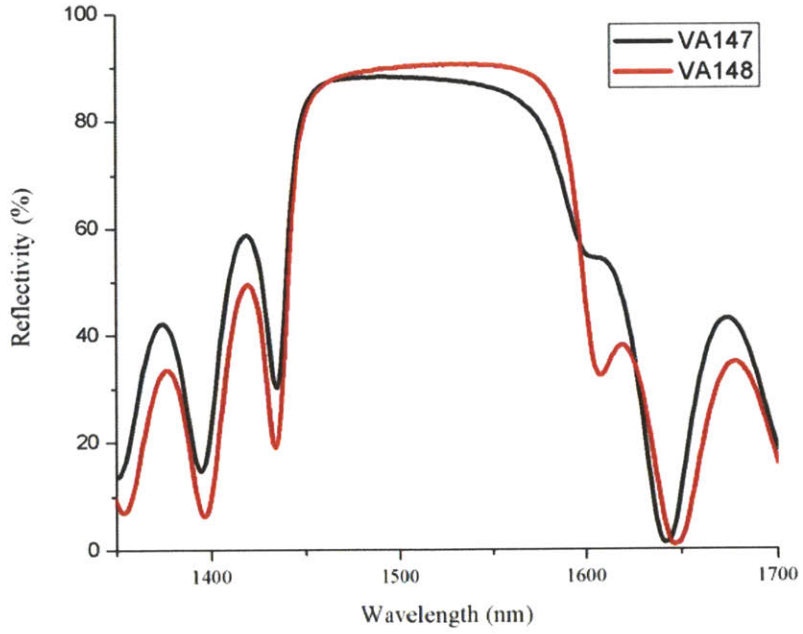

Figure 5-19 – Spectral bandwidth of VA147 and VA148. At 1560nm, the measured reflectivities of the SBRs are 85 and 90%, respectively. Courtesy of Michelle Sander.

The saturation and temporal dynamics of these samples were also studied. As expected, the recovery times of the two samples were both 11ps. The equality of the two recovery times is expected as the relaxation time depends on the quality of the material. The probe reflectivities as a function of pump-probe delay for both samples at a fluence of 25μJ/cm^2 are shown in Figure 5-20. The modulation depth of the VA147 sample is approximately twice that of VA148. Because of the double-absorber layer structure of the VA147 and VA148, they are expected to exhibit twice the modulation depth achieved with a single absorber layer such as VA86 with no resonant coating. As shown in this figure, VA147 exhibits nearly such modulation depth and it seems that compared to VA148, its design offers a more optimum overlap between the absorber layers and the peak of the E-field in the device is achieved.

Furthermore, the reflectivity of the two samples as a function of the fluence on the sample was also measured and the results are shown in Figure 5-21. The saturation parameters of the devices are extracted and summarized in Table 5-7. VA147 sample exhibits larger saturable loss and lower saturation fluence which are desirable characteristics for implementation in a mode-locked laser.

Table 5-7 – VA148 and VA147 saturable loss, saturation fluence, and non-saturable loss extracted from the measured data.

Sample	Saturable loss q_0 (%)	Saturation fluence F_{sat} (μJ/cm^2)	Non-saturable loss R_{ns} (%)
VA148	4	5.4	6.2
VA147	7.5	4.7	8

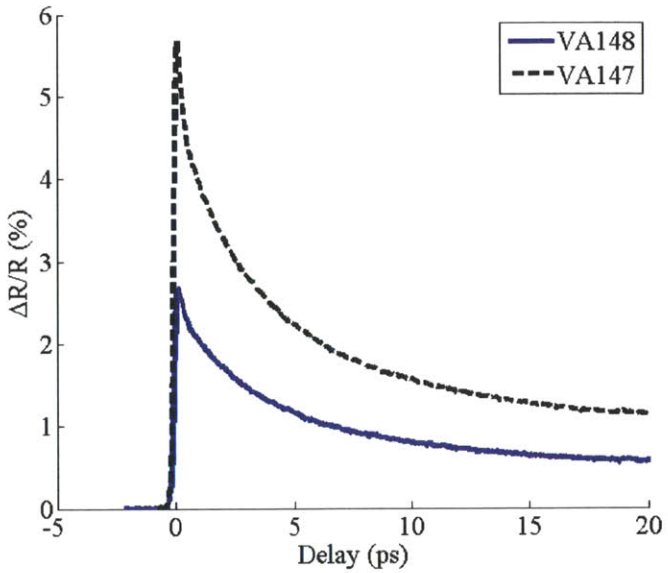

Figure 5-20 – Probe reflectivity as a function of the delay from the pump for both VA148 and VA147 samples at fluence of 25μJ/cm^2. Both samples have a long recovery time of 11ps.

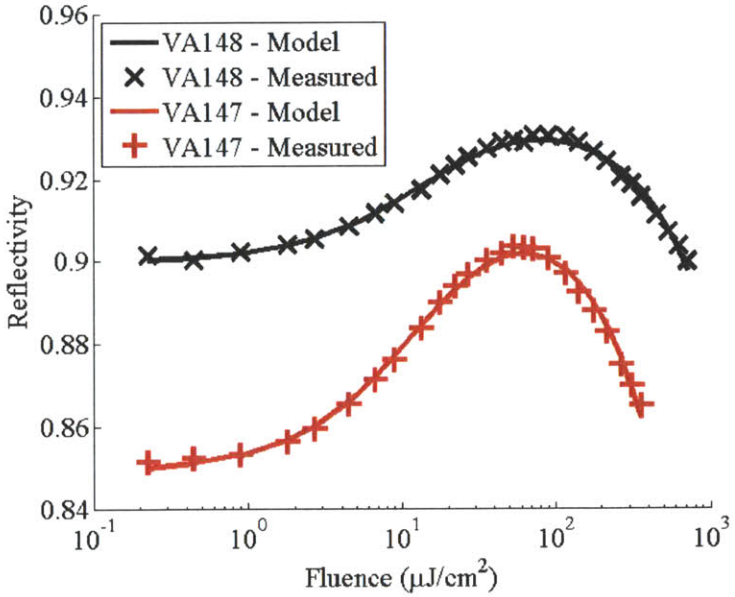

Figure 5-21 – Reflectivity of the VA147 and VA148 as a function of the fluence on the sample both measured and using a model to extract the saturable loss, non-saturable loss, and saturation fluence.

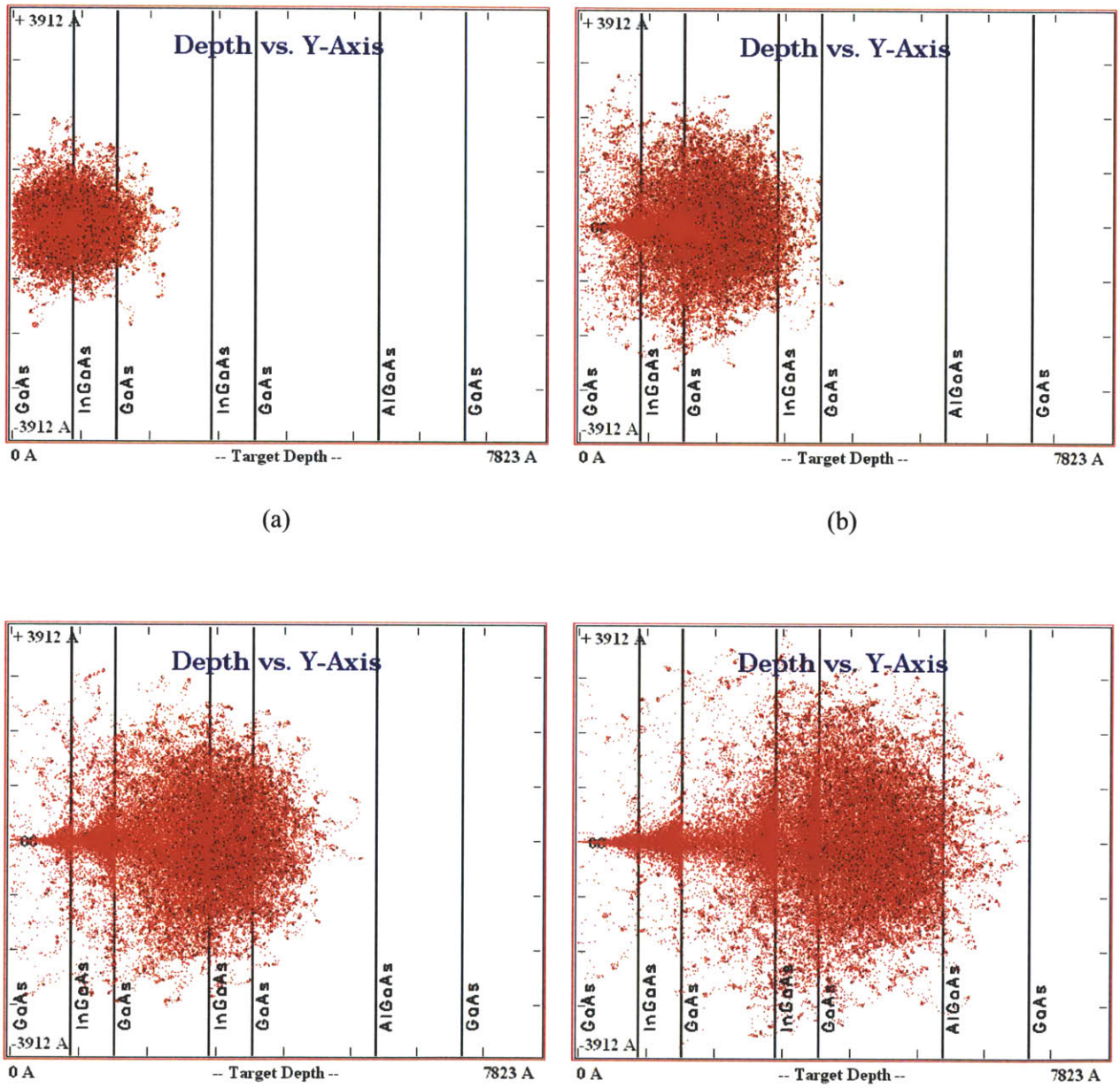

Figure 5-22 – TRIM simulation of the proton bombardment of VA148 sample. The protons enter the structure from the left. The red cloud shows the penetration depth of the protons. The proton energy levels of each figure are as follows: (a) 10KeV, (b) 25KeV, (c) 40KeV, and (d) 60KeV.

The effects of proton bombardment on the carrier dynamics of the VA148 sample were studied further. Since the two absorber layers in this structure are located at different depths inside the structure, several different combination of proton bombardment levels were utilized in this study. SRIM software (www.srim.org) was utilized to determine the depth of proton penetration as a function of the energy of the ion beams. The result of this simulation for proton energies of 10, 25, 40, and 60KeV are shown in Figure 5-22. The protons enter the structure from the left side of the page where the top layer of the VA148 is placed. As the protons travel through the structure, due to their collision with nuclei and interaction with the outer-shell electrons of the atoms in the structure, they slow down and deposit their energy along the way. The proton beam deposits most of its energy just before it comes to rest. In Figure 5-22, the red cloud indicates the stopping position of the protons. Based on this simulation, combination of 25KeV, 40KeV and 60KeV proton energies were selected for this study trying to reach different absorbing layers as tabulated in Table 5-8.

Table 5-8 – Combination of proton bombardment doses and energies on VA148 saturable absorber

Sample designation	Proton bombardment	
	Dose (/cm^2)	Energy(KeV)
PB0	-	-
PB40114	10^{14}	40KeV
PB60513	5×10^{13}	60KeV
PB60114	10^{14}	60KeV
PB25113+60513	10^{13};25KeV + 5×10^{13}; 60KeV	
PB25513+60114	5×10^{13};25KeV + 10^{14}; 60KeV	

Carrier lifetimes of the proton bombarded samples were measured using the cross-polarized pump probe experimental setup. The results for five of the six samples tested at $25\mu J/cm^2$ are shown in Figure 5-23. The pump probe trace for PB40114, the sixth sample, is not shown since it exhibits the same recovery times as PB60114 and PB25113+60513 samples. The long recovery times vary between 10.5ps for no proton bombardment down to 6ps for the PB25513+60114 sample which has received the highest dose. This latter sample exhibits 7% modulation depth which is more than 2 times that of the other VA148 proton bombarded samples. It also exhibits 7% higher unbleached loss compared to the other VA148 samples. This is demonstrated in the saturation dynamic studies as shown in Figure 5-24.

The large difference between the response of the PB25513+60114 sample and the rest of the VA148 samples may be due to the physical location of the wafer from which this sample was taken. As this sample was not tested prior to being sent for proton-bombardment, the larger unbleached loss, and modulation depth may have been present on the non-proton-bombarded sample. Since we are operating close to the edge of the bandwidth of the SBR, any variations in thicknesses of the mirror layers may result in a shift in the center wavelength of the Bragg stack. This shift in the center wavelength can result in a large unbleached loss. In addition, this large loss may be due to the refractive index changes induced by the implanted ions in different layers of the SBR, resulting in a shift of the absorber overlap with the peak of the E-field standing wave pattern. The large variation of the sample response observed in the PB25513+60114 characteristics emphasizes the importance of pump-probe characterization of saturable absorbers.

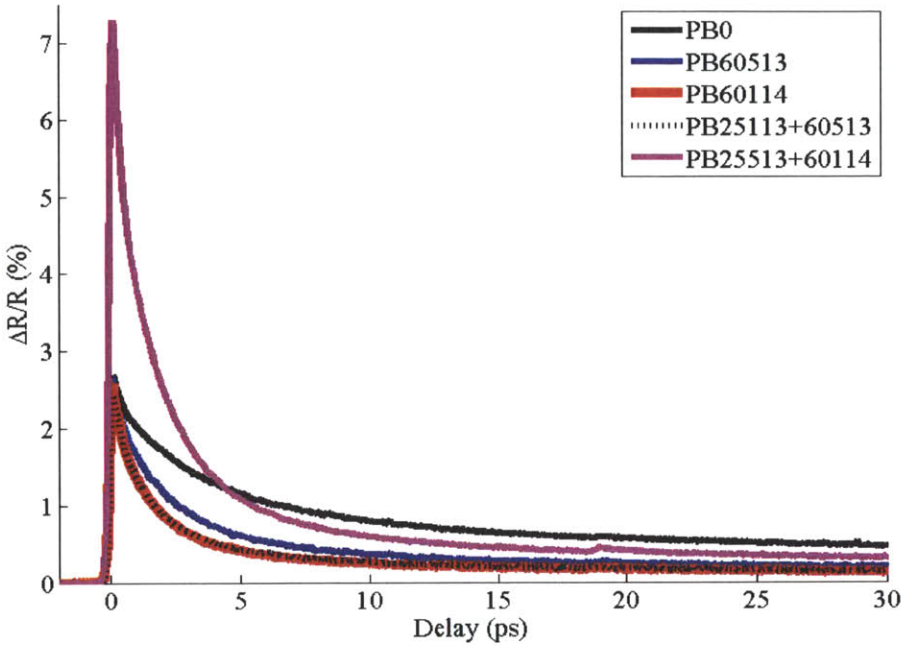

Figure 5-23 – Relative reflectivity change of the probe signal as a function of the delay from the pump signal with fluence of 25μJ/cm^2.

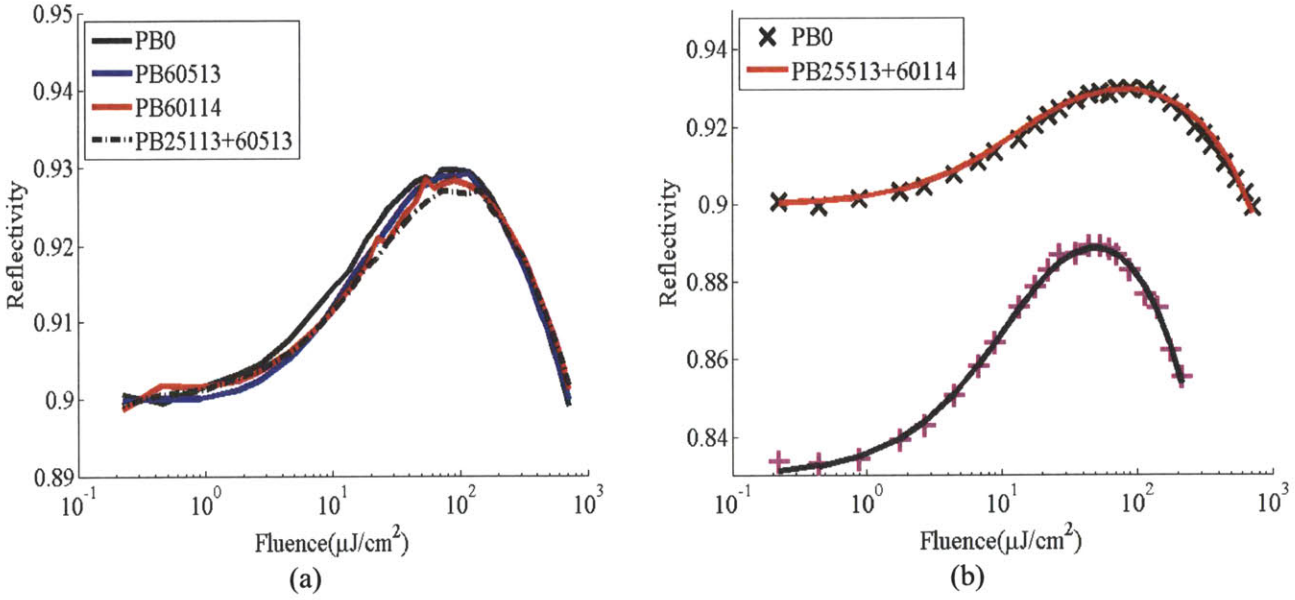

Figure 5-24 – Reflectivity of VA148 proton bombarded samples. (a) Proton bombardment has very little effect on the saturation dynamics of VA148. (b) Highest proton bombardment with 5×10^{13}/cm^2 at 25KeV plus 10^{14}/cm^2 at 60KeV results in addition 7% unbleached loss, and lower saturation fluence from 5.5 μJ/cm^2 down to 4.4 μJ/cm^2.

Table 5-9 – Saturation dynamics of the VA148 saturable absorber as a function of proton bombardment

Sample designation	Proton bombardment		Saturable loss	Saturation fluence	Non-saturable loss
	Dose (/cm^2)	Energy(KeV)	q_0 (%)	F_{sat} (μJ/cm^2)	R_{ns} (%)
PB0	-	-	3.9	5.4	6.2
PB40114	10^{14}	40KeV	5	6.1	5.2
PB60513	5×10^{13}	60KeV	4	5.8	6
PB60114	10^{14}	60KeV	3.9	6.4	6.2
PB25113+60513	10^{13};25KeV + 5×10^{13}; 60KeV		3.7	6.5	6.4
PB25513+60114	5×10^{13};25KeV + 10^{14}; 60KeV		9.0	4.4	8

5.6. Conclusion

Studies of ultrafast carrier dynamics of single and double absorber were described in this chapter. Effects of different proton bombardment levels on the carrier lifetime and the saturation dynamics of these devices were explored. We were able to reduce the carrier lifetime of the single-absorber devices from 12ps with no proton-bombardment down to 1.5ps with 10^{15}/cm^2 dose. However, the saturation fluence of this latter sample increased by more than a factor of 2 in the same range with the biggest increase observed between 5×10^{14} and 10^{15}/cm^2 doses. We also demonstrated that with the addition of resonant layers on an SBR, the saturation fluence of these devices can be lowered. We demonstrated a factor of four reduction in the saturation fluence of the single-absorber devices.

In addition, double-absorber SBRs were fabricated and their ultrafast carrier dynamics were studied. To determine the optimum design leading to higher modulation depth and lower

saturation fluence, two different designs with different cladding-layer thicknesses were fabricated and studied. The two different topologies demonstrated that further work is necessary to design the layer structures for optimum overlap of the absorber layer with the peak of the E-field pattern in the device. In addition, different proton bombardment levels and energy combinations were utilized to lower the carrier lifetime in these SBRs. Further work is necessary to optimize the doses and energy levels as the carrier lifetime of these devices were only shortened by a factor of 2 compared to that of the non proton-bombarded sample.

The future work on these latter samples may consist of fabrication of several different SBR structures with different cladding layer thicknesses. Further reduction in the saturation fluence can be explored by addition of resonant layers. Finally, with larger combination of proton bombardment levels and energies, the trade-off between the carrier lifetime reduction and the saturation dynamics can be better modeled.

5.7. References

[1] S. T. Cundiff and A. M. Weiner, "Optical arbitrary waveform generation," *Nat Photon,* vol. 4, pp. 760-766, 2010.

[2] E. Ippen, *et al.*, "Optical arbitrary waveform generation," in *Lasers and Electro-Optics (CLEO) and Quantum Electronics and Laser Science Conference (QELS), 2010 Conference on*, 2010, pp. 1-2.

[3] Z. Jiang, *et al.*, "Optical arbitrary waveform processing of more than 100 spectral comb lines," *Nat Photon,* vol. 1, pp. 463-467, 2007.

[4] Z. Jiang, *et al.*, "Line-by-line pulse shaping control for optical arbitrary waveform generation," *Opt. Express,* vol. 13, pp. 10431-10439, 2005.

[5] J. Ye, *et al.*, "Optical frequency combs: From frequency metrology to optical phase control," *IEEE Journal of Selected Topics in Quantum Electronics,* vol. 9, pp. 1041-1058, Jul-Aug 2003.

[6] S. T. Cundiff, *et al.*, "Optical frequency synthesis based on mode-locked lasers," *Review of Scientific Instruments,* vol. 72, pp. 3749-3771, Oct 2001.

[7] J. Kim and F. X. Kartner, "Attosecond-precision ultrafast photonics," *Laser & Photonics Reviews,* vol. 4, pp. 432-456, May 2010.

[8] T. Udem, *et al.*, "Optical frequency-comb generation and high-resolution laser spectroscopy," in *Few-Cycle Laser Pulse Generation and Its Applications*. vol. 95, ed Berlin: Springer-Verlag Berlin, 2004, pp. 295-316.

[9] D. C. Adler, *et al.*, "In vivo endomicroscopy using three-dimensional optical coherence tomography and Fourier Domain Mode Locked lasers - art. no. 684708," in *Coherence Domain Optical Methods and Optical Coherence Tomography in Biomedicine Xii*. vol. 6847, J. A. Izatt, *et al.*, Eds., ed, 2008, pp. 84708-84708.

[10] D. C. Adler, *et al.*, *Optical Coherence Tomography Phase Microscopy Using Buffered Fourier Domain Mode Locked (FDML) Lasers at up to 370,000 Lines per Second*, 2007.

[11] T. H. Tsai, *et al.*, "Frequency comb swept lasers," *Optics Express,* vol. 17, pp. 21257-21270, Nov 2009.

[12] A. Ben-Yakar and F. Bourgeois, "Ultrafast laser nanosurgery in microfluidics for genome-wide screenings," *Current Opinion in Biotechnology,* vol. 20, pp. 100-105, Feb 2009.

[13] M. Gu, *et al.*, "Ultrafast biophotonics," *Journal of Optics,* vol. 12, Aug 2010.

[14] J. Ye, *et al.*, "Applications of ferntosecond laser comb to nonlinear molecular spectroscopy," in *Astrophysics, Clocks and Fundamental Constants*. vol. 648, S. G. Karshenboim, Ed., ed, 2004, pp. 275-295.

[15] D. Bruneel, *et al.*, "Micromachining of metals with ultra-short Ti-Sapphire lasers: Prediction and optimization of the processing time," *Optics and Lasers in Engineering,* vol. 48, pp. 268-271, Mar 2010.

[16] M. Mielke, *et al.*, "Ultrafast Fiber Laser Platform for Advanced Materials Processing," *Journal of Laser Micro Nanoengineering,* vol. 5, pp. 53-58, Feb 2010.

[17] S. B. Fleischer, *et al.*, "Femtosecond optical-dynamics of C-60 and M3C-60," *Applied Physics Letters,* vol. 62, pp. 3241-3243, Jun 1993.

[18] J. T. Gopinath, *et al.*, "Recovery dynamics in proton-bombarded semiconductor saturable absorber mirrors," *Applied Physics Letters,* vol. 78, pp. 3409-3411, May 2001.

[19] K. L. Hall, *et al.*, "Femtosecond gain dynamics and saturation behavior in InGaAsP multiple quantum-well optical amplifiers," *Applied Physics Letters,* vol. 57, pp. 2888-2890, Dec 1990.

[20] K. L. Hall, *et al.*, "Subpicosecond gain and index nonlinearities in InGaAsP diode-lasers," *Optics Communications,* vol. 111, pp. 589-612, Oct 1994.

[21] K. L. Hall, *et al.*, "Heterodyne pump probe technique for time-domain studies of optical nonlinearities in wave-guides," *Optics Letters,* vol. 17, pp. 874-876, Jun 1992.

[22] M. Joschko, *et al.*, "Ultrafast hot-carrier dynamics in semiconductor saturable absorber mirrors," *Applied Physics Letters,* vol. 76, pp. 1383-1385, Mar 2000.

[23] P. Langlois, *et al.*, "High fluence ultrafast dynamics of semiconductor saturable absorber mirrors," *Applied Physics Letters,* vol. 75, pp. 3841-3843, Dec 1999.

[24] E. Lioudakis, *et al.*, "Femtosecond carrier dynamics in implanted and highly annealed polycrystalline silicon," *Semiconductor Science and Technology,* vol. 21, pp. 1041-1046, Aug 2006.

[25] E. Lioudakis, *et al.*, "Femtosecond dynamics in single wall carbon nanotube/poly(3-hexylthiophene) composites," *Nanoscale Research Letters,* vol. 3, pp. 278-283, Aug 2008.

[26] E. Lioudakis, *et al.*, "Probing carrier dynamics in implanted and annealed polycrystalline silicon thin films using white light," *Applied Physics Letters,* vol. 88, May 2006.

[27] A. Othonos, "Probing ultrafast carrier and phonon dynamics in semiconductors," *Journal of Applied Physics,* vol. 83, pp. 1789-1830, Feb 1998.

[28] M. Hofer, *et al.*, "Mode-locking with cross-phase and self-phase modulation," *Optics Letters,* vol. 16, pp. 502-504, Apr 1991.

[29] D. E. Spence, *et al.*, "60-fsec pulse generation from a self-mode-locked Ti-Sapphire laser," *Optics Letters,* vol. 16, pp. 42-44, Jan 1991.

[30] E. P. Ippen, *et al.*, "Additive pulse mode locking," *J. Opt. Soc. Am. B,* vol. 6, pp. 1736-1745, 1989.

[31] H. A. Haus, *et al.*, "Analytic theory of additive pulse and Kerr lens mode locking," *Quantum Electronics, IEEE Journal of,* vol. 28, pp. 2086-2096, 1992.

[32] K. Tamura, *et al.*, "Self-starting additive pulse mode-locked erbium fibre ring laser," *Electronics Letters,* vol. 28, pp. 2226-2228, 1992.

[33] H. A. Haus, *et al.*, "Additive-pulse modelocking in fiber lasers," *Quantum Electronics, IEEE Journal of,* vol. 30, pp. 200-208, 1994.

[34] H. A. Haus, *et al.*, "Stretched-pulse additive pulse mode-locking in fiber ring lasers: theory and experiment," *Quantum Electronics, IEEE Journal of,* vol. 31, pp. 591-598, 1995.

[35] H. A. Haus, "Mode-locking of lasers," *Selected Topics in Quantum Electronics, IEEE Journal of,* vol. 6, pp. 1173-1185, 2000.

[36] U. Keller, *et al.*, "Semiconductor saturable absorber mirrors (SESAM's) for femtosecond to nanosecond pulse generation in solid-state lasers," *IEEE Journal of Selected Topics in Quantum Electronics,* vol. 2, pp. 435-453, Sep 1996.

[37] D. H. Sutter, *et al.*, "Semiconductor saturable-absorber mirror-assisted Kerr-lens mode-locked Ti : sapphire laser producing pulses in the two-cycle regime," *Optics Letters,* vol. 24, pp. 631-633, May 1999.

[38] H. Byun, *et al.*, "Compact, stable 1 GHz femtosecond Er-doped fiber lasers," *Applied Optics,* vol. 49, pp. 5577-5582, Oct 2010.

[39] G. R. Jacobovitz-Veselka, *et al.*, "Broadband fast semiconductor saturable absorber," *Opt. Lett.*, vol. 17, pp. 1791-1793, 1992.

[40] R. Fluck, *et al.*, "Broadband saturable absorber for 10-fs pulse generation," *Opt. Lett.*, vol. 21, pp. 743-745, 1996.

[41] U. Keller, *et al.*, "Solid-state low-loss intracavity saturable absorber for Nd:YLF lasers: an antiresonant semiconductor Fabry?Perot saturable absorber," *Opt. Lett.*, vol. 17, pp. 505-507, 1992.

[42] C. Hönninger, *et al.*, "Femtosecond Yb:YAG laser using semiconductor saturable absorbers," *Opt. Lett.*, vol. 20, pp. 2402-2404, 1995.

[43] R. Takahashi, *et al.*, "Ultrafast 1.55 mu m all-optical switching using low-temperature-grown multiple quantum wells," *Applied Physics Letters*, vol. 68, pp. 153-155, 1996.

[44] Y. Silberberg, *et al.*, "Fast nonlinear optical response from proton-bombarded multiple quantum well structures," *Journal Name: Appl. Phys. Lett.; (United States); Journal Volume: 46:8*, pp. Medium: X; Size: Pages: 701-703, 1985.

[45] J. Mangeney, *et al.*, "Comparison of light- and heavy-ion-irradiated quantum-wells for use as ultrafast saturable absorbers," *Applied Physics Letters*, vol. 79, pp. 2722-2724, 2001.

[46] J. T. Gopinath, "Studies of Third-Order Nonlinearities in Materials and Devices for Ultrafast Lasers," Ph.D., Electrical Engineering and Computer Science, Massachusetts Institute of Technology, Cambridge, 2005.

[47] M. Haiml, *et al.*, "Optical characterization of semiconductor saturable absorbers," *Applied Physics B: Lasers and Optics*, vol. 79, pp. 331-339, 2004.

[48] E. R. Thoen, "Development of Ultrashort Pulse Fiber Lasers for Optical Communication Utilizing Semiconductor Devices," Ph.D., Electrical Engineering and Computer Science, Massachusetts Institute of Technology, Cambridge, 2000.

[49] J.-C. Diels, *et al.*, "Ultrashort Laser Pulse Phenomena," *Optical Engineering*, vol. 36, pp. 2362-2362, 1997.

Chapter 6

Conclusion

Ultrafast carrier dynamics and optical nonlinear properties of several active and passive devices were studied in this thesis. The devices studied included slab-coupled optical waveguide amplifiers (SCOWAs), silicon-based nanowaveguides, and III-V semiconductor saturable Bragg-reflectors (SBRs).

Slab-coupled optical waveguide amplifiers exhibit high optical output powers. Limitations imposed by nonlinear optical processes, namely TPA and FCA on the saturation power of a SCOWA were studied. The TPA coefficient and the effective cross-section of FCA were extracted from the study. We developed a model to predict the saturation energy of a SCOWA as a function of the input pulse energy. This model was utilized to determine the saturation energy of a SCOWA for amplification of ultrafast pulses. The saturation energy of a SCOWA transmitting 150fs pulses at an 80MHz repetition rate occurs at very low input energy levels. This makes producing any significant gain for long-haul transmission of such short pulses a challenge. This also creates a challenge to implement SCOWAs in ultrafast mode-locked lasers. The key to overcoming these challenges can be to reduce the effects of the TPA by constructing the slab layer, where the optical intensity is the highest, from higher bandgap materials compatible with the InP technology.

Ultrafast nonlinear optical properties of high-index contrast silicon waveguides of 106nm×497nm cross section were studied. A heterodyne pump-probe technique was utilized to characterize the magnitude of the TPA and FCA losses as well as the optical Kerr effect and the refractive index change as a function of the carrier density. The high sensitivity of the heterodyne technique has allowed for this characterization using very small carrier densities with great accuracy. We developed a model to predict nonlinear optical loss and phase change as a function of the input pulse energy. This model was utilized to predict the limitations imposed by the nonlinearity on the transmission of different pulse energies. As the carrier recovery of silicon can be in the order of several hundreds of picoseconds to nanoseconds, the devices were proton bombarded with different doses. Carrier lifetime of 33ps with proton bombardment level of 10^{15} /cm^2 with 14.8dB linear loss was achieved. Future work in this area may include further studies of proton bombardment to achieve shorter recovery times.

Ultrafast carrier dynamics of single and double absorber were studied in this chapter. Effects of different proton bombardment levels were explored on the carrier lifetime and the saturation properties of these devices. We were able to reduce the carrier lifetime of the single-absorber devices from 12ps with no proton-bombardment down to 1.5ps with 10^{15}/cm^2 dose. However, the saturation fluence of this latter sample increased by more than a factor of 2 in the same range with the biggest increase observed between 5×10^{14} and 10^{15}/cm^2 doses. We also demonstrated that with addition of resonant layers on a SESAM, the saturation fluence of these devices can be lowered. We demonstrated a factor of four reduction in the saturation fluence of the single-absorber devices.

In addition double-absorber SBRs were fabricated and their ultrafast carrier dynamics were studied. To determine the optimum design leading to higher modulation depth and lower

saturation fluence, two different designs with different cladding-layer thicknesses were fabricated and studied. The two different topologies demonstrated that further work is necessary to optimize the layer structures for optimum overlap of the absorber layer with the peak of the E-field pattern in the device. In addition, different proton bombardment levels and energy combinations were utilized to lower the carrier lifetime in these SBRs. Further work is necessary to optimize the doses and energy levels as the carrier lifetime of these devices were only shortened by a factor of 2 compared to that of the non proton-bombarded sample.

The future work on these latter samples may consist of fabrication of several different SBR structures with different cladding layer thicknesses. Further reduction in the saturation fluence can be explored by addition of resonant layers. Finally, with larger combination of proton bombardment levels and energies, the trade-off between the carrier lifetime reduction and the saturation properties can be better modeled.

Appendix A

Double Modulated Pump-Probe Dynamics

In this section, the mathematics of the double chopped pump probe experiment is described and formulas for determining the TPA coefficient using this technique are derived. To determine the nonlinear response and the recovery time of the device, a pump signal is passed through the device and the probe signal is used to determine the changes induced by the pump by passing the probe signal at different delays with respect to the former. Clearly, at the output, the pump and the probe signals must be separated and only the probe signal is detected so that the effects of the pump can be uniquely distinguished. One method to accomplish this is by cross-polarizing the pump and the probe so that a polarizer can be utilized to filter the unwanted pump at the output of the device. Another method is to make the pump and the probe at two different wavelengths, so that an optical filter can separate the probe pulse. Due to the large polarization dependence of the gain of SCOWAs to the input polarization of the incident light, and since the optimal operating wavelength is at 1540nm, neither one of these two methods can be utilized to measure the response of a SCOWA. Therefore, a degenerate double-chopped pump-probe signal is used, where the pump and the probe signals are each modulated at two distinct frequencies, and the output signal is detected at the sum of the frequencies of the two chopping frequencies.

The modulation of the pump and probe pulses can be accomplished using a mechanical chopper or an AOM. To simplify the mathematical analysis, we assume sinusoidal amplitude modulation with 100% modulation index, though this can be replaced with square wave modulation which is the case of mechanical chopping. Therefore, we can describe the modulated pump and probe signals as

$$I_p(t) = \frac{1}{2}\left(1 + m\cos(\omega_1 t)\right) I_{p,0}(t) \tag{A.1}$$

$$I_s(t) = \frac{1}{2}\left(1 + m\cos(\omega_1 t)\right) I_{s,0}(t), \tag{A.2}$$

where $I_{p,0}$ and $I_{s,0}$ are respectively the intensity of the unmodulated Gaussian pump and probe pulses at the input of the SCOWA, m is the modulation index which without the loss of generality are assumed to be 1, and ω_1 and ω_2 are the different chopping frequencies.

Differential equation describing the propagation of the probe pulse is given by

$$\frac{dI_s}{dz} = g\Gamma I_s - \beta I_p I_s, \tag{A.3}$$

where g is the gain of the amplifier, Γ is the confinement factor, and β is the two-photon absorption coefficient. Solving this differential equation to determine the intensity of the probe pulse at the output of the SCOWA, we have

$$I_s(L) = I_{s,0} e^{\int_0^L (g_0\Gamma - \beta I_p) dz}, \tag{A.4}$$

where

$$I_p = I_{p,0} e^{g_0 \Gamma z}. \tag{A.5}$$

Substituting Equation (A.5) in (A.4), we have

$$I_s(L) = I_{s,0} \exp(g_0 \Gamma L) \exp\left(-\frac{\beta}{\Gamma g} I_{p,0}\left(e^{g_0 \Gamma L} - 1\right)\right). \tag{A.6}$$

Since pump probe measurements are performed in the perturbative regime, the component of the second exponential term, ie $\frac{\beta}{\Gamma g} I_{p,0}\left(e^{g_0 \Gamma L}-1\right) \ll 1$, therefore, Equation (A.6) can be approximated as

$$\Delta I_s(L) = I_s(L) - I_{s,0} = -\beta I_s(L) I_p(L) \left(\frac{1-e^{-g_0 \Gamma L}}{g_0 \Gamma L}\right) L . \tag{A.7}$$

Substituting Equations (A.1) and (A.2) in the above equation, and only keeping the frequency term $\omega_1+\omega_2$, and accounting for the coherent artifact, and the effect of pump on the probe and vice versa at time delay τ=0, the peak absorption in the pump probe trace, normalized to the probe power is

$$\frac{\Delta I_s}{I_s(L)} = -2\beta \left(\frac{1-e^{-g\Gamma L}}{g\Gamma L}\right) L I_p(L) \cos\left(\omega_1+\omega_2\right) t . \tag{A.8}$$

The amplitude of the fractional loss due to TPA as detected on a lock-in amplifier at frequency $\omega_1+\omega_2$ is

$$2\beta \left(\frac{1-e^{-g\Gamma L}}{g\Gamma L}\right) L I_p(L) \propto \frac{E}{\tau}, \tag{A.9}$$

where τ is the pulsewidth, hence

$$\frac{\Delta I_s}{I_s(L)} \propto \frac{1}{\tau} . \tag{A.10}$$

Appendix B

TPA and FCA Effective Areas

in Highly Confined Waveguides

Differential equations describing the propagation of optical pulses in silicon nanowaveguides were given in Chapter 4. To extract the nonlinear optical parameters of these waveguides from the pump-probe measurements, the intensity of the optical signal inside the waveguide needs to be determined. Since the upper and lower cladding material is made up of HSQ and SiO_2, the nonlinear interaction is limited to the waveguide and none in the cladding layers. Since only a fraction of the optical mode interacts with the nonlinear region, it is necessary to define an effective area to determine the effective intensity of the optical signal to determine the TPA and FCA nonlinearities.

TPA is dependent on the intensity of the optical signal. Several different techniques have been utilized to calculate such effective area. The following table summarizes the different formulas for such calculation.

Table B-1 – Different techniques to calculate TPA effective area

Technique	Formula	TPA effective area (μm^2) 475×106nm	TPA effective area (μm^2) 1000×800nm	Reference
Integration over all space for weakly confined waveguides	$\frac{\left[\int_{\infty}\lvert E\rvert^2\,dxdy\right]^2}{\int_{\infty}\lvert E\rvert^4\,dxdy}$	0.275	0.474	[1]
Integration over core weakly confined with core nonlinearity	$\frac{\left[\int_{\infty}\lvert E\rvert^2\,dxdy\right]^2}{\int_{core}\lvert E\rvert^4\,dxdy}$	0.530	0.475	[2]
Foster	$\frac{\left[\int_{\infty}(E\times H).e_z\,dxdy\right]^2}{\int_{core}\left[(E\times H).e_z\right]^2\,dxdy}$	0.228	0.437	[3]
Strongly confined modes	$\frac{Z_0^2}{n_{inter}^2}\frac{\left[\int_{\infty}(E\times H).e_z\,dxdy\right]^2}{\int_{core}\lvert E\rvert^4\,dxdy}$	0.096	0.420	[4]
Strongly confined modes	$\frac{Z_0^2}{n_{inter}^2}\frac{3\left[\int_{\infty}(E\times H).e_z\,dxdy\right]^2}{\int_{core}\left[2\lvert E\rvert^4+\lvert E^2\rvert^2\right]dxdy}$	0.113	0.429	[5]
Mode solver		0.097	0.420	

As shown in this table, for large waveguides, all different techniques result in the same effective area, while in the smaller waveguides, the range of values increases dramatically. The technique used in this thesis is based on the exact solution using a numerical mode-solver developed by

Milos Popovic and Anatol Khilo. The mode-solver calculation results in the TPA effective area of the silicon waveguides to be $0.098\mu m^2$.

The free-carriers generated by the TPA process absorb light and result in further optical loss. Similar to the TPA process, an effective area needs to be defined for FCA calculations. The light in this case interacts with the free-carriers in the core, therefore, the distribution of these carriers needs to be calculated. Using the same mode-solver program used for the TPA effective area calculation, the FCA loss was modeled and the FCA effective area was determined to be $0.074\ \mu m^2$.

B.1. References

[1] G. Agrawal, *Nonlinear Fiber Optics*: Academic Press, 2001.

[2] A. Villeneuve, *et al.*, "Waveguide design for minimum nonlinear effective area and switching energy in AlGaAs at half the bandgap," *Electronics Letters,* vol. 31, pp. 549-551, 1995.

[3] M. Foster, *et al.*, "Optimal waveguide dimensions for nonlinear interactions," *Opt. Express,* vol. 12, pp. 2880-2887, 2004.

[4] C. Koos, *et al.*, "Nonlinear silicon-on-insulator waveguides for all-optical signal processing," *Opt. Express,* vol. 15, pp. 5976-5990, 2007.

[5] S. Afshar V and T. M. Monro, "A full vectorial model for pulse propagation in emerging waveguides with subwavelength structures part I: Kerr nonlinearity," *Opt. Express,* vol. 17, pp. 2298-2318, 2009.

Appendix C

Heterodyne Pump-Probe Analysis

Using pump probe techniques, the instantaneous and long-lived effects can be separated. In this section, the analysis on how to extract each parameter separately for the silicon waveguides analysis is given. This analysis can be extended to other devices.

The following derivations are based on conducting the pump-probe in the perturbative regime, i.e. where the response of the system is linear with the intensity of the pump. Therefore, we may assume an optical signal only experiences linear loss and it can described at the output of the waveguide by:

$$I(z) = I(0)e^{-\alpha_{lin}z}, \tag{C.1}$$

where I is the optical intensity and α_{lin} is the device linear loss.

C.1. Two-photon absorption

The instantaneous response due to TPA with a corresponding coefficient, β, can be modeled by

$$\frac{dI_S}{dz} = -(\beta I_P + \alpha_{lin})I_S, \tag{C.2}$$

where I_P and I_S are the pump and probe intensities, respectively. These intensities are calculated using the power of each signal divided by the TPA effective as calculated in Appendix B. Integrating both sides of this equation over the length of the device, we have

$$I_{S,TPA}(L) = I_S(0)e^{-\int_0^L(\beta I_P(z)+\alpha_{lin})dz} = I_S(L)e^{-\int_0^L \beta I_P(z)dz}, \tag{C.3}$$

where $I_{S,TPA}$ is the magnitude of the instantaneous response of the probe signal measured from the pump-probe experiment. Substituting for I_P as per Equation (C.1), we have

$$I_{S,TPA}(L) = I_S(L)\exp\left(-\int_0^L \beta I_P(0)\exp(-\alpha z)dz\right) = I_S(L)\exp\left(-\beta I_P(0)\frac{1-\exp(-\alpha L)}{\alpha}\right). \tag{C.4}$$

Since the measurements are made in the perturbative regime, we can use $e^{-x} \approx 1-x$, and rewrite Equation (C.4) as

$$\frac{\Delta I_{S,TPA}}{I_S(L)} = \frac{I_{S,TPA}(L)-I_S(L)}{I_S(L)} = -\beta I_P(0)\frac{1-\exp(-\alpha L)}{\alpha} = -\beta I_P(0)L_{TPA,eff}. \tag{C.5}$$

$\Delta I_{S,TPA}$ is the differential response of the instantaneous component of the pump-probe trace. The term $\Delta I_{S,TPA}/I_S$ is the normalized transmission or reflection measurement and it is directly proportional to the TPA coefficient. As the optical signal propagates through the device, it is attenuated due to the TPA loss, as a result, the effective length over which the signal experiences loss is the TPA effective length described by

$$L_{TPA,eff} = \frac{1-\exp(-\alpha L)}{\alpha}. \tag{C.6}$$

C.2. Free-carrier absorption

The FCA differential reflectivity can be derived similar to the TPA calculations. The differential equation describing the FCA loss can be described by

$$\frac{dI_S(z,t)}{dz} = -\left[\int_{-\infty}^{t} \sigma \frac{\beta I_P^2(z,t')}{\hbar\omega} dt' + \alpha_{lin}\right] I_S(z,t). \tag{C.7}$$

The intensity can be separated into two functions one as a function of time, and the other as a function of distance z. The above formula can be simplified to

$$\frac{dI_S(z,t)}{dz} = -\left(\sigma I_P^2(t) I_P^2(z) + \alpha_{lin}\right) I_S(z). \tag{C.8}$$

Solving this differential equation as a function of z and ignoring the time dependent part which can be added at the end, we have

$$I_{S,FCA}(L) = I_S(0)\exp\left(-\int_0^L \left(\sigma\beta I_P^2(t) I_P^2(z) + \alpha_{lin}\right) dz\right) = I_S(L)\exp\left(-\sigma\beta I_P^2(t)\int_0^L I_P^2(z) dz\right)$$

, (C.9)

where $I_{S,FCA}$ is the magnitude of the long-lived free-carrier induced loss on the probe signal. Since the pump-probe measurement is performed in the perturbative regime, Equation (C.1) can be used to describe the propagation of the pump intensity. This leads to

$$I_{S,FCA}(L) = I_S(L)\exp\left(-\sigma\beta I_P^2(t) I_P^2(0)\frac{1-\exp(-2\alpha L)}{2\alpha}\right). \tag{C.10}$$

Assuming perturbative pump-probe measurement, we have

$$\frac{\Delta I_{S,FCA}}{I_S(L)} = -\sigma\beta I_P^2(0) L_{FCA,eff}, \tag{C.11}$$

where $L_{FCA,eff}$ is the effective length of the FCA effect given by

$$L_{FCA,eff} = \frac{1-\exp(-2\alpha L)}{2\alpha}. \tag{C.12}$$

Appendix D

Carrier Density Calculation

In this appendix, the derivation of formulas to determine the TPA-induced free-carrier density in a passive waveguide of length L using the transfer function deviation of the waveguide from a linear response is given. As described in Chapter 4, and demonstrated in Figure D-1, the optical output power as a function of the input power deviates from a linear response with increasing optical input power. Since this deviation is a due to the TPA process, for every two photons absorbed, an electron and a hole are generated. The derivations in this section are in particular with reference to the silicon waveguides studied in this thesis. However, the formulas can be extended to other passive devices.

The optical loss as a function of the length of the device can be described by

$$\alpha(z) = \alpha_{lin} + \alpha_{NL} = \alpha_{lin} + \frac{\beta}{A_{TPA}} P(z), \tag{D.1}$$

where α_{lin} is the linear loss, β is the TPA coefficient, A_{TPA} is the TPA effective area, and $P(z)$ is the optical power inside the waveguide. For simplicity, we define

$$\varsigma = \frac{\beta}{A_{TPA}}. \tag{D.2}$$

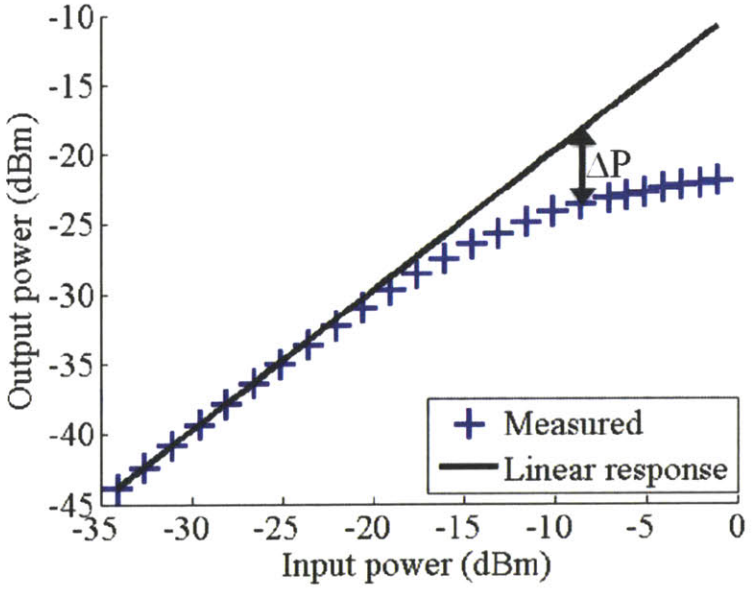

Figure D-1 - Optical output power of a silicon waveguide as a function of the input power.

Assuming that the optical signal experiences linear loss only so that

$$P(z) = P_0 e^{-\alpha_{lin} z}, \tag{D.3}$$

where P_0 is the input power coupled into the waveguide. The total optical loss due to the TPA process is given by

$$\alpha_{NL} = \varsigma \int_0^L P(z)\, dz = \varsigma P_0 \frac{1 - e^{-\alpha_{lin} L}}{\alpha_{lin}}, \tag{D.4}$$

In terms of the measured parameters, this total deviation from the linear loss can be calculated using

$$\alpha_{NL} = 1 - 10^{\left[\left(P_{out,meas}(dBm) - P_{out,lin}(dBm)\right)/10\right]}, \tag{D.5}$$

where $P_{out,lin}$ is the output power of the device without any nonlinear effects, and $P_{out,meas}$ is the actual measured output power. Furthermore, the total number of electrons and holes generated by the TPA process are given by

$$N_{Total,e} = N_{Total,h} = \frac{T}{2\hbar\omega}\int_0^L \varsigma P^2(z)dz\,, \tag{D.6}$$

where T is the repetition rate of the optical signal, $\hbar\omega$ is the energy of a photon at wavelength λ, and $N_{Total,e}$ and $N_{total,h}$ are the total number of generated carriers. Evaluating this integral by substituting Equations (D.3) and (D.4), we have

$$N_{Total,e} = N_{Total,h} = \frac{\alpha_{NL}}{2}\left(\frac{1-e^{-2\alpha_{lin}L}}{1-e^{-\alpha_{lin}L}}\right)\frac{E_{in}}{2\hbar\omega}\,, \tag{D.7}$$

where E_{in} is the energy of the optical pulses coupled into the waveguide.

Appendix E

Saturation Fluence Calculation Using Pump-Probe Measurements

The saturation properties of a saturable Bragg-reflector can be studied from the pump-probe experiments by measuring the probe transmission as a function of the pump fluence at zero time-delay. Detailed derivations of the formulas describing the saturation dynamics of an SBR is given in [1, 2]. These derivations are described for pump and probe beams with equal beam waists. In this section, this derivation is extended to the case where the pump and probe beams are of different sizes when focused on the sample.

The normalized Gaussian beam incident on an SBR can be described using [1]

$$I(r,t)=\frac{E}{\tau_p}f(t)\left(\frac{2}{r_0^2}e^{-r^2/r_0^2}\right), \tag{E.1}$$

where E is the energy of the pulse, τ_p is the pulsewidth, r_0 is the beamwaist of the Gaussian signal, and $I(r,t)$ is the intensity of the optical signal. The coefficients are set such that

$$E=\iint I(r,t)\,dtdA\,. \tag{E.2}$$

The time-averaged saturation properties of an SBR as a function of the incident fluence is given by[2]

$$q = q_0 \frac{1 - e^{-F/F_{sat}}}{F/F_{sat}}, \tag{E.3}$$

where F is the fluence of the optical signal, and F_{sat} is the saturation fluence of the SBR. The fluence is given by

$$F = \frac{2E}{\pi r_p^2} e^{-r^2/r_p^2}, \tag{E.4}$$

where r_p is the pump signal beam-waist. The saturation fluence is given by

$$F_{sat} = \frac{2E_{sat}}{\pi r_p^2}. \tag{E.5}$$

Substituting Equations (E.4) and (E.5) in (E.3) and integrating over the probe beam diameter, we have

$$q = \int_0^\infty q_0 \frac{1 - e^{-Ee^{-r^2/r_p^2}/E_{sat}}}{Ee^{-r^2/r_p^2}/E_{sat}} \frac{2re^{-r^2/r_s^2}}{r_s^2} dr, \tag{E.6}$$

where r_s is the probe signal beam-waist. Assuming the ratio of the pump and probe beams is

$$m = \frac{r_s^2}{r_p^2}, \tag{E.7}$$

Equation (E.6) can be re-written as

$$q = q_0 \frac{E_{sat}}{E} \int_0^\infty \frac{1 - e^{-E/E_{sat} e^{-r^2/r_p^2}}}{e^{-r^2/r_p^2}} e^{-r^2/mr_p^2} \frac{2r}{mr_p^2} dr. \tag{E.8}$$

To simplify this integral, the following change of variables is applied

$$x = \frac{r^2}{r_p^2} \Rightarrow dx = \frac{2r}{r_p^2} dr \tag{E.9}$$

$$q = \frac{q_0}{m}\frac{E_{sat}}{E}\int_0^{\infty}\frac{1-e^{-E/E_{sat}e^{-x}}}{e^{-x}}e^{-x/m}dx. \tag{E.10}$$

Further simplification is possible by applying the following change of variables

$$z = \frac{E}{E_{sat}}e^{-x} = \frac{F}{F_{sat}}e^{-x}. \tag{E.11}$$

Applying this change of variable to Equation (E.10), we have

$$q(F) = q_0\left(\frac{F_{sat}}{F}\right)^m \int_0^{F/F_{sat}}\frac{\left(1-e^{-z}\right)}{mz^2}z^m dz. \tag{E.12}$$

In the case where the pump and probe beam-waists are equal (m=1), this equation reduces to the formula in [1].

E.1. References

[1] E. R. Thoen, "Development of Ultrashort Pulse Fiber Lasers for Optical Communication Utilizing Semiconductor Devices," Ph.D., Electrical Engineering and Computer Science, Massachusetts Institute of Technology, Cambridge, 2000.

[2] M. Haiml, *et al.*, "Optical characterization of semiconductor saturable absorbers," *Applied Physics B: Lasers and Optics,* vol. 79, pp. 331-339, 2004.